A Quasi-Optical THz Mixer

Based on a Nb Diffusion-Cooled Hot-Electron Bolometer

Walter Ganzevles

3806
774771
312 3421
TR 3866

A Quasi-Optical THz Mixer Based on a Nb Diffusion-Cooled Hot-Electron Bolometer

Walter Ganzevles

BIBLIOTHEEK TECHNISCHE UNIVERSITEIT
Prometheusplein 1
2628 ZC
DELFT

A Quasi-Optical THz Mixer Based on a Nb Diffusion-Cooled Hot-Electron Bolometer

Proefschrift

ter verkrijging van de graad van doctor
aan de Technische Universiteit Delft,
op gezag van de Rector Magnificus prof. dr ir J.T. Fokkema,
voorzitter van het College voor Promoties,

in het openbaar te verdedigen op dinsdag 14 mei 2002 om 16:00 uur

door Walter Frank Maria GANZEVLES
natuurkundig ingenieur
geboren te Assen.

BIBLIOTHEEK TECHNISCHE UNIVERSITEIT
Prom[illegible]plein 1
DELFT

Dit proefschrift is goedgekeurd door de promotor:
Prof. dr ir T.M. Klapwijk

Samenstelling promotiecommissie:

Rector Magnificus,	voorzitter
Prof. dr ir T.M. Klapwijk,	Technische Universiteit Delft, promotor
Dr J.R. Gao,	Space Research Organization of the Netherlands, toegevoegd promotor
Prof. dr ir J.J.M. Braat,	Technische Universiteit Delft
Prof. dr W.T. Wenckebach,	Technische Universiteit Delft
Prof. dr E. Kollberg,	Chalmers Tekniska Högskola, Sweden
Prof. dr E.F. van Dishoeck,	Universiteit Leiden
Dr K. Jacobs,	Universität zu Köln, Germany

Dit onderzoek is gesteund door technologiestichting STW als onderdeel van NWO en het technologieprogramma van EZ.

Part of this work has been performed at DIMES, the Delft Institute of Microelectronics and Submicron Technology.

Part of this work has been performed at SRON, the Space Research Organization of the Netherlands.

This work has been financially supported in part by the European Space Agency (ESA) under contract no. 11738/95/NL/PB.

Ganzevles, Walter Frank Maria
A Quasi-Optical THz Mixer Based on a Nb Diffusion-Cooled Hot-Electron Bolometer / Walter Frank Maria Ganzevles.

Ph.D. thesis, Delft University of Technology. – With ref. – With summary in Dutch.
ISBN 90–9015747–6
Keywords: Heterodyne receivers / THz detection / Superconducting devices / Planar antennas

Preface

This thesis describes the development of a diffusion-cooled quasi-optical Nb hot electron bolometer mixer (HEBM). This development is driven by the need for a sensitive heterodyne detector with a large IF bandwidth that will find its use in astronomical and atmospherical observations.
The mixer is a short superconducting strip that is contacted by normal metal cooling pads. The resistance of this strip varies with the beatings in incoming rf power. This rf power is a superposition of the signal to be observed and the well-known local oscillator. Variations in device resistance reflect variations in the signal to be detected.
The mixer's operation is described in terms of the recently developed hot spot model. This model describes the current-voltage (I(V))-curve of such a mixer. From this, the device's voltage responsivity and gain can be calculated, and to some extent, the intermediate frequency bandwidth can be predicted.
One of the crucial issues in this type of detectors is to efficiently couple the signal from free space into the superconducting bridge. This thesis describes the properties of several quasi-optical coupling schemes used in the literature. A novel coupling scheme employing microstrip transmission lines is proposed and designed. Models to design these microstrip transmission lines and the co-planar waveguide (CPW) transmission lines that have been described in literature are described and an optimization of the design is done.
Several fabrication processes using (nano)lithographical tools, reactive ion etching and sputter deposition of metals are described. Devices produced by these processes are characterized at both dc and rf-frequency. The results are compared and an evaluation of the processes is made.
A comparison between the designed and measured direct response of both CPW-coupled and microstrip line coupled devices is made.
Finally, the heterodyne properties of several types of devices are explored and sensitivity, gain and IF bandwidth are measured.

Contents

1 Introduction **3**

1.1 Applications of THz detection 3

1.2 Astronomical THz observatories 4

1.3 Heterodyne detection 5

1.3.1 Principle of heterodyne detection 5

1.3.2 Detector requirements 6

1.3.3 Existing technologies 7

1.4 Rationale for the use of quasi-optical hot-electron bolometer mixers 10

1.5 Thesis outline 11

2 Principle of device operation **13**

2.1 Introduction 13

2.2 Bolometers 14

2.2.1 Radiation detection 14

2.2.2 Responsivity and speed 14

2.2.3 Superconducting hot electron bolometer mixers 16

2.3 The lumped element model 19

2.4 The hot-spot model 20

2.4.1 Voltage responsivity and conversion gain 22

2.4.2 Intermediate bandwidth 23

2.4.3 Noise temperature 25

2.5 Discussion 27

3 Quasi-optical coupling schemes **29**

3.1 Waveguide coupling 29

3.2 Quasi-optical mixers 31

3.3 Quasi-optical lens configurations 32

3.4 Planar antennas 34
3.5 On-chip transmission lines: CPW and microstrip lines 36
3.5.1 Microstrip line characteristics 37
3.6 Discussion 40

4 Lay-out and design ... 43
4.1 Introduction 43
4.2 Method to simulate the direct response of HEBMs 44
4.2.1 Outline of the rf structure using twin-slot antenna coupled HEBMs 44
4.3 Microstrip line coupled HEBMs 45
4.4 CPW-coupled HEBMs 47
4.4.1 Results of the equivalent circuit-approach for CPW devices 51
4.4.2 Method of Moments-calculation of the intrinsic CPW coupling 52
4.5 Microstrip line-coupled HEBMs 54
4.5.1 The influence of surface impedance at high frequency 54
4.5.2 Results of the equivalent circuit approach for microstrip line devices 58
4.6 Discussion 60
4.7 Conclusions 62

5 Device fabrication 65
5.1 Introduction 65
5.2 Process outline of co-planar waveguide-based HEBMs 67
5.3 Process outline of microstrip-line based HEBMs 74
5.4 Discussion 77
5.5 Conclusion 82

6 Direct response of co-planar waveguide coupled ... 85
6.1 Introduction 85
6.2 Simulation of the direct response 87
6.3 Measurements of the direct response 90
6.4 Discussion 91
6.5 Conclusion 92

7 Direct response of microstrip line coupled ... 95
7.1 Introduction . . . 95
7.1.1 Sample Fabrication . . . 96
7.2 Discussion . . . 101
7.3 Conclusions . . . 102

8 The detailed characterization of ... 105
8.1 Introduction . . . 105
8.2 Measured mixer characteristics . . . 106
8.2.1 Device IS 1_4 F3 . . . 106
8.2.2 FTS of the device . . . 109
8.2.3 Pumped current-voltage characteristics . . . 110
8.2.4 Receiver– and mixer sensitivity . . . 112
8.2.5 Gain . . . 116
8.2.6 Output noise . . . 118
8.2.7 IF bandwidth . . . 119
8.3 Analysis and comparison to hot-spot model . . . 121
8.4 Discussion . . . 123
8.5 Conclusion . . . 124

9 Heterodyne measurements on a twin-slot HEBM at 0.7 THz 129
9.1 Device geometry . . . 129
9.2 Direct response of device IS 1_2 G4 . . . 131
9.3 Heterodyne sensitivity . . . 132
9.4 Gain . . . 136
9.5 IF bandwidth . . . 137
9.6 Discussion . . . 139
9.7 Conclusion . . . 142

10 Conclusions and outlook 145

11 Samenvatting 151

12 Summary 155

A Experimental methods and equipment used ... 157
A.1 Experimental set up 157
A.1.1 Cryogenic hardware 157
A.1.2 Sensitivity measurements 160
A.1.3 IF bandwidth measurements 162
A.2 Experimental methods 163
A.2.1 Noise temperature: the Y-factor measurements 163
A.2.2 Gain 165
A.2.3 Mixer output noise 166

B Production parameters for Nb HEBMs 169
B.1 Production parameters for Nb HEBMs 169

List of publications 176

Curriculum Vitæ 179

Dankwoord 180

Chapter 1

Introduction

1.1 Applications of THz detection

Observations of the universe have been performed throughout almost the entire electromagnetic spectrum, from radiowaves to gamma-rays. Only few frequency regimes have not been used to explore the nature and origin of galaxies, stars and planets. One such regime is the submm range (wavelength about $50 - 1000\,\mu$m), also called THz range (frequency 0.3-6 THz). This frequency range is particularly interesting because many small molecules like CO, H_2CO and CH_3OH are known to have rotational transitions in this regime[1]. Also the C^+-ion has a transition in this range, as do several hydrides. Observations in this part of the spectrum give information about the abundance and excitation of these molecules, shedding light on the chemical and physical processes associated with the formation of stars and galaxies. The optical regime (wavelength around 500 nm) is not suitable for studies of star– and galaxy formation, since this inherently occurs in dusty regions, obscuring the actual formation process. Energy released in this process is absorbed and re-emitted by the dust, especially so in the submm-regime. The chemical composition of the dust and its physical parameters like temperature and pressure can be deduced from the spectral information contained in the re-emitted radiation, thus giving much information about the circumstances under which the formation of stars and galaxies takes place.

Other applications of THz detection are in atmospheric research. Gases similar to those mentioned above are known to influence the earth's ozone

layer. Especially, transitions of HCl at 0.64 THz, the C^+ at 1.9 THz and of the hydroxyl group around 2.5 THz are of interest in this field. The overall picture of chemical reactions involved in the destruction of the ozone layer will be more complete once the distribution and abundance of these gases are known. Eventually, with this knowledge one hopes to find a way of stopping the destructing of the ozone layer. The frequencies at which these spectral lines are found have been one of the drivers for choosing the frequencies used in this thesis.

1.2 Astronomical THz observatories

Observation facilities for frequencies up to about 1 THz have been realized on earth, e.g. the James Clark Maxwell Telescope (JCMT[7]), CalTech Submillimeter Observatory (CSO[8]), the Heinrich Hertz Telescope[9], the KOSMA-telescope at the Gornergrat[10] and, to some extent, IRAM's 30 m telescope at Pico Veleta[11]. A masterpiece of astronomical instrumentation will be built in Chile: ALMA, the Atacama Large Millimeter Array[12] will consist of 64 dishes that will be linked such that interferometric observations can be performed, strongly improving the resolution of the system compared to a single-dish system. These telescopes are built on high mountain tops (CSO and JCMT on Mauna Kea, Hawaii, Heinrich Hertz at Mount Graham, Arizona, KOSMA's on a mountain near Zermatt, Switzerland and IRAM's in Spain) because water vapor absorbs a large part of the radiation from space. Telescopes built at high and dry places suffer least from this absorption.

To decrease the absorption by water vapor even more, observatories have to be placed in air– or even spacecraft. Observations above ~ 1 THz can only be done outside (or very high in) the earth's atmosphere. Astronomical observation platforms in airplanes such as the Kuiper Airborne Observatory (KAO[2]) and the Stratospheric Observatory For Infrared Astronomy (SOFIA[3])) and spacecraft (ISO[4], Herschel[5] (formerly known as the Far InfraRed Space Telescope, FIRST) and the International Space Station[6]) are or have been developed. These are, contrary to earthly observatories, able to study the abundance of water in the universe.

1.3 Heterodyne detection

Heterodyne receivers are rather common: a radio– or TV set is a good example, as is a cell phone. Their working principle will be sketched in this Section. To be of use as a practical detector, a mixer has to fullfil many requirements. These mainly concern signal frequency, sensitivity and intermediate frequency (IF). These will be discussed below.

1.3.1 Principle of heterodyne detection

In a heterodyne receiver, the signal to be detected, at a radial frequency ω_{sig}, is combined with a strong, well characterized signal from a local oscillator (LO) at a frequency ω_{LO}. The difference between both frequencies is called the intermediate frequency $\omega_{\mathrm{IF}} = |\omega_{\mathrm{sig}} - \omega_{\mathrm{LO}}|$ and is in the order of a few GHz (typically, 1–2% of ω_{rf}). Combining the LO and signal power in a mixing element results in an amplitude modulation (beatings) of the total radiation falling on the mixing element. A heterodyne receiver measures this amplitude modulation, which contains the spectral information that was present in the original signal.

To mathematically describe the mixing process, we assume that these mixers are square-law devices (note, however, that heterodyne detection is not restricted to this type of device), i.e. their heating power as a function of voltage is given by[13]

$$\mathrm{P(V)} = \frac{\mathrm{V}^2}{\mathrm{R_{HEB}}}. \tag{1.1}$$

P(V) is the total power coming into the device as a function of rf voltage V and $\mathrm{R_{HEB}}$ is the resistance of the device. For simplicity, we neglect the dc bias voltage in this discussion. The voltages due to the LO and incoming signal, respectively, are given by:

$$\mathrm{V_{LO}(t)} = \mathrm{V_{LO}} \cos(\omega_{\mathrm{LO}} \mathrm{t}) \tag{1.2}$$

and

$$\mathrm{V_{sig}(t)} = \mathrm{V_{sig}} \cos(\omega_{\mathrm{sig}} \mathrm{t}), \tag{1.3}$$

where $\omega_{\mathrm{sig,LO}}$ is the angular frequency of the signal and LO, respectively, and t is the time. $\mathrm{V_{sig,LO}}$ is the voltage amplitude of signal and LO, respectively.

Using some elementary algebra, Eq. (1.1) is rewritten as follows:

$$\begin{aligned} P(V,t) &\propto \left(V_{LO}\cos(\omega_{LO}t) + V_{sig}\cos(\omega_{sig}t)\right)^2 \\ &= \Big[\tilde{V}_{LO}^2 + \tilde{V}_{sig}^2 + \frac{1}{2}V_{LO}V_{sig}\cos\left((\omega_{LO}+\omega_{sig})t\right) \\ &\quad \underbrace{+\frac{1}{2}V_{LO}V_{sig}\cos\left((\omega_{LO}-\omega_{sig})t\right)}_{\text{IF signal}}\Big] \end{aligned} \tag{1.4}$$

The first two terms are a time-average, the third frequency-dependent term in Eq. (1.4) is of order $2\omega_{LO}$ and, since the device is only fast enough to respond to the IF frequency, these can be neglected in this discussion. The last argument is not general, but it holds for the HEBM.

The component with $\omega_{IF} = |\omega_{LO} - \omega_{sig}|$ is of most interest, since it is the downconverted signal. As can be seen in Fig. 1.1[a], the features present in the signal at high frequency are directly down-converted to IF. In the process, some loss may occur (decreasing the signal amplitude) and some noise may be added (lifting the noise floor). Both effects are illustrated in the figure.

Since $\cos(\omega_{LO} - \omega_{sig}) = \cos(\omega_{sig} - \omega_{LO})$, signal from both above (upper sideband) and below (lower sideband) the LO frequency is downconverted into ω_{IF}. The IF signal is further amplified and studied. It provides the same information as is available at ω_{sig}, but since this information is now available at a few GHz, it can readily be amplified and unraveled by a spectrometer.

At first sight, heterodyne detection is a complicated technique. Its advantages, however, make it a suitable technique for astronomical study. First, since no filters are necessary to obtain spectral information from the signal, the loss due to these is absent. Second, the spectral information is obtained at low (IF) frequency, making signal processing relatively simple. Then, the resolution can be high, enabling the detailed study of spectral lines.

1.3.2 Detector requirements

To study variety, abundance and physical parameters of gas clouds in the universe, one needs spectral information. At high frequencies, most detectors are not able to provide spectral information directly. Therefore, spectral information has to be obtained using a filter in front of the detector, e.g. a grating or a Fabry-Perot etalon. In a heterodyne mixer, spectral information

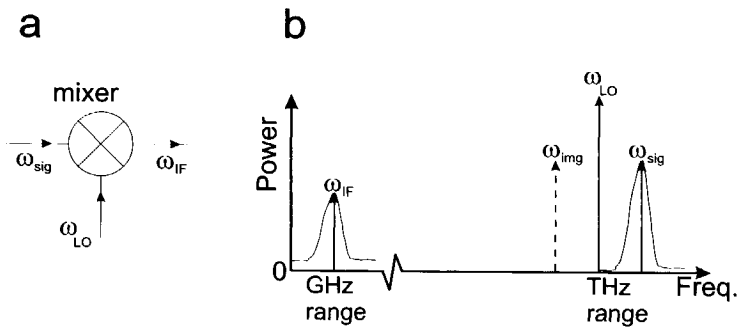

FIGURE 1.1. [a] Schematic representation of the mixing process. [b] Downconversion of the signal at $\omega_{\rm sig}$. Note that the image frequency $\omega_{\rm img}$ is also converted into the IF band, adding noise to the measured IF signal.

is extracted from the downconverted signal at the intermediate frequency. Fig. 1.2 shows an example of the spectrum of the CO J = 6 – 5-transition in Orion using a heterodyne receiver.

The requirements on the mixer are mainly set by the astronomical observations that will be done with it. Studies on distant gas clouds containing small traces of molecules or molecules with low transition probabilities require very sensitive detectors. For example, research on a particular transition of a single molecular species requires only narrow rf bandwidth, but a very high spectral resolution, while an unbiased survey of all chemical species present in a certain object requires a large rf bandwidth.

An important requirement is that of a high IF bandwidth. The IF bandwidth determines how many LO steps are needed to map the entire rf band. The higher the IF, the less LO steps are necessary, reducing the total measurement time. A large IF bandwidth also allows wide spectral lines, e.g. the wide, Doppler-shifted lines from external galaxies, to be measured in one scan.

1.3.3 Existing technologies

The non-linearity in the I(V)-curve can also be used in a mixer. Several devices having non-linear I(V)s have been used as a mixer. Some of

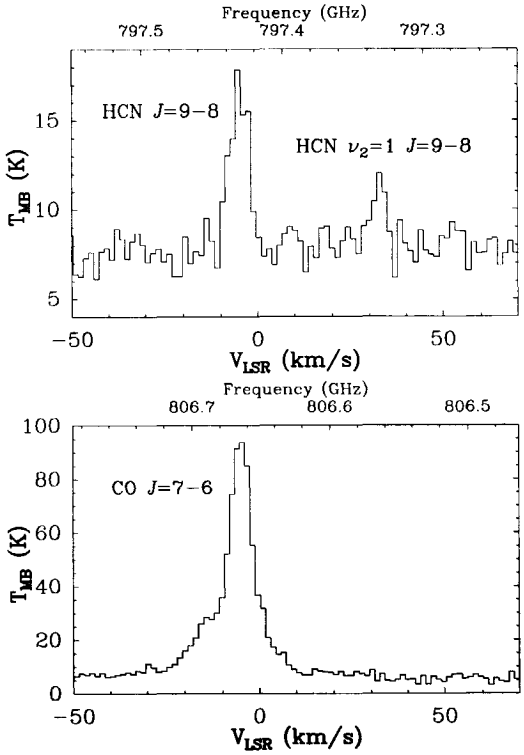

FIGURE 1.2. Spectrum of the the $\nu_2 = 0$ J = 9 − 8 and the vibrationally excited $\nu_2 = 1$ J = 9 − 8 line of HCN in the massive protostar GL 2591 at 797.434 and 797.330 GHz, respectively, taken with the Bonn/SRON 800 GHz receiver at JCMT. The CO J = 7 − 6 at 806.652 GHz is shown for comparison. Image taken from Boonman *et al.*[14].

the most important are Schottky-diode mixers, superconductor-insulator-superconductor (SIS) mixers and hot-electron bolometer mixers.

Schottky-diodes

Schottky-diodes work over a wide frequency range (up to several THz) and do not require cooling to cryogenic temperatures. Their sensitivity, however, is rather poor and large amounts of LO power (several mW) are required to

operate them. The latter disadvantage is an important issue in the application of this type of detector. Generation of rf radiation above about 1 THz is difficult. The only strong sources available are far infra-red (FIR) lasers, which are bulky, heavy and not tunable in frequency. These properties make them unsuitable for use in air– or space-borne missions.

Superconductor-insulator-superconductor mixers

Extremely sensitive (quantum limited) heterodyne mixers have been built for the 0.1–0.7 THz range[15]. These mixers rely on $Nb/Al_xO_y/Nb$ junctions and Nb superconducting transmission lines. Above the gap frequency of a superconductor, given by $f_{gap} = \Delta/h$, in which Δ is the superconducting gap energy and h Planck's constant, the loss increases dramatically. Therefore, normal-metal transmission lines have to be used to avoid the strongly increasing loss of Nb above f_{gap}[16]. Recently, superconductors with a higher f_{gap}, like NbN and NbTiN have been used in transmission lines[17]. This has pushed the (experimentally observed) upper frequency limit in SIS-mixers to 1.2 THz[18]. Advantages of SIS-mixers are their wide IF bandwidth and rather low LO power requirements and the fact that the technology is well developed. Next to the intrinsic upper frequency limit, another disadvantage of SIS-mixers is their intrinsic capacitance $C_{junction}$. In order to couple radiation effectively to the device, $C_{junction}$ has to be tuned out by the transmission line. This makes the design of sensitive, high-frequency, wide-band SIS mixers difficult.

Hot-electron bolometer mixers

Superconducting hot electron bolometer mixers (HEBMs) require very low (few tens of nW, whereas SIS-detectors, for example, require several hundreds of nW) LO power, they have a high sensitivity and (virtually) no upper frequency limit. These properties make it the detector of choice in the super-THz regime where SIS junctions show sharply decreasing performance. From a practical point of view, the limited IF bandwidth in HEBMs has initially been a matter of concern. Application of a mixer, e.g. in astronomical receivers, requires an IF bandwidth of at least a few GHz. Semi- and superconductor HEBMs have been fabricated and used before[19–21], but have shown IF bandwidths of up to only about 150 MHz. To overcome these

obstacles, much effort has been put in developing HEBMs with a high IF bandwidth in recent years.

1.4 Rationale for the use of quasi-optical hot-electron bolometer mixers

The aim of the research reported in this thesis is to *design, build* and *understand* a heterodyne mixer based on HEBMs around 2.5 THz for use in future astronomical and atmospherical observatories.

When starting this thesis work, no heterodyne receiver was available above 1 THz that is sensitive, has a high IF bandwidth and requires low LO power. Such a receiver is urgently needed by the astronomical community for studies to the chemistry of the universe, star formation and the processes that took place shortly after the Big Bang.

From theoretical predictions[22,23], these merits are expected to be combined in the superconducting hot electron bolometer mixer and indeed, in recent years, experiments have indicated that these desirable properties are present in superconducting HEBMs.

Superconducting HEBMs based on NbN have been introduced in the early 1990s[19]. One of the major difficulties with respect to these devices is obtaining a sufficiently large IF bandwidth. For large IF bandwidth, an extremely thin film is required, which is difficult to produce reliably. A breakthrough came in 1993 with the proposal of the diffusion-cooled Nb HEBM[22], as this type of mixer offers tuning of the IF by changing the length of the mixing element. We decided to study the latter type of hot-electron bolometer mixers since, over the years, our lab has obtained much experience in both producing thin Nb films and micro– and nano-patterning by means of sophisticated lithography techniques and because of the promising IF-properties.

A promising theory describing the operation of superconducting HEBMs has been developed recently[24,25]. This model is able to qualitatively describe the behavior of the mixers. However, the model does not describe mixer noise and gain accurately yet. To improve the understanding of these parameters, a better comparison between the model and experiments is needed.

The interesting features of Nb HEBMs made us decide to work on the development of receivers based on these devices.

1.5 Thesis outline

In this thesis, we start out with describing the principle of operation of a superconducting hot-electron bolometer mixer (Ch. 2). Since initially, not much expertise was present in our group on the coupling of signals at several THz, effort has been put into the development and characterization of a quasi-optical (QO) setup and the rf design of the devices themselves. This work has been described in Chs. 3 and 4. In Ch. 5 the fabrication processes required for the device production are described. Chs. 6 and 7 describe the characterization of the direct response of two types of twin-slot coupled HEBMs and in Chs. 8 and 9 we report on heterodyne measurements. Finally, in Ch. 10 we present the conclusions that are drawn from this work and we put this work and its consequences in perspective.

References

[1] For example, see N.G. Douglas, *Millimetre and submillimetre wavelength lasers,* Springer Series in Optical Sciences **61**, ISBN 3-540-50827-9, Springer-Verlag, New York (1989).

[2] See `http://quest.arc.nasa.gov/lfs/about-kao^.html`

[3] See `http://sofia.arc.nasa.gov/`

[4] See `http://isowww.estec.esa.nl/`

[5] See `http://www.sron.rug.nl/hifiscience/`

[6] See `http://spaceflight.nasa.gov/station/`

[7] See `http://www.jach.hawaii.edu/JACpublic/index.html`

[8] See `http://www.caltech.edu/subpages/pmares.html`

[9] See `http://maisel.as.arizona.edu:8080/smt.html`

[10] See `http://www.astro.uni-bonn.de/~webrai/Arbeitsgruppen/Kosma/kosma_eng.html`

[11] See `http://www.iram.es/`

[12] See `http://www.eso.org/outreach/press-rel/pr-1999/pr-09-99.html`

[13] For example, see J. Lesurf, *Millimeter-wave optics, devices and systems,* IOP Publishing Ltd. (1990).

[14] A.M.S. Boonman, R. Stark, F.F.S. van der Tak, E.F. van Dishoeck,

P.B. van der Wal, F. Schäfer, G. de Lange and W.M. Laauwen, Astrophys. J. **553**, L63-L67 (2001).

[15] C.K. Walker, J.W. Kooi, M. Chant, H.G. LeDuc, P.L. Schaffer, J.E. Carlstrom and T.G. Phillips, Int. J. IR and MM waves **13**, 785 (1992).

[16] H. v.d. Stadt, A. Baryshev, P. Dieleman, T.M. Klapwijk, S. Kovtonyuk, G. de Lange, I. Lapitskaya, J. Mees, R. Panhuyzen, G. Prokopenko and H. Schaeffer, Proc. 6th Int. Symp. Space THz Techn., Pasadena, CA, March 21-23, pp. 66-77 (1995).

[17] J.W. Kooi, J.A. Stern, G. Chattopadhyay, H.G. LeDuc, B. Bumble and J. Zmuidzinas, Proc. 9th Int. Symp. Space THz Techn., Pasadena, CA, March 17-19, pp. 283-295 (1998).

[18] A. Karpov, D. Miller, F. Rice, J. Zmuidzinas, J.A. Stern, B. Bumble, H.G. LeDuc, Proceedings of the 8th International Superconducting Electronics Conf., Osaka, Japan, June 19-22, pp. 521-522 (2001).

[19] E.M. Gershenzon, G. Gol'tsman, I.G. Gogidze, Y.P. Gusev, A.I. Elant'ev, B.S. Karasik and A.D. Semenov, Sov. Phys. Superc. **3**, 1582 (1990).

[20] F. Arams, C. Allen, B. Peyton and E. Sard, Proc. IEEE **54**, 612 (1966).

[21] T.G. Phillips and K.B. Jefferts, Rev. Sci. Instrum. **44**, 1009 (1973).

[22] D.E. Prober, Appl. Phys. Lett. **62**, 2119 (1993).

[23] B.S. Karasik and A.I. Elantiev, Appl. Phys. Lett. **68**, 853 (1996).

[24] D. Wilms Floet, E. Miedema, T.M. Klapwijk and J.R. Gao, Appl. Phys. Lett. **74**, 433 (1999).

[25] H.F. Merkel, E.L. Kollberg and K.S. Yngvesson, Proc. 9th Int. Symp. Space THz Techn., Pasadena, CA, March 17-19, pp. 81-97 (1999).

Chapter 2

Principle of device operation

This Chapter describes the principle of operation of superconducting HEBMs. Since it is beyond the scope of this thesis to fully cover all details, only the elements used in this work are mentioned.

2.1 Introduction

A bolometer is a device that detects radiation by collecting radiation power in an absorber. The corresponding temperature increase is sensed by a thermometer, e.g. a metal strip of which the electrical resistance changes with temperature. Bolometers can be used in *direct* or in *heterodyne* mode.

In direct mode, the total amount of power absorbed is quantified by measuring the temperature increase. In this case, only the overall power is measured since there is no spectral information available. Frequency-selectivity can only be obtained using a grating or a filter in front of the bolometer. In heterodyne mode, the device is used as a mixing element, combining LO– and signal power to generate the IF signal (see Section 1.3). In this mode, the frequency of the incoming signal has to be close to that of the LO source. Since the frequency of the LO is known, spectroscopy can be done on the signal by studying the spectrum of the IF output. Key issues of a bolometer as a mixer are its sensitivity (expressed as a noise temperature T_N) and its IF bandwidth.

To design and fabricate an HEBM-based receiver which shows the ultimate in sensitivity and IF bandwidth, it is important to know which parameters are important for device performance and how to vary them to opti-

mize the performance. The theory of a bolometer in direct mode has been reviewed by Richards[1]. Semiconducting bolometer mixers are described by Arams *et al.*[3]. Superconducting HEBMs, however, are relatively new and few models are available: the lumped element approach as described by Prober[4] and Karasik and Elantiev[5] and the hot-spot model by Wilms Floet[6] and Merkel[7] can be found in literature.

In this Chapter we first describe the operation of bolometers in general, followed by a discussion on superconducting HEBMs. To describe bolometers acting as mixers, the hot-spot model is introduced.

2.2 Bolometers

A bolometer is used to measure radiation from the far infrared to the deep UV part of the spectrum. The simplest bolometer is a lens focusing the suns' rays onto a Hg thermometer, measuring the expansion of the Hg. A pyrometer is another type of bolometer, measuring the change in capacitance of a capacitor filled with heat-sensitive dielectric.

2.2.1 Radiation detection

Fig. 2.1 shows a schematic picture of a bolometer. Power is collected in the absorber, which, as a result, rises in temperature. Using a thermometer, the difference in temperature is measured. In the bolometers we use, the absorber acts as a thermometer with a temperature-dependent resistance R(T). This resistance is voltage-biased and a change in resistance leads to a change in bias current, which is detected. Heat build-up in the device is avoided via a thermal link to a heat sink at temperature T_b. Several other implementations of bolometers have been realised in practice. Ref. 1 describes the materials and techniques used in bolometers for infrared and mm waves.

2.2.2 Responsivity and speed

Two important parameters can be identified in a bolometer: its speed and its voltage responsivity S. The latter parameter reflects the change in voltage across the thermometer per Watt of power collected in the absorber. For a

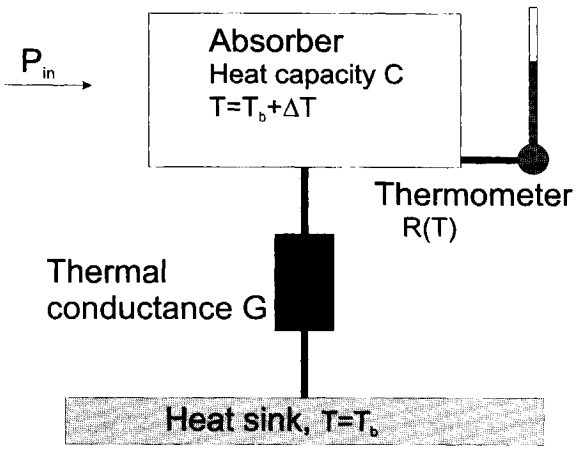

FIGURE 2.1. Schematic picture of a bolometer (after Ref. 8).

bolometer with resistance R, biased with a current I, the voltage responsivity S is given by

$$S = \frac{I\left(\frac{dR}{dT}\right)}{G - I^2\left(\frac{dR}{dT}\right) + i\omega C}, \tag{2.1}$$

with ω the angular frequency of the incoming radiation, C the heat capacitance of the absorber and G the thermal conductance to the heat sink.

The change of resistance with incoming radiation is also 'seen' by the bias current, thus the dc dissipation changes. This results in an effective thermal conductance $G_{eff} = G - I^2 R\alpha$. α is defined as $R^{-1} \cdot (dR/dT)$ and is positive for superconducting bolometers and negative for semiconducting bolometers. In combination with *current* biasing, $\alpha > 0$ can lead to thermal runaway when the denominator of Eq. (2.1) becomes 0.

The speed of the device is determined by the time a bolometer needs to respond to a change in incoming signal. This time is called its thermal time constant τ_{th}. It is given by

$$\tau_{th} = \frac{C}{G_{eff}}. \tag{2.2}$$

At frequencies higher than τ_{th}^{-1}, S drops rapidly, because the system becomes too slow to follow the incoming changes in power.

From Eqs. (2.1) and (2.2) it is clear that a high S comes with a long τ_{th}, thus a slow device. A trade-off must be made between high responsivity and fast response. To maximize S, slow bolometers, intended for direct detection, are built on spider web-like support structures to keep G minimal[2]. On the other hand, in our bolometers, we go at length to minimize τ_{th}, thus increasing G.

2.2.3 Superconducting hot electron bolometer mixers

We use bolometers as a *mixer*, i.e. as a heterodyne detector described in Section 1.3. In this Section the implications of the requirements for a useful mixer (low noise, high IF bandwidth, see Section 1.3) are discussed.

Hot electrons in thin metal films

We exploit so-called hot electrons in our mixers. This effect is present in materials where the interaction between electrons and phonons is weak. In such materials it is possible to add energy to the electron system, e.g. by running a current or radiating it at radio frequency (rf) and hence create an electron system at an elevated temperature. Since there is hardly any interaction between electrons and phonons, the phonons stay at a lower temperature. It is possible to define a temperature for each separate system, thus defining an electron temperature T_e and a phonon temperature T_{ph}. A model of such a system is depicted in Fig. 2.2. The assumption of a low interaction between electrons and phonons is valid at low (~ 10 K) temperature. At room temperature, τ_{e-ph} is so short that the energy is quickly distributed among the electrons and phonons, so equilibrium is reached almost immediately: $T_b = T_{ph} = T_e$.

In order to have a well-defined temperature at any point in the bridge, it is necessary that the energy of the excited electrons is quickly distributed over the other electrons in the bridge. The timescale for this process, the electron-electron interaction time τ_{e-e}, should be shorter than the time it takes for the energy to leave the bridge: $\tau_{e-e} < \tau_{th}$. Usually, the thin films in the dirty limit as used in this work have a short τ_{e-e}, fulfilling the criterion $\tau_{e-e} < \tau_{th}$ in a practical bridge.

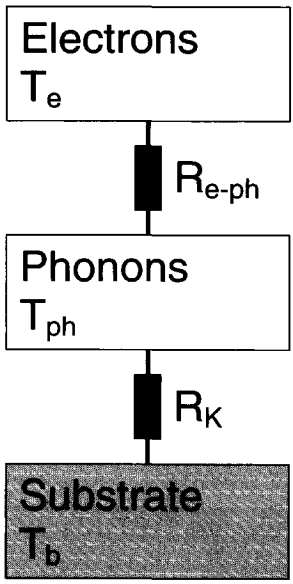

FIGURE 2.2. The thermal subsystems in a hot electron system. Energy between electrons and phonons is exchanged via electron-phonon interactions. The thermal resistance is represented by R_{e-ph}. The heat exchange between phonons in the film and those in the substrate occurs via the Kapitza-resistance R_K.

In superconductors the current is carried by Cooper pairs. Radiation with a photon energy below the gap energy cannot break Cooper pairs. At these frequencies, radiation is absorbed by quasi-particles: excitations from the ground state. Radiation above the gap energy breaks Cooper pairs into quasi-particles. Energy larger than the energy gap is used to excite the newly created quasi-particle higher above the gap: a hot electron is created. If we assume a short τ_{e-e} and a decoupled phonon system, this electron quickly shares its energy and many hot electrons are created, each having their share of the first excited electrons' energy. It should be noted that the phonon system can be at a temperature lower than T_c, while T_e is above that.

Using hot electrons it is possible to bring the electron system at a temperature above T_c and drive the superconducting bridge into a resistive state by

applying a dc current or rf radiation. Under the right operating conditions, not the entire bridge is driven into a normal state. Therefore, applying more power drives the bridge into a more resistive state: a detector! In Section 2.3 we will refine this picture.

Bolometer mixers do not measure the change in current induced directly by photon-assisted tunneling as in an SIS-tunnel junction. Rather, the incoming ac field accelerates the electrons, thus adding energy. Due to the short electron-electron scattering time τ_{e-e} the energy is quickly distributed. This mechanism makes a bolometer independent of the energy (i.e. frequency) of the incoming radiation, provided that the energy of the radiation is above the superconducting gap.

Phonon– and diffusion cooled HEBMs

In view of the requirements on IF bandwidth (see Section 1.3), two routes have been taken to develop superconducting HEBMs. One uses the phonon-cooled HEBM, usually based on NbN as the superconducting material, the other is the diffusion cooled HEBM, mostly exploiting the superconducting properties of Nb, although NbC[10], Al[11] and, recently, bilayers of Nb/Au[12] have been investigated.

The former uses ultrathin (~ 3 nm) NbN layers sputtered onto a Si or MgO substrate. Their strong electron-phonon interaction gives these films a relatively high T_c and a high (theoretically about 10 GHz) bandwidth. In recent years, these devices have shown the highest sensitivity for HEBMs in the range 0.5–5 THz[13,14]. Experimental IF bandwidth in this type of devices is as high as 3-4 GHz on Si wafers and has recently been increased to 4.6 GHz on MgO[15]. The latest development in this type of detector is the use of NbTiN[16].

The diffusion-cooled hot electron bolometer, proposed by Prober[4], uses the out-diffusion of electrons to remove energy from the nanobridge. Devices of this type are shorter than the electron-phonon interaction length (or thermal healing length) $\lambda_{th} = \sqrt{\tau_{e-ph}D}$, with D the diffusion constant. In practice, this means that electrons will diffuse out of the bridge before they have a chance to interact with phonons. In this thesis, diffusion-cooled bolometers are studied.

The IF bandwidth $f_{3\,dB}$ is given by

$$f_{3\,dB} = \frac{1}{2\pi\tau_{diff}}, \tag{2.3}$$

where, in a fully metallic strip and assuming diffusion cooling, the diffusion time τ_{diff} is given by[17]

$$\tau_{diff} = \frac{L^2}{\pi^2 D}. \tag{2.4}$$

Fig. 2.3 shows the calculated IF bandwidth $f_{3\,dB}$ as a function of bridge length based on a typical Nb thin film (12 nm thick with $D = 1.6 \cdot 10^{-4}\ m^2/s$). From an application-point of view, a $f_{3\,dB}$-value of around 8 GHz is required. This implies a device length of about 150 nm. Fabrication of devices this small requires the use of electron beam lithography (EBL), see Ch. 5. Burke *et al.*[18] have experimentally shown this length dependence of the IF frequency. Furthermore, they show the transition from phonon-cooling to diffusion cooling upon increasing bridge length.

2.3 The lumped element model

Refs. 4 and 5 have suggested a simple model to describe the thermal properties of diffusion-cooled HEBMs. In this model, it is assumed that the whole bridge is at the same temperature T and is operated in the middle of the transition. Beatings (with frequency $IF = |\omega_{LO} - \omega_{sig}|$) in the incoming LO and signal cause the temperature of the bridge to deviate, thus changing its resistance. A detector employing the critical transition of a superconductor is a called transition-edge sensor (TES).

A more realistic thermal model has been proposed by Burke[19] and Wilms Floet *et al.*[6]. Instead of assuming the whole bridge to be at the same temperature, they assume a temperature profile in the electron system of the bridge. The phonon system is assumed to be at T_b. Since the cooling pads are bulky and well connected to the bath, these are assumed to be at the bath temperature. Due to the dc and rf power supplied to the bridge, the electrons in the center of the bridge are at the highest temperature. If this temperature is higher than T_c, a normal region will develop in the bridge: a so-called electronic hot spot[6]. In operating conditions, small changes in

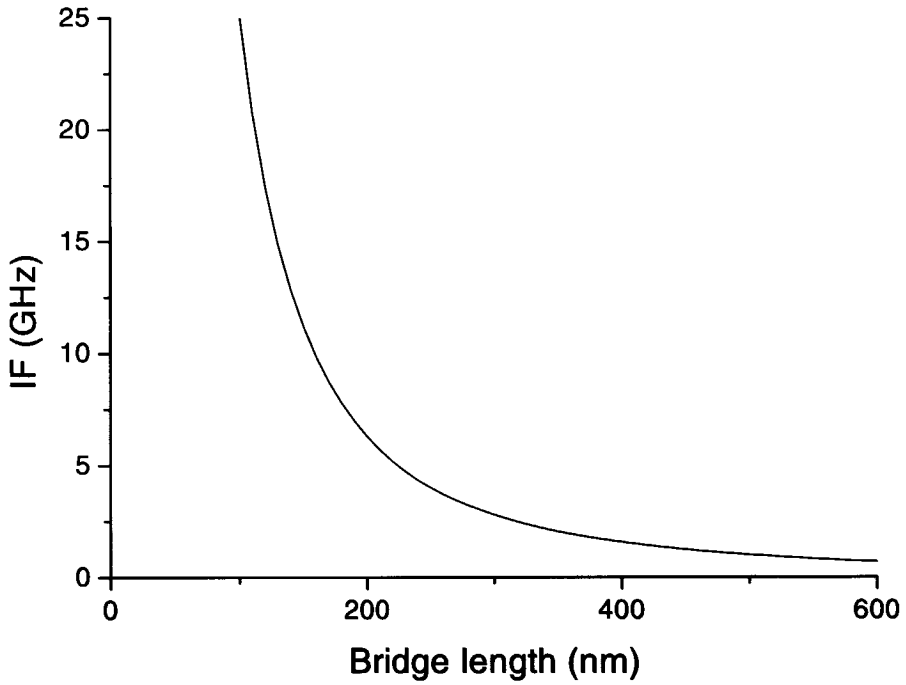

FIGURE 2.3. Length dependence of the IF bandwidth in Nb HEBMs. The diffusion constant D is taken to be $1.6 \cdot 10^{-4}\,\mathrm{m^2 s^{-1}}$.

incoming power at the IF frequency result in a modulation of the hot spot length and therefore in a modulation of the resistance of the device. The corresponding current modulation can be detected and further amplified.

2.4 The hot-spot model

To properly describe the I(V)– and gain vs V-curve (G(V)) of an HEBM, the hot spot model starts with calculating the temperature profile of the electrons in the bridge as a function of dc and rf power. Knowing this profile, one can deduce the I(V)-characteristics as well as the devices' gain.

To describe the heat transport in the nanobridge, a heat balance equation

is set up. In the superconducting parts of the bridge, we have

$$-K\frac{d^2T}{dx^2} + \frac{c_e}{\tau_{e-ph}}(T - T_b) = p_{rf} \tag{2.5}$$

and within the hot spot we have:

$$-K\frac{d^2T}{dx^2} + \frac{c_e}{\tau_{e-ph}}(T - T_b) = j^2\rho + p_{rf}. \tag{2.6}$$

In these equations, p_{rf} is the rf power density, K is the thermal conductivity (assumed to be independent of x, i.e. T), T the electron temperature and x the coordinate along the bridge. The first term in these equations describes the out-diffusion of heat. The second term, with c_e the electronic heat capacity, describes the energy transfer to the phonons. Both these terms describe the outflow of heat from the system. The last two terms of Eq. (2.6) describe the input of power. The current density j and the resistivity ρ determine the dc heating within the hot spot. The rf radiation p_{rf} is absorbed throughout the bridge, because a frequency higher than the gap-frequency is assumed.

Solving these equations for T(x) gives the temperature profile in the bridge. Fig. 2.4[a] shows the temperature distribution of the electrons in the bridge for high and low power levels of the beatings. In the middle, the temperature is higher than T_c, the critical temperature of the bridge. In this area, a normally conducting regime is formed: an electronic hot spot. Fig. 2.4[c] shows the beatings in incoming power (see Section 1.3). These cause the hot spot to oscillate as is indicated in Fig. 2.4[b].

Eqs. (2.5) and (2.6) can be solved using textbook expressions and –values for c_e, K and τ_{e-ph}[6,8]. To obtain the boundary conditions for this system, the cooling pads are assumed to be at a constant temperature T_b and the flow across the normal-superconductor interface needs to be constant. This is guaranteed by matching K(dT/dx) on both sides of the interface.

From the modeled temperature profile, the length of the hot spot is calculated. From that, the resistance of the bridge can be calculated. Assuming a voltage bias, the current density $j(L_h, p_{rf})$ can be calculated, where L_h is the hot spot length and p_{rf} the rf power density absorbed in the bridge. $j(L_h, p_{rf})$ can be converted into an I(V)-curve when the exact geometry is known. Obviously, this can be done for several p_{rf}, i.e. levels of LO power.

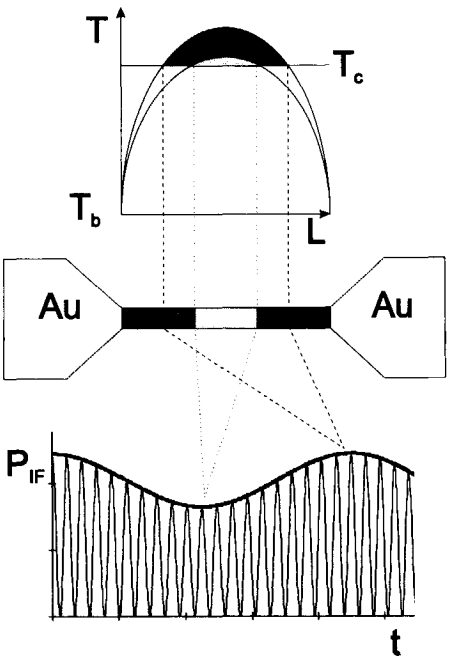

FIGURE 2.4. [a] Profile of T_e as a function of distance in the bridge. [b] Top view of the nanobridge, indicating normal (shaded) and superconducting (black) regions. [c] Beatings (at IF, thick line) in the radiation coupled to the bridge. The thin line represents the signal– and LO power at rf.

When calculating I(V)-curves for increasing LO power, $\frac{d^2I}{dV^2}$ at low bias changes from positive to negative. This change occurs at the power level where the LO power alone can just sustain the hot spot.

2.4.1 Voltage responsivity and conversion gain

We argued above that a HEBM is not a transition edge sensor and therefore we use dL_h/dp_{rf} as the quantity that changes with incoming power. The voltage responsivity at low frequency S(0) can then be derived to be

$$S(0) = I\left(\frac{dR}{dp_{rf}}\right) = j\rho\left(\frac{dL_h}{dp_{rf}}\right), \tag{2.7}$$

we can calculate it once the pumped I(V)-curve is known. S(0) gives the change in voltage over the nanobridge per Watt of power absorbed in the device.

The mixer gain G_{Mix} is given by the ratio of the output power of the mixer and the signal power delivered to the device:

$$G_{Mix} = \frac{P_{IF}}{P_{sig}}. \tag{2.8}$$

In more detail, the gain of the mixer is given by[19]

$$G_{Mix}(f) = 2\frac{P_{LO}}{R_N}\frac{S(0)^2}{1+\left(\frac{f}{f_{3\,dB}}\right)^2}, \tag{2.9}$$

in which R_N is the resistance of the device and $f_{3\,dB}$ is the cut-off frequency. G_{Mix} depends on the LO power P_{LO}, normal state resistance and the voltage responsivity.

The bottom panel of Fig. 2.5 shows pumped I(V)-curves of a typical device for LO power levels of 30, 50 and 70 nW. With increasing LO power, the current through the device is increasingly suppressed, a result of the growing hot spot. The top panel shows the gain vs V for the same operating conditions. In general, the effects of electro-thermal feedback (ETF) as described by Ref. 20 should be taken into account in these calculations.

The figure shows values for G_{Mix} that peak far above 0 dB. This gain-regime is reached in operating conditions where the differential resistance is negative. In practice, however, the device cannot be stably biased in this range.

2.4.2 Intermediate bandwidth

One of the main drivers to develop diffusion cooled HEBMs has been to improve the IF bandwidth. In this Section, the behavior of the IF bandwidth is described in terms of the hot spot model. For a metallic bridge, the diffusion time τ_{diff} is given by Eq. (2.4). In this expression, the temperature profile is taken into account, but D is constant throughout the bridge. However, as described above, in operating conditions an electronic hot spot is formed in the middle of the bridge, leaving two superconducting bridge ends. In a metallic strip, D is given by the ratio of the thermal conductivity K and the

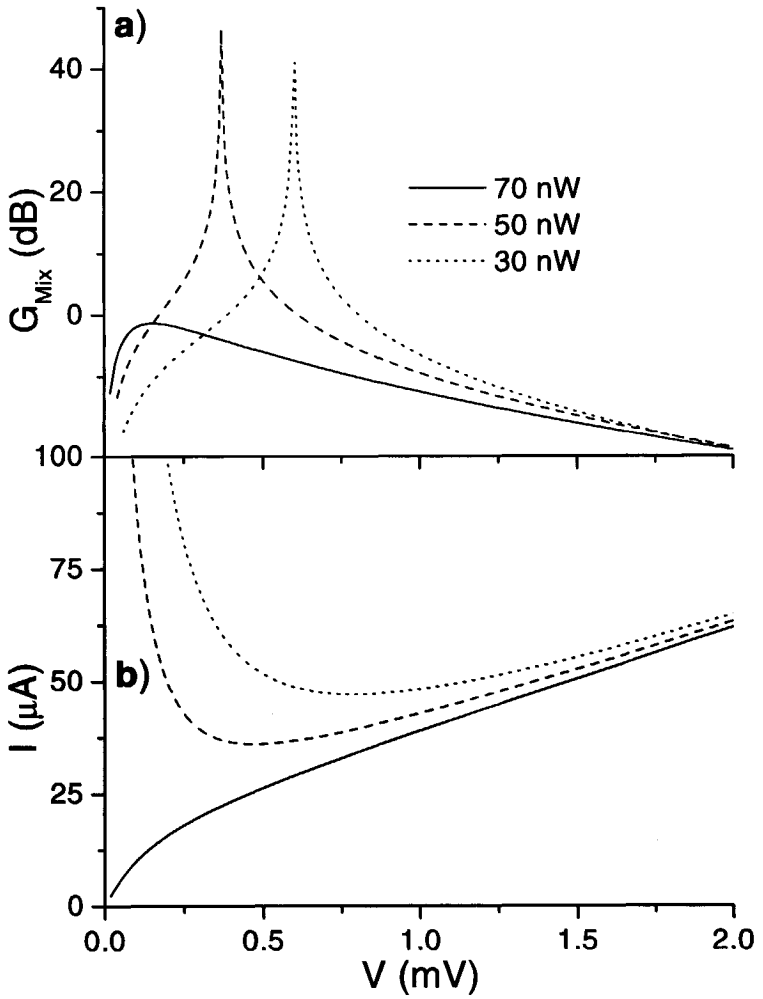

FIGURE 2.5. [a] Gain curves for an HEBM with length L = 250 nm, width w = 100 nm and thickness t = 12 nm. We assume a bath temperature $T_b = 4.7$ K and a critical temperature $T_c = 7.0$ K. The curves are calculated for 30 nW (dotted), 50 nW (dashed) and 70 nW (solid). [b] Pumped I(V)-curves and corresponding power levels for the same device.

electronic heat capacity c_e: $D = K/c_e$, which is independent of T, since both K and c_e increase linearly with T. In the superconducting ends of the bridge, c_e is larger than in the normal state. On the other hand, K decreases, since $K \propto T^2 e^{-1.76T_c/T}$. The decrease of K and the increase of c_e cause D to drop when going from a normal to a superconducting region, assuming that D is still given by K/c_e. From this reasoning, one can see that the IF bandwidth will increase upon increasing P_{LO} or increasing the bias voltage. IF bandwith is not only determined by the geometry (length) of the device, but also by its operating point. For a complete discussion, the effects of ETF should be taken into account as well.

2.4.3 Noise temperature

We will express the sensitivity of the mixers as a noise temperature T_N at the input of the device, as is common in this field. In this approach, the mixer itself is regarded as a lossless element with a noise source at temperature T_N in front of it. This way of expressing the sensitivity allows a comparison of signal strength and integration time needed for various mixers.

This noise temperature is given by

$$T_{Mix} = \frac{T_{out}}{G_{Mix}} \tag{2.10}$$

in which T_{out} is the noise measured at the output of the device. T_{out} consists of two terms: the Johnson noise T_J and the electron fluctuation noise T_{EFN}. In the optimal bias range, the latter dominates T_{out} in HEBMs[5].

The equivalent Johnson noise temperature of a resistor equals its temperature T_e and has a white spectrum. Since, in HEBMs, $T_J \ll T_{EFN}$, we will digress on the electron fluctuation noise here.

Thermal fluctuation noise

In a system at temperature T_b, in thermal equilibrium via a heat conductivity G, the spectral density of the temperature fluctuations is given by $\delta T^2 = 4k_B T_b^2/G$ [21]. The superconducting nanobridge can be considered as such a system. The temperature fluctuations cause the hot spot to grow and shrink accordingly. The equivalent output noise due to thermal fluctuation

noise at IF (i.e. in front of the IF amplifier) is given by[22]

$$T_{EFN} = \frac{1}{k_B} \frac{I_0^2 \cdot R_L}{(R_L + R_{b0})^2} \cdot \left[\frac{1}{1 - C_{dc} \cdot I_0^2 \cdot \frac{R_L - R_{b0}}{R_L + R_{b0}}} \right]^2 \cdot \left(\frac{dR}{dT} \right)^2 \cdot \frac{4k_B T_e^2}{c_e V} \cdot \tau_{th}. \tag{2.11}$$

In this equation, k_B is Boltzmann's constant, I_0 is the bias current, R_{b0} is the device resistance in the operating point due to dc bias and time-averaged rf radiation, R_L represents the load resistance, C_{dc} is the change in resistance due to dc bias, V the device's volume and c_e is the electronic heat capacity. Within the hot spot model, dR/dT is calculated from the electron temperature profile. A small increase in electron temperature ΔT_e gives rise to a total change in hot spot length $\Delta H = (2/(dT_e/dx|_{T_c}) \cdot \Delta T_e$. (N.B. here, we assume that a *small* temperature increase leaves the temperature profile unchanged in shape and only lifts the profile, thereby moving the S/N boundary by $\Delta x = (1/(dT_e/dx)) \cdot \Delta T_e$.) The change in resistance is then given by

$$\Delta R = R_N \cdot \frac{\Delta H}{L} = 2\frac{R_N}{L} \cdot \frac{1}{\frac{dT_e}{dx}\Big|_{T_c}} \cdot \Delta T_e, \tag{2.12}$$

assuming a bridge length L.

The resistance change dR due to a small change temperature dT_e is given by

$$\frac{dR}{dT_e} \approx \frac{\Delta R}{\Delta T_e} = 2 \cdot \frac{R_N}{L} \cdot \frac{1}{\frac{dT_e}{dx}\Big|_{T_c}}. \tag{2.13}$$

Inserting Eq. (2.13) into 2.11 gives for T_{EFN}[23]:

$$T_{EFN} = \frac{1}{k_B} \frac{I_0^2 \cdot R_L}{(R_L + R_{b0})^2} \cdot \left[\frac{1}{1 - C_{dc} \cdot I_0^2 \cdot \frac{R_L - R_{b0}}{R_L + R_{b0}}} \right]^2 \cdot \left(2 \cdot \frac{R_N}{L} \cdot \frac{1}{\frac{dT_e}{dx}\Big|_{T_c}} \right)^2 \cdot \frac{4k_B T_e^2}{c_e V} \cdot \tau_{th}. \tag{2.14}$$

This equation takes into account the EFN. If the device and the IF chain do not have the same impedance, a correction for the mismatch should be made for both T_J and T_{EFN}.

Typical values for T_{EFN} in lowest-noise bias conditions are around 50 K — an order of magnitude larger than the value of T_J. In a long (relative to bridge length) hot spot, the slope of the T_e is large, which results in a low sensitivity of the resistance to changes in temperature, in turn causing a low contribution to the noise temperature. However, a high conversion gain requires a high sensitivity to a change in temperature. To get low mixer noise (the ratio of T_{out} and G_{mix}), a compromise needs to be found.

2.5 Discussion

A validation of these models is expected from a comparison to experiments performed on nanobridges. Merkel *et al.*[23] have shown such a comparison for phonon-cooled devices and Wilms Floet *et al.*[8] did so for diffusion-cooled HEBMs. In this thesis, the comparison to the model and the experiment is discussed in Ch. 8 and 9.

Qualitatively, the model describes the experimentally obtained data quite well, especially the I(V)– and behavior of the G(V)-curve. However, as far as noise temperature and gain are concerned, the observed differences between model and experiments suggests that more work needs to be done to fully understand superconducting HEB mixers.

References

[1] P.L. Richards, J. Appl. Phys. **76**, 1 (1994).

[2] J.J. Bock, D. Chen, P.D. Mauskopf and A.E. Lange, Space Science Review **74**, 229 (1995).

[3] F. Arams, C. Allen, B. Peyton and E. Sard, Proc. IEEE **54**, 612 (1966).

[4] D.E. Prober, Appl. Phys. Lett. **62**, 2119 (1993).

[5] B.S. Karasik and A.I. Elant'ev, Appl. Phys. Lett. **68**, 853 (1996).

[6] D. Wilms Floet, E. Miedema, T.M. Klapwijk and J.R. Gao, Appl. Phys. Lett. **74**, 433 (1999).

[7] H.F. Merkel, E.L. Kollberg and K.S. Yngvesson, Proc. 9th Int. Symp. Space THz Techn., Pasadena, CA, March 17-19, pp. 81-97 (1999).

[8] D. Wilms Floet, *Hotspot Mixing in THz Niobium Superconducting Hot Electron Bolometer Mixers*, Ph. D. thesis, Delft University of Technology (2001).

[9] E.M. Gershenzon, G. Gol'tsman, I.G. Gogidze, Y.P. Gusev, A.I. Elant'ev, B.S. Karasik and A.D. Semenov, Sov. Phys. Superc. **3**, 1582 (1990).

[10] B. S. Karasik, K. S. Il'in, E. V. Pechen, S. I. Krasnosvobodtsev, Appl. Phys. Lett. **68**, 2285 (1996).

[11] A. Skalare, W.R. McGrath, P.M. Echternach, H.G. LeDuc, I. Siddiqi, A. Verevkin, D.E. Prober, Proc. 11th Int. Symp. Space THz Techn., Ann Arbor, MI, May 1-3, pp. 501-512 (2000).

[12] P. Yagoubov, X. Lefoul, W.F.M. Ganzevles, J.R. Gao, P.A.J. de Korte and T.M. Klapwijk, to appear in Proc. 12th Int. Symp. Space THz Techn., San Diego, CA, Feb. 14-16 (2001).

[13] P. Yagoubov, M. Kroug, H. Merkel, E. Kollberg, J. Schubert, H.-W. Hübers, S. Svechnikov, B. Voronov, G. Gol'tsman and Z. Wang, Proc. Europ. Conf. on Appl. Superconductivity (EUCAS '99), Barcelona, September 14-17 (1999).

[14] J. Schubert, A.D. Semenov, G. Gol'tsman, H.W. Hübers, G. Schwaab, B. Voronov, E. Gershenzon, Proc. 10th Int. Symp. Space THz Techn., Charlottesville, March 16-18, pp. 190-199 (1999).

[15] S. Cherednichenko, M. Kroug, P. Yagoubov, H. Merkel, E. Kollberg, K.S. Yngvesson, B. Voronov and G. Gol'tsman, Proc. 11th Int. Symp. Space THz Techn., Ann Arbor, MI, May 1-3, pp. 219-227 (2000).

[16] C.E. Tong, J. Stern, K. Megerian, H. LeDuc, T.K. Sridharan, H. Gibson, and R. Blundell, to appear in Proc. 12th Int. Symp. Space THz Techn., San Diego, CA, Feb. 14-16 (2001).

[17] H.S. Carslaw and J.C. Jaeger, *Conduction of Heat in Solids*, Clarendon Press, Oxford (1959).

[18] P.J. Burke, Appl. Phys. Lett. **68**, 3344 (1996).

[19] P.J. Burke, *High Frequency Electron Dynamics in Thin Film Superconductors and Applications to Fast Sensitive THz Detectors*, Ph. D. thesis, Yale University (1997).

[20] D. Wilms Floet, T.M. Klapwijk, J.R. Gao and P.A.J. de Korte, Appl. Phys. Lett. **77**, 1719 (2000).

[21] C. Kittel and H. Kroemer, *Thermal Physics*, Freemand and Co. (1980)

[22] K.S. Yngvesson and E.L. Kollberg, Proc. 10th Int. Symp. Space THz Techn., Charlottesville, VA, March 16-18, pp. 566-591 (1999).

[23] H.F. Merkel, P. Khosropanah, D. Wilms Floet, P.A. Yagoubov and E.L. Kollberg, IEEE Trans. Microwave Theory and Techn. **48**, 690 (2000).

Chapter 3

Quasi-optical coupling circuits

To obtain high sensitivity in (heterodyne) receivers, it is important to couple the signal from the outside world effectively into the nanobridge at ℓHe-temperatures. Several methods to do this are described in literature[1–3], which are briefly described in this chapter. We discuss waveguide– and quasi optical coupling, on-chip transmission lines and some basic microwave concepts. For a more detailed discussion, see for example Refs. 2, 4 and 5.

3.1 Waveguide coupling

Before describing quasi-optical techniques, we shortly review waveguide-coupling circuits. These are often used in SIS-receivers below 1 THz and have desired properties for application of a receiver in a telescope.

Fig. 3.1[a] shows a photograph of a split-block waveguide mount designed for frequencies around 0.7 THz. This waveguide is produced by H. Schaeffer at the laboratory of the Space Research Organization of the Netherlands, Groningen[1,6]. A polyethylene (PE) lens focuses the radiation into the diagonal horn, which couples it into the waveguide. The waveguide is dimensioned such that, in the frequency range of interest, only one mode exists within the waveguide. For this frequency range that means that the width and height of the waveguide are 300 μm and 150 μm, respectively.

The mixer, fabricated on a quartz substrate, is put in the substrate channel in such a way that the rf probes of the mixer symmetrically stick into the waveguide, as is depicted in Fig. 3.1[b]. To avoid substrate modes (which allow signal to leak into the substrate), the substrate is kept very

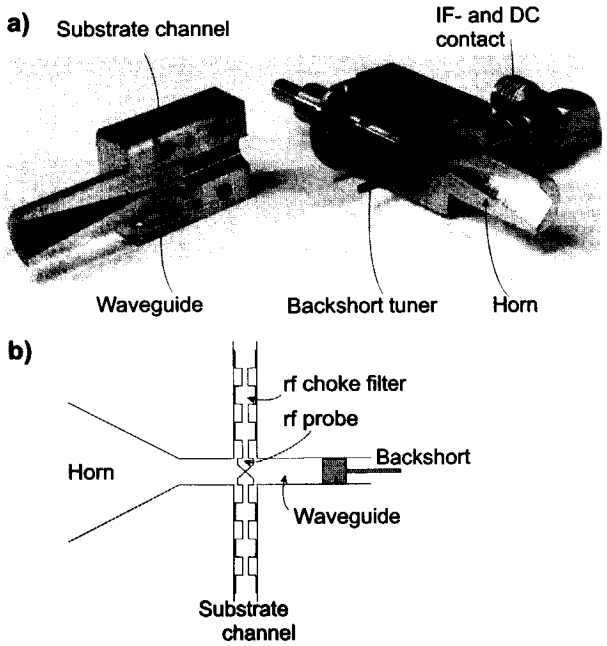

FIGURE 3.1. [a] Photograph of a waveguide mixer mount fabricated at SRON. This mixer is designed for use around 0.7 THz and has a mechanical tuner. Nowadays, fixed-tuned waveguides are commonly used. [b] Schematic cross-section of the waveguide mixer with backshort tuner.

thin (less than $1/4\ \lambda_{\text{eff}}$, about 35 μm at 1 THz).

At the end of the waveguide, a metal backshort reflects the radiation back onto the mixer probes. The distance from this tuning element to the probes is chosen such that the coupling of the signal to the mixing element is optimal. In the initial mixers, it was necessary to optimize the position of the mirror while operating the mixer. Nowadays, due to a better understanding of both waveguide and on-chip tuning structures, fixed-tuned waveguides are used.

Waveguides show very low losses, especially the fixed-tuned waveguides. Employing SIS mixers as the mixing element in waveguides, excellent sensitivity is obtained up to 1 THz[7]. This narrow bandwidth reduces the satura-

tion in the device. Another clear advantage of using waveguides is its beam pattern, which is very clean and well defined. This is a desirable property for application in a telescope.

When waveguides are used at higher frequency, the dimension of the waveguide, substrate channel and substrate need to be reduced accordingly. Above about 1.5 THz, this poses problems in the production of the waveguides and device handling. Next to quartz, only few other substrates can be used in a waveguide, as these materials generally have too high a dielectric constant ϵ_r. (The high ϵ_r makes the required physical thickness even smaller, since the effective wavelenght scales with $1/\sqrt{\epsilon_r}$.) This might be a hindrance for using high-T_c– or semiconductor bolometers (which can be fabricated on certain substrates only) in a waveguide coupling scheme.

Although difficult, production and operation of waveguide mixers well above 1 THz is possible[8]. An easier way to couple radiation to the mixing element at high frequency is the quasi-optical coupling scheme.

3.2 Quasi-optical mixers

In the QO setup, one uses a lens to focus the signal from free space onto the mixer chip (or die). This idea has originally been introduced in this field by Rutledge and Muha[9]. The planar antenna is placed directly on the back of a dielectric lens. If the dielectric constant ϵ_r of the lens is close to that of the antenna substrate, no substrate modes will exist. Another advantage of this configuration is that most of the power will be radiated into the dielectric: the ratio of powers radiated into the dielectric and into air is approximately $(\epsilon_r/\epsilon_{air})^{3/2}$ for the slot-antennas used in this work. For Si (having $\epsilon_r = 11.7$), only 2–3% of the radiation is lost into the air-side of the system. Additionally, dielectric lenses can produce high-quality Gaussian beams that can be coupled efficiently to a quasi-optical telescope.

A sketch of the lens-chip combination is shown in Fig. 3.2. The die is glued to the lens using bees' wax or superglue. On the chip, a planar antenna is located, usually a spiral– or slot antenna. The antenna picks up the radiation that is focused onto it. Some antennas, like the spiral– and log periodic antenna, connect to the nanobridge directly (see Fig. 8.1), others need a transmission line to couple the signal from the antenna feedpoint to the nanobridge, as is visible in Fig. 9.1. This is the case for the twin slot

antenna used mostly in this work.

Good mixer sensitivities have been obtained using quasi-optical coupling in the frequency range 0.5-5 THz and above 1 THz it is the technology of choice[5,7,10–12].

Furthermore, since the rf impedance of an HEB is frequency independent, the bandwidth of the receiver is determined by the element with the narrowest bandwidth. Combined with a wideband antenna like a spiral– or log periodic antenna, the frequency range 0.3-3 THz can be spanned in one device. To explore the device performance, e.g. its sensitivity and IF bandwidth at various frequencies, applying such antennas offers great advantages.

The open structure of the quasi-optical configuration makes fabrication and handling of the lens and its mount relatively easy. Much space is available for contacting the device and adding peripheric equipment like magnet coils, thermometers and heaters. Fabrication is less difficult than that of waveguide mounts: size– and alignment tolerances are virtually absent. Furthermore, mounting a quasi-optical device is less critical because the dies are larger and thicker, so less vulnerable to damage. Die alignment requires a relatively simple XY-table with micrometers and microscope, whereas mounting a waveguide device calls for much skill, experience and patience.

The requirement that devices need to be fabricated smaller with increasing frequency also holds for quasi-optical devices. In this case, well-established (sub)microlithographic techniques offer high control and flexibility in fabricating the rf structures.

3.3 Quasi-optical lens configurations

Fig. 3.3 shows three different types of lenses that have been used for quasi-optical receivers: a hemispherical [a], a hyperhemispherical [b] and an elliptical lens [c]. All pictures are drawn assuming the geometrical optics-limit. Quasi-optical beams would diverge coming out of the lens.

The extended hemispherical lens has been subject of several studies, both experimental and theoretical[13–15]. The extended hemisphere is a hemisphere with radius R and an extension of length l. Its directivity strongly depends on the length l, especially at higher frequency. The coupling efficiency to a Gaussian beam is high up to an intermediate position between the hyperhemisphere (see below) and synthesized elliptical lens (an extended

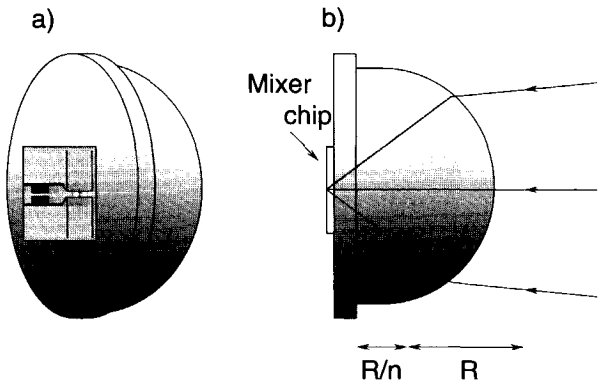

FIGURE 3.2. [a] Sketch of the quasi-optical setup. The mixer chip is glued to a hyper-hemispherical or elliptical Si lens. This narrows the wide beam from the planar antenna to a narrow (few degrees) beam that can be coupled to a telescope. [b] The detector, here incorporating a twin slot antenna, is defined on the mixer chip. The IF matching board is not shown. The flanges on the lens are used to assure good thermal contact when clamping the lens to the Cu mixer block.

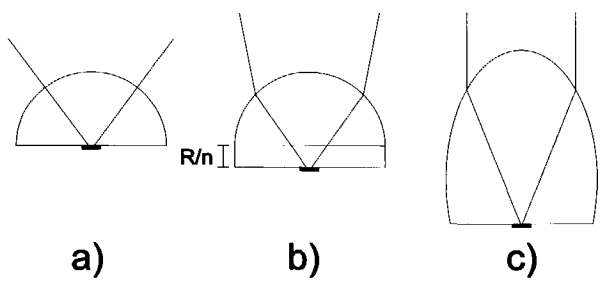

FIGURE 3.3. Different types of lenses used in quasi-optical coupling schemes. [a] hemispherical, [b] hyperhemisperical and [c] elliptical.

hemisphere with l=0.38 R). In practice, a trade-off between directivity and Gaussian efficiency is found for an extension length between that of the hyperhemisphere and the synthesized ellips.

A hyperhemispherical lens reduces the beam witdth by a factor of n, n being the index of refraction of the lens[16] (note that this lens is a special case of the extended hemisphere described above). This configuration is a hemispherical lens with an extension length R/n from the sphere's center, in which R is the radius of the lens. Often, an objective lens is placed in front of the hyperhemisphere to narrow the beam emerging from the lens even more to couple effectively to a telescope.

An elliptical lens is an efficient configuration because an antenna placed on the back of the lens (in its second focus) will be diffraction-limited by the aperture of the lens. This configuration is compatible with imaging systems having a large f-number, because it can achieve very narrow beam patterns[14]. A drawback of this lens is the larger effective reflection coefficient at the lens/air interface. This is due to the large range of incident angles.

In this work, we have used a synthesized elliptical lens. This lens is fairly easy to produce, while its properties fulfill the laboratory needs: our main focus is on direct response and device performance rather than the optimization of other device properties such as beam pattern. In that case, one obviously needs the full advantage of the elliptical lens.

3.4 Planar antennas

Using a lens, it is possible to transform the broad beam of the planar antenna into a much narrower beam that couples efficiently to the telescope. In this Section, we will describe some planar antennas that are widely used in submm receivers.

Planar — or printed — antennas are essentially 2-dimensional structures that are lithographically printed on either a membrane (freestanding antennas) or on a dielectric. The size of the essential elements in such an antenna usually is a large fraction of the wavelength. For example, at 2.5 THz (with free-space wavelenght λ_0 equal to 120 μm), the typical length of a twin slot antenna is 39 μm.

Antennas can be divided into two classes: resonant and non-resonant (or travelling wave) antennas. Dipoles and slots — either single, double

(or twin) or even multiple — are usually operated as resonant antennas. Bow ties, spirals and log-periodic antennas are non-resonant. The main property of the latter is the wide bandwidth, that of the former is its narrow bandwidth.

For the characterization of HEBMs, a large bandwidth usually is preferable: one device can be investigated throughout the submm (0.3-3 THz) region. However, the large bandwidth might cause saturation in the nanobridge, since it is rather sensitive to direct detection. Furthermore, the beam– and polarization properties of the wideband antennas available are not as good as those of resonant antennas.

Some of the properties of several types of planar antennas will be described below. For more details, see Refs. 2, 5, 13 and 17.

1. The *spiral antenna* is a member of a class of antennas that — theoretically — has properties like impedance Z_{ant} and beam pattern that do not change with frequency. When a self-complementary design is used, $Z_{ant} = Z_0/\sqrt{2(1+\epsilon_r)}$. On Si, $Z_{ant} = 75\,\Omega$. Unfortunately, it is hard to fabricate Nb HEBMs that match well to this rather high antenna impedance. In many applications it is a drawback that this type of antenna polarization has circular polarization. Otherwise, the bandwidth of the spiral antenna are well suited for device characterization provided that certain modifications are implemented to physically match the nanobridge and cooling pads to the antenna arms[18].

2. The *log-periodic* antenna is a wideband antenna, theoretically its impedance and gain are flat with frequency. The design that is commonly used is self-complementary, as is the design of the spiral antenna. In this antenna, the — linear — polarization of this antenna oscillates over a fixed angle ϕ upon a change in frequency. ϕ depends on the exact geometry of the antenna at hand. The nature of this antenna provides a more natural transition from the antenna arms to the cooling pads than does the spiral antenna. In both these antennas, however, the signal is directly fed from the antenna to the cooling pads and nanobridge, i.e. no transmission line is necessary to couple the antenna to the bridge.

3. *Double slot* antennas are complementary to double dipoles. Their bandwidth, gain, sidelobe– and cross polarization levels are compa-

rable. Z_{ant} of a double slot is some 50% lower than that of the double dipole. This property makes it a suitable antenna for use in (low-impedance) Nb HEBMs. The double slot does not need a backplane reflector, thus reducing the complexity of the system. As does the double dipole, a double slot needs a transmission line to couple radiation to the mixing element. Both CPWs and microstrip lines have been suggested in literature[5,15]. For HEBMs using a double slot antenna however, only CPW lines have been reported in literature[3].

3.5 On-chip transmission lines: CPW and microstrip lines

HEBMs using twin-slot slot antennas rely on co-planar waveguide transmission lines (CPW)[3,19,20] to couple the radiation from the antenna to the superconducting bridge. This technology has proven to work up to 2.5 THz, in both waveguide– and QO-coupled mixers. In SIS-mixers, the use of microstrip line transmission lines is widespread, using both normal metal and superconducting conductors. Their success has been extensively shown up to about 1 THz[5,21], and recently, 1.2 THz SIS mixers have been shown[22]. For this work, the requirements on the transmission line are that they should provide a low-loss, easy-to-design and easy-to-produce means of coupling the signal to the nanobridge.

In this work, both CPW– and microstrip lines have been used to couple the antenna to the mixing element. A CPW design was readily available in literature, and this design has been proven to work up to 2.5 THz[3]. The microstrip line transmission line is a novel design in this field. Technology to produce this type of device has been developed to verify the new concept.

Both CPWs and microstrip transmission lines are used to transport rf radiation. In Fig. 3.4, it can be seen that CPW is a 2-dimensional structure. The metal strip in the middle is called the center conductor, both large metal planes next to it form the ground plane. Fig. 3.5 shows a microstrip line transmission line. This is a stacked (or 3-dimensional) structure. The large bottom plane is ground, the top wiring layer lies above a dielectric separator.

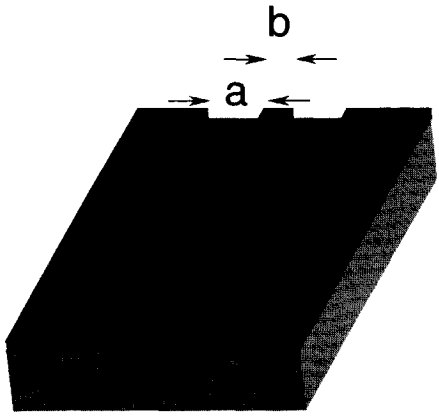

FIGURE 3.4. Schematic picture of a co-planar waveguide transmission line. a and b represent the slot– and center conductor width, respectively.

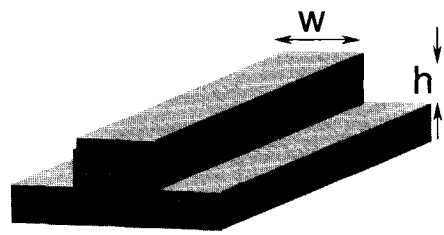

FIGURE 3.5. Schematic picture of a microstrip line. h and w give the thickness of the SiO_2 and the top wiring width, respectively.

3.5.1 Microstrip line characteristics

A good impression of the general properties of microstrip transmission lines can be obained from a description in the so-called ladder representation. A piece of microstrip line is sketched in Fig. 3.5. It consists of a ladder of series impedances and shunt admittances. $\tilde{R}$ is the series resistance, $\tilde{L}$ is the series inductance, $\tilde{G}$ represents the shunt conductance and $\tilde{C}$ the shunt capacitance. These are all distributed quantities, measured per unit lenght, see, e.g. Ref. 23. In such a representation, the impedance Z is given by $Z = \tilde{R} + i\omega\tilde{L}$, the admittance Y by $Y = \tilde{G} + i\omega\tilde{C}$, with ω the angular frequency. Voltage and current are related by

$$\frac{dV}{dx} = -ZI \tag{3.1}$$

and

$$\frac{dI}{dx} = -YV, \tag{3.2}$$

where x is the coordinate along the line.

These equations have solutions of the form

$$V(x) = V(0)e^{-\gamma x}, \tag{3.3}$$

$$I(x) = I(0)e^{-\gamma x}. \tag{3.4}$$

$\gamma = \alpha + \imath\beta$ is the propagation constant, which is determined by

$$\gamma = \sqrt{ZY} = \sqrt{(\tilde{R} + \imath\omega\tilde{L})(\tilde{G} + \imath\omega\tilde{C})}, \tag{3.5}$$

with α the attenuation constant and β the phase constant. The power transmitted is

$$P(x) = \mathrm{Re}\left[V(x)\overline{I(x)}\right] = P(0)e^{-2\alpha x}. \tag{3.6}$$

Note that the power attenuation is 2α. Relations for the group velocity $v_{gr} = \delta\omega/\delta\beta$ and phase velocity $v_{ph} = \omega/\beta$ can readily be found.

The lines' characteristic impedance Z_0 is given by V(x)/I(x):

$$Z_0 = \sqrt{\frac{Z}{Y}} = \sqrt{\frac{\left(\tilde{R} + \imath\omega\tilde{L}\right)}{\left(\tilde{G} + \imath\omega\tilde{C}\right)}}. \tag{3.7}$$

Physically, $\tilde{R}$ represents the resistance in the conductors, contributing to the loss in the stripline. $\tilde{R}$ is related to the surface impedance of the metal (see Ch. 4). $\tilde{G}$ represents losses in the dielectric. At the frequency of interest for this thesis, these losses are negligible. The series inductance $\tilde{L}$ includes the surface impedance of the conductors and the geometry of the line.

Using a simplified model, the influence of the line's geometry can be assessed. We consider a parallel-plate line as sketched in Fig. 3.5. Assuming the width w is much greater than the spacing h, fringing effects can be ignored. For a lossless conductor (i.e. $\tilde{R}$=0, an ideal metal), we find[24]

$$\tilde{L} = \mu_0 \frac{h}{w}, \tag{3.8}$$

and

$$\tilde{C} = \epsilon_0 \epsilon_r \frac{w}{h}. \tag{3.9}$$

Using Eqs. (3.7) and (3.5), we find:

$$Z_0 = \frac{\sqrt{\mu_0/\epsilon_0}}{\sqrt{\epsilon_r}}\frac{h}{w} = \frac{\eta_0}{\sqrt{\epsilon_r}}\frac{h}{w} \tag{3.10}$$

and

$$\gamma = \imath\omega\sqrt{\mu_0\epsilon_0}\sqrt{\epsilon_r} = \imath\frac{\omega}{c}\sqrt{\epsilon_r}, \tag{3.11}$$

where ϵ_r is the dielectric constant of the spacer layer. $\eta_0 = \sqrt{\mu_0/\epsilon_0} = 377\,\Omega$ is the vacuum impedance and $c = 1/\sqrt{\mu_0\epsilon_0}$ is the speed of light in vacuum, the phase velocity is given by $v_{ph} = \omega/\beta = c/\epsilon_r$.

Following Ref. 25, we now consider the same transmission line using normal metal conductors, i.e. $\tilde{R} > 0$. The surface resistance, $\mathrm{Re}(Z_s)$, now contributes to the impedance of the line. Its impedance Z is now given by $Z = \imath\omega\tilde{L} + 2Z_s/w$. Y remains the same. Assuming the system to be in the regime of the classical skin effect, Z_s is given by

$$Z_s = \frac{1}{\sigma\delta_c}(1+\imath), \tag{3.12}$$

where σ is the conductivity of the metal and $\delta_c = \sqrt{2/\mu_0\omega\sigma}$ is the classical skin depth. At 1 THz, $\delta_c \approx 35$ nm for the striplines typical for this work, while h is of the order of 400 nm. Therefore, we assume that $\delta_c \ll h$. In that regime, Z_0^{loss} and γ^{loss} can be approximated to first order in δ_c/h by:

$$Z_0^{loss} = \sqrt{Z/Y} \approx Z_0(1+\frac{\delta}{2h}) - \imath Z_0\frac{\delta}{2h} \tag{3.13}$$

and

$$\gamma^{loss} = \sqrt{ZY} \approx \frac{\omega}{c}\sqrt{\epsilon_r}\frac{\delta_c}{2h} + \imath\frac{\omega}{c}\sqrt{\epsilon_r}(1+\frac{\delta_c}{2h}). \tag{3.14}$$

Introducing resistive loss in the metal of the transmission line causes the real part of Z_0 to rise by $\delta_c/2h$ and the attenuation constant to increase from 0 to $(\omega/c)\sqrt{\epsilon_r(\delta_c/2h)}$. The phase velocity v_{ph} is reduced by about $\delta_c/2h$. The change in reactance mainly causes a frequency shift that can be corrected for. More serious is the increased loss caused by the surface resistance. This directly reduces the sensitivity of the mixer.

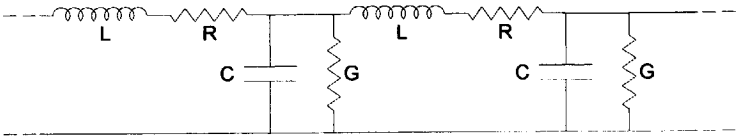

FIGURE 3.6. Equivalent circuit of a of microstrip line in ladder representation.

This Section gives some insight in the behavior of microstrip transmission lines. For the actual design of the devices produced in this thesis, a more realistic description of the surface resistance in these transmission lines is used[26]. However, the general behavior is well explained by these considerations.

The behavior of CPW lines will not be discussed here as details on the calculations can be found in literature[27–29]. In Chs. 4 and 6 we use this method and describe it in some detail.

3.6 Discussion

The methods to simulate the properties of microstrip lines described in this Chapter have been used extensively at frequencies up to ~ 1 THz. Experiments have shown that the simulations describe the direct reponse accurately. At higher frequency, neither experimental nor simulated results are available and the accuracy of the models is unknown. Especially, the surface resistance increases strongly with increasing frequency, requiring optimization of the microstrip line to design lowest-noise receivers.

References

[1] C.E. Honingh, *A quantum mixer at 350 GHz based on superconductor-insulator-superconductor (SIS) junctions*, Ph. D. thesis, Rijks*Universiteit* Groningen (1993).

[2] S.S. Gearhart and G.M. Rebeiz, IEEE Trans. on Microwave Theory Tech. **42**, 2504 (1994).

[3] B.S. Karasik, M.C. Gaidis, W.R. McGrath, B. Bumble and H.G. LeDuc, IEEE Trans. on Appl. Supercond. **7**, 3580 (1997).

[4] P. Goldsmith, *Quasioptical systems,* IEEE Press, Piscataway, NJ, ISBN 0-7803-3439-6 (1998).

[5] J. Zmuidzinas and H.G. LeDuc, IEEE Trans. Microwave Theory Tech. **40**, pp. 1797-1804 (1992).

[6] G. de Lange, *Quantum Limited Heterodyne Detection of 400-840 GHz Radiation with Superconducting Nb Tunnel Junctions*, Ph. D. thesis, Rijks*Universiteit* Groningen (1994).

[7] B.D. Jackson, A.M. Baryshev, G. de Lange, J.R. Gao, S.V. Shitov, N.N. Iosad and T.M. Klapwijk, Appl. Phys. Lett. **79**, 436 (2001).

[8] B. Ellison, M.L. Oldfield, D.N. Matheson, B.J. Maddison, C.M. Mann and A.F. Smith, Proc. 5th Int. Symp. Space THz Techn., Ann Arbor, MI, May 10-12, pp. 851-860 (1994).

[9] D.B. Rutledge and M.S. Muha, IEEE Trans. Antennas Propagat. **30**, 535-540 (1982).

[10] E. Gerecht, C.F. Musante, Y. Zhuang, M. Ji, K.S. Yngvesson, T. Goyette and J. Waldman, Proc. 11th Int. Symp. Space THz Techn., Ann Arbor, MI, May 1-3, pp. 209-218 (2000).

[11] P. Yagoubov, M. Kroug, H. Merkel, E. Kollberg, J. Schubert, H.-W. Hübers, S. Svechnikov, B. Voronov, G. Gol'tsman and Z. Wang, Proc. Europ. Conf. on Appl. Superconductivity (EUCAS'99), Barcelona, September 14-17 (1999).

[12] A.D. Semenov, H.W. Hübers, J. Schubert, G.N. Gol'tsman, A.I. Elantiev, B.M. Voronov, E.M. Gershenzon, Proc. 11th Int. Symp. Space THz Techn., Ann Arbor, MI, May 1-3, pp. 39-48 (2000).

[13] T. Büttgenbach, IEEE Trans. on Microwave Theory Tech. **41**, 1750-1761 (1993).

[14] D.F. Filipovic, S.S. Gearhart and G.M. Rebeiz, IEEE Trans. Microwave Theory Tech. **41**, pp. 1738-1749 (1993).

[15] D.F. Filipovic and G.M. Rebeiz, Int. J. IR and MM waves **14**, pp. 1905-1924 (1993).

[16] D. Kasilingam and D.B. Rutledge, Int. J. IR and MM waves **7**, pp. 1631-1647 (1986).

[17] C.A. Balanis, *Antenna Theory,* 2nd ed., Whiley & Sons, NY, ISBN 0-471-59268-4 (1997).

[18] A.D. Semenov, Yu. P. Gousev, R.S. Nebosis, K.F. Renk, P. Yagoubov, B.M. Voronov, G.N. Gol'tsman, V.D. Syomash and E.M. Gershenzon, Appl. Phys. Lett. **69**, 260 (1996).

[19] A. Skalare, W.R. McGrath, B. Bumble, H.G. LeDuc, P.J. Burke, A.A. Verheijen, R.J. Schoelkopf and D.E. Prober, Appl. Phys. Lett. **68**, 1558 (1996).

[20] R.A. Wyss, A. Neto, W.R. McGrath, B. Bumble and H.G. LeDuc, Proc. 11^{th} Int. Symp. Space THz Techn., Ann Arbor, MI, May 1-3, pp. 379-388 (2000).

[21] H. v.d. Stadt, A. Baryshev, P. Dieleman, T.M. Klapwijk, S. Kovtonyuk, G. de Lange, I. Lapitskaya, J. Mees, R. Panhuyzen, G. Prokopenko and H. Schaeffer, Proc. 6^{th} Int. Symp. Space THz Techn., Pasadena, CA, March 21-23, pp. 66-77 (1995).

[22] A. Karpov, D. Miller, F. Rice, J. Zmuidzinas, J.A. Stern, B. Bumble, H.G. LeDuc, Proceedings of the 8^{th} International Superconducting Electronics Conf., Osaka, Japan, June 19-22, pp. 521-522 (2001).

[23] D.M. Pozar, *Microwave Engineering*, Addison-Wesley, Reading MA, (1990).

[24] J.D. Jackson, *Classical Electrodynamics*, (Wiley, New York NY, 1975).

[25] M. Bin, *Low-noise THz Niobium SIS Mixers*, Ph. D. thesis, California Institute of Technology, Pasadena, CA (1997).

[26] R.L. Kautz, J. Res. of the Nat'l. Bureau Std. **84**, no. 3, 247 (1979).

[27] B.C. Wadell, *Transmission Line Design Handbook*, Artech House, Inc., ISBN 0-89006-436-9 (1991).

[28] R. v.d. Laan, M. Sc. thesis, nr. 439/97/Afst/FDL, Rijks*Universiteit* Groningen (1997).

[29] W.F.M. Ganzevles, J.R. Gao, D. Wilms Floet, G. de Lange, A.K. van Langen, L.R. Swart, T.M. Klapwijk and P.A.J. de Korte, Proc. 10^{th} Int. Symp. Space THz Techn., Charlottesville VA, March 16-18, pp. 247-260 (1999).

[30] G. Yassin and S. Withington, J. of Phys. D **28**, 1983 (1995), and G. Yassin and S. Withington, ESA Technical Report RDG 4 (1995) (unpublished).

[31] M. Kominami, D.M. Pozar and D.H. Schaubert, IEEE Trans. on Antennas and Propagat. **33**, 600 (1985).

Chapter 4

Lay-out and design of quasi-optically coupled hot electron bolometer mixers

4.1 Introduction

The sensitivity of a mixer is determined by its conversion gain, intrinsic noise and coupling efficiency of the signal from free space to the Nb bridge. In this Chapter, we focus on the last contribution. In designing the rf geometry, it is important to understand the parameters dominating the direct response and to be able to design an efficient rf coupling environment.

Until recently, quasi-optical (QO) HEBMs have been based on co-planar waveguide (CPW) transmission lines. The direct response of this type of device has not been looked at in detail before[1]. Therefore, we develop a model to simulate the direct response of these devices.

A novel rf coupling circuit is designed to efficiently connect the twin-slot antenna to the nanobridge in quasi-optical HEBM-receivers. This design uses a microstrip line transmission line instead of a CPW-line. This transmission line consists of the gold antenna groundplane, a SiO_2 dielectric layer and an Al top wiring. A model is developed to calculate the direct response of these devices.

In this Chapter, we first outline general methods to simulate the direct response of quasi-optical HEBMs. Second, we sketch the structure of these devices. Third, we describe the simulation of the direct response of CPW-

based HEBMs, followed by the simulation of microstrip line coupled HEBMs. The Chapter ends with a discussion and conclusions.

4.2 Method to simulate the direct response of HEBMs

We have simulated the coupling efficiency of the antenna–transmission line–nanobridge–filter-combination as a function of frequency. This is done in two ways. In one approach, we consider the structure as a whole and calculate the current– and voltage distribution and from there the impedance seen by the bridge. For this method, we use a commercially available software package[2]. We take into account the devices' geometry and surface impedance using the dc conductivity of the metal σ_{dc}. We note that this method has only been used for the CPW-coupled devices.

In the other approach, we simulate all elements separately, link them together (e.g. using the ABCD-formalism, see, for example, Ref. 3) and optimize each element for maximum coupling. The elements we take into account are the antenna, the transmission line transformer, the choke filter and the nanobridge itself. These elements are easily identified in Fig. 4.1 and 4.2. In this simulation, we take into account geometry, the surface impedance of the metals and the effect of fringing fields.

For both types of transmission line, models to calculate their characteristic impedance Z_0 are available. However, due to a lack of expressions to obtain the loss in CPW lines, only reflection losses are taken into account. In the microstrip line model, losses are better described. Ohmic losses are estimated using the surface resistance $\mathrm{Re}(Z_s)$ according to Ref. 4. Reflection losses are taken into account as well.

4.2.1 Outline of the rf structure using twin-slot antenna coupled HEBMs

The devices we simulate here all contain a twin-slot antenna, an impedance transformer, a filter and a nanobridge. The antenna is a twin-slot antenna: a metal ground plane containing two long, narrow slots. To transport the radiation from the antenna slots to the nanobridge, a transformer is used.

A so-called rf choke filter is used to avoid the rf signal to leak away from the nanobridge. This filter is built in the same technology as the transformer.

The last element of the HEBM that is taken into the calculation is the mixing element itself.

4.3 Microstrip line coupled HEBMs

We start by describing the rf circuit used in microstrip-line coupled HEBMs. The rf structure has to be coupled efficiently to the mixing element. This has an estimated impedance of about $15 - 50\,\Omega$. Antennas that have been used in practical receivers have an impedance at center frequency around $30 - 40 + 5i\,\Omega$. These values provide us with a realistic basis to start with.

In this geometry, we use an antenna with $l = 0.33\lambda_0$, separation $s = 0.17\lambda_0$, in which λ_0 is the free space-wavelenght, and width $w = 0.05 \cdot l$, which is situated in the groundplane. The SiO_2 dielectric (400 nm thick) separates the antenna plane from the top wiring (150 nm Al). The signal is picked up from the ground plane to the top wiring by rectangular or radial stubs (capacitors) acting as shorts for rf radiation. Via a microstrip line transformer, the signal is fed to the Nb bridge which is also located on the top wiring. An rf choke filter prevents the signal from leaking into the IF chain.

The microstrip line-coupled HEBM can be seen as a 3-dimensional structure in which the electric field is perpendicular to the substrate, running in a dielectric between the ground plane and the top wiring, whereas in the CPW-coupled HEBM, the field is parallel to the substrate between two conductors (see Fig. 4.1).

The (dis)advantages of microstrip line– and CPW-technology are discussed in Chs. 3 and 7.

A $\frac{1}{4}\lambda_{\text{eff}}$ rf filter is used to prevent signal from entering the IF chain. λ_{eff} is the effective wavelength in the dielectric (microstrip line) or at the Si–air boundary (CPW devices). The filter consists of high impedance sections with a width of 1.5 μm and low impedance sections having a width of 8 μm. At 2.5 THz, the length of the sections is 12 μm. A CPW transmission line, optimized at IF, is connected to the filter. This acts as the connection to both the DC bias supply and the IF amplifier. A similar design is reported in literature at various frequencies[1,8].

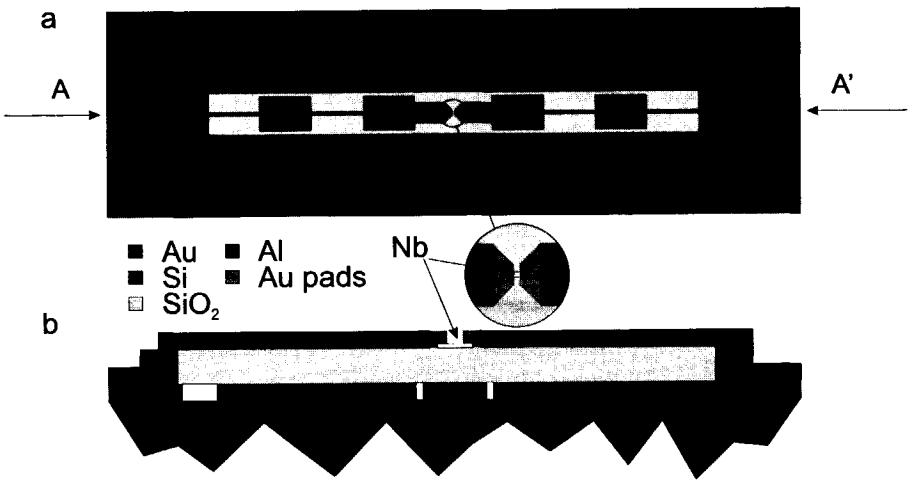

FIGURE 4.1. [a] Lay out of a microstrip line coupled HEBM. The two vertical lines form the twin slot antenna. The transformer runs from either slot to the nanobridge. The choke filter is built in the same type of transmission line, extending outwards from the slots. [b] Cross section of this device along the line A-A'. The typical slot length l equals 39.6 μm, separation s = 20.4 μm and width w = 2.0 μm.

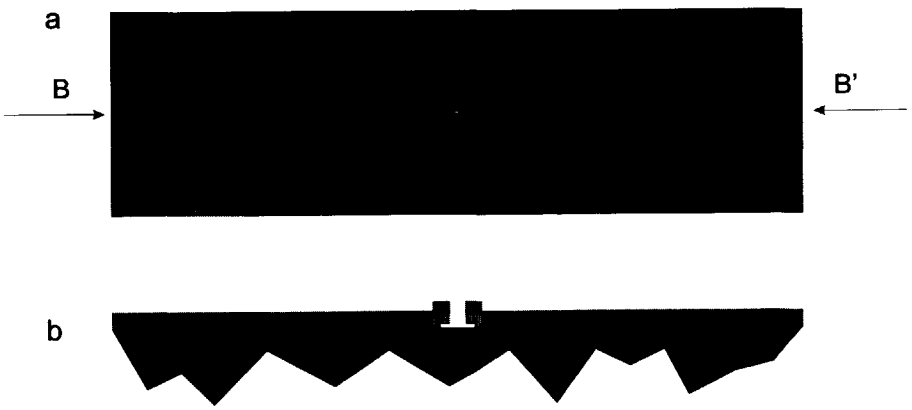

FIGURE 4.2. [a] Lay out of a CPW line coupled HEBM. In this case, the transformer and choke filter are built in CPW transmission line. The superconducting bridge itself is located in between the two transformers. The antenna dimensions are similar to those in the microstrip line. [b] Cross section along the line B-B'.

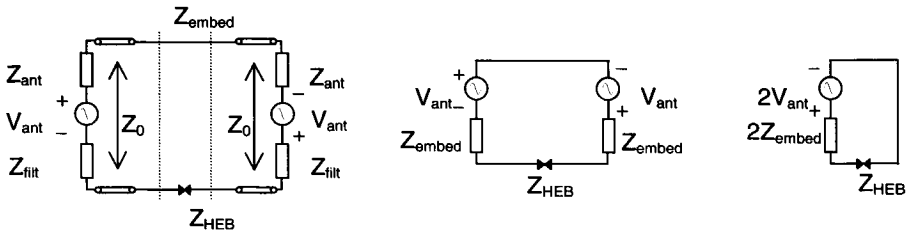

FIGURE 4.3. The rf structure represented in terms of voltage generators and impedances. Simplifying them correctly, one arrives at the rightmost scheme. V_{ant} and Z_{ant} are the voltage and impedance generated by the antenna, respectively. Z_{filt} is the impedance of the filter, Z_{HEB} is the normal state resistance of the HEBM (see Ch. 6). The characteristic impedance of the transmission line is represented by Z_0, while Z_{embed} represents the equivalent impedance originating from one side of the filter and antenna after being transformed by the transmission line.

4.4 CPW-coupled HEBMs

The most transparent way to calculate the coupling of radiation into the device is to describe the circuit in terms of separate impedances, calculate each impedance separately and transform them to the effective impedance seen by the bridge and calculate the coupling between the bridge and the environment η_{int} using:

$$\eta_{int} = 1 - \left| \frac{Z_{HEB} - 2\,Z_{embed}}{Z_{HEB} + 2\,Z_{embed}} \right|^2, \tag{4.1}$$

where Z_{HEB} is the impedance of the nanobridge and Z_{embed} the impedance of the environment at the position of the HEB. It should be noted that Eq. 4.1 only takes into account reflection losses. Ohmic losses cannot be calculated in this way.

An equivalent circuit of our device, following a model by Gearhart and Rebeiz[8], is shown in Fig. 4.3. When the circuit is fed in phase, it can be simplified by transforming the added antenna– and filter impedance (Z_{ant} and Z_{filter}, respectively) via the characteristic microstrip line impedance Z_0 into Z_{embed}. Now, the coupling between the two impedances can be calculated using Eq. (4.1). By tuning the geometry of the antenna and transformer

lines, the coupling is optimized. The calculation and optimization of the constituent parts are described in the sections below.

Twin slot antenna

The antenna properties are calculated using a program by Chattopadhyay and Zmuidzinas[9], which is based on a model by Kominami *et al.*[10]. The program takes into account antenna geometry and ϵ_r of the substrate, but metal thickness and resistive loss of the antenna are not taken into account. It calculates, among others, the antenna input impedance and its beam pattern.

The efficiency of the antenna is good at f_c and below, but drops rapidly above f_c. This is due to 2 principal effects: first, the antenna develops grating lobes in the $\vec{E}$-plane due to the slot spacing exceeding $\lambda_{dielectric}/2$; second, the slots start to behave as traveling-wave antennas rather than standing wave antennas at higher frequencies, which tends to produce a V-type double-lobe pattern in the $\vec{H}$-plane rather than a single lobe pattern. The overall result is that the main beam splits into multiple lobes. To account for the decreased efficiency above f_c in the model, the coupling is multiplied by the relative power coupled into the main lobe as a function of frequency[9]. This is a rapidly dropping function of frequency.

Several double slot antenna geometries are suggested in literature[5,8,12], which in general vary around a length of $l = 0.33 \cdot \lambda_0$, where λ_0 is the wavelength in free space, a separation of $s = 0.17 \cdot \lambda_0$ and a slot width w of $0.05 \cdot l$. Fig. 4.4 shows the impedance vs frequency for the antenna we use in our design. The reactance at f_c is low, which allows good power transfer into the microbridge without having to tune out any antenna reactance. Although the impedance changes with frequency, the response is fairly flat. Matching should not be influenced too much over the device bandwidth (~ 1.5 THz). At the center frequency, the beam pattern of this antenna is fairly symmetric: θ^E/θ^H, the ratio of the $\vec{E}$- and $\vec{H}$-plane beam width at half-max, equals 1.08 and the main beam efficiency is calculated to be 91%. Less than 9% is coupled into the back lobe and only 1% is lost into dielectric sidelobes. These values are calculated for the geometry mentioned above, but are typical for the antennas we calculated.

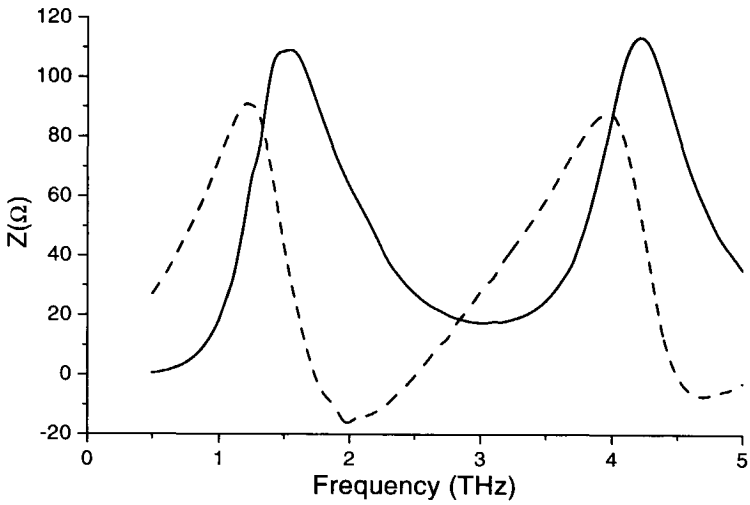

FIGURE 4.4. $\mathrm{Re}(Z_{ant})$ (solid line) and $\mathrm{Im}(Z_{ant})$ (dashed line) at the feed point of a twin slot antenna having a geometry of $l = 0.33 \cdot \lambda_0$, a separation of $s = 0.17 \cdot \lambda_0$ and a slot width w of $0.05 \cdot l$, where λ_0 is the wavelength in free space.

The transformer

To match the antenna impedance to the bridge impedance, a CPW transformer is used. Its function is to transform the antenna impedance into an effective impedance seen by the bridge. The transformer is a piece of CPW transmission line. Ideally, for a $\lambda/4$-transformer, its impedance is equal to the geometric mean of the antenna– and bridge impedance: $Z_{CPW} = \sqrt{Z_{HEB} \cdot Z_{ant}}$. This would require a CPW with narrow slots (few hundreds of nm), which is difficult to make in practice. It is possible to reliably fabricate a CPW with slots about 500 nm wide.

A 'standard' CPW with $a = 0.5\,\mu m$ and $b = 2.0\,\mu m$ has a characteristic impedance of about $39\,\Omega$ as calculated by Momentum, while a similar value has been obtained using Touchstone[13]. Calculations performed using an expression based on elliptical integrals (e.g. Wadell[14]) give $18\,\Omega$. The disagreement increases with decreasing slot width. Unfortunately, Momentum-calculations are lengthy. Therefore, we assume that Z_0 for the standard

TABLE 4.1. Characteristic impedance of certain CPW lines.

	a(μm)	b(μm)	$Z_{0,Mom}(\Omega)$	$Z_{0,ell.\,int}(\Omega)$
$Z_{transf.}$	0.5	2	39	18
Z_{low}	1	7	—	26
Z_{high}	4	1	—	75

CPW as calculated by Momentum can be linearly interpolated using the values obtained via Ref. 14, at least over a small enough range in slot width.

The rf choke filter

The rf filter we use is designed such that it reflects the rf signal back to the microbridge. This avoids signal being lost into the IF chain. It is important to note that the filter has low impedance. If this were not the case, the antenna impedance would be strongly influenced, as an infinite metal groundplane is assumed around the slots, acting as a short. The filters are designed to have a small number (typically 2×2) of $\lambda/4$-sections to keep the series resistance as low as possible. Although a low number of filter sections decreases the steepness at the cut-off frequencies, the impedance around f_c is not affected. The filter is made in the same transmission line technology as the transformer and since the slot widths are rather large, calculations are done using Ref. 14.

The Nb nanobridge

The impedance of the nanobridge can be described by $Z_{HEB} = Z_S \cdot \frac{L}{d} + Z_L$, with L the bridge length, d its thickness and Z_L its geometric inductance. Z_S reduces to the square resistance $R_\square$ when the frequency is higher than the gap frequency of the bridge and the film thickness is much smaller than the skin depth[15]. Furthermore, Z_L is small, on the order of $2i\,\Omega$ for our device[16]. Therefore, Z_{HEB} in practice equals the normal state resistance R_N. The geometric inductance may in practice be larger than estimated due to

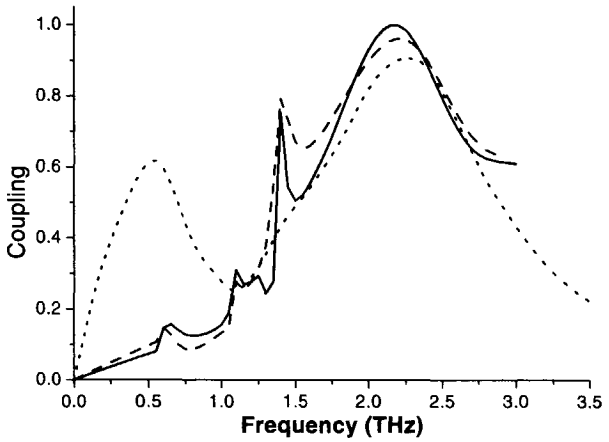

FIGURE 4.5. Comparison between the intrinsic coupling η_{int} calculated using a Method of Moment (MoM) approach (solid line: infinite gold conductivity σ, dashed line: $\sigma = 1 \cdot 10^7\ \Omega^{-1}\mathrm{m}^{-1}$) and a calculation based on the equivalent circuit method (dotted line). All curves assume on an $Z_{HEB} = 40\,\Omega$ and a geometry described in Table 4.2.

a rather sharp squeezing of the current from the CPW's center conductor to the nanobridge as has been suggested by Wyss *et al.*[17].

4.4.1 Results of the equivalent circuit-approach for CPW devices

A 2.5 THz CPW mixer has been designed using the above design scheme. To do this, we have chosen the parameters given in Table 4.2.

The simulated intrinsic coupling η_{int} (i.e. the relative power transfer from just in front of the antenna to the nanobridge) as a function of frequency is given by the dotted line in Fig. 4.5. The main response centers at $f_c = 2.2$ THz and has a bandwidth B equal to 1.3 THz. The maximum response is 82%. Since no Ohmic loss is taken into account, this means that some 18% of the signal is lost due to reflections in the structure. The low-frequency resonance is found to be due to the filter.

Bearing in mind Fig. 4.4, a peak in efficiency is expected at the second

resonance of the antenna, about 4.5 THz. However, due to the decrease in antenna efficiency with frequencies described above, this resonance does not show up.

As a function of Z_{HEB}, an optimum in coupling is found at 45 Ω, keeping Z_{CPW} fixed at 41 Ω. This maximum changes 20% over the range 20-80 Ω. The center frequency is constant. Assuming $R_N = 40\,\Omega$, the characteristic impedance of the line is changed from 15 to 45 Ω. This causes the coupling to rise sharply from 0.70 to 0.90. Thereafter, it slowly drops back to 0.85 at 75 Ω. Doing this, f_c rises from 2.25 to 2.45 THz.

4.4.2 Method of Moments-calculation of the intrinsic CPW coupling

Another approach to calculate the properties of the structure is the so-called Method of Moments (MoM). This method takes into account the geometry and material properties of the detector to calculate the current– and voltage distribution in the layers. From there, the $\vec{E}$– and $\vec{H}$-field can be calculated, as well as the impedance at any point, the beam pattern and the time-dependence of the fields. We use Hewlett Packards' HPADS (HP Advanced Design System[2] (also known as Momentum)) software to perform this task. The impedance at the position of the superconducting bridge is determined as a function of frequency. Using an equation very much like Eq. (4.1), it is then coupled to Z_{HEB} to find the coupling efficiency. Note that this approach does not allow us to calculate the Ohmic loss in the metals.

The termination at the IF side of the filter does not influence the calculation much, presumably because it is far away from the antenna (note that, for an ideal filter, no influence is expected at all!). Therefore, the filter is left open in all calculations. At the position of the microbridge, a small ($\sim 1\ \mu$m) slot is assumed, keeping both CPW signal lines unconnected. A port all impedances are referred to has been defined by asuming a very small ($\sim 1\ \mu$m) microstrip line patch at the position of the nanobridge, its top wiring serving as the input port. It is checked that this microstrip line/via combination has little or no effect on the simulated device characteristics. Eq. (4.1) is used to couple the nanobridge's impedance Z_{HEB} to this port and to calculate the direct response.

For simplicity, the conductivity of the Au groundplane is assumed to

TABLE 4.2. Geometry of the CPW-device used for the simulations in CPW-coupled HEBMs.

Antenna	l = 38.4 μm, s = 19.2 μm, w = 1.9 μm
Transformer	length = 2 × 8.5 μm, a = 0.5 μm, b = 2.0 μm
Filter: low imp.	length = 11.9 μm, a = 1.0 μm, b = 7.0 μm
Filter: high imp.	length = 11.9 μm, a = 4.0 μm, b = 1.0 μm
Nanobridge	length=250 nm, width=150 nm, R_N = 40 Ω
Substrate	Si, 300 μm, ϵ_r = 11.7, metal thickness: 200 nm.

be infinite and the impedance of the HEB is taken to be 40 Ω, equal to its normal state resistance R_N (see Ch. 6).

Results of the MoM-approach applied to CPW-coupled HEBMs

To calculate the coupling of a typical design at 2.5 THz, we calculate the impedance at the position of the nanobridge for the structure described in Table 4.2. Z_{embed} found at the position of the Nb bridge is then coupled to R_N using Eq. (4.1) over the frequency range of interest, yielding the intrinsic coupling efficiency η_{int}, as shown in Fig. 4.5 (solid line). η_{int} peaks at a center frequency f_c around 2.2 THz, close to the design frequency, and its 3 dB bandwidth B equals 1.4 THz. A series of peaks is observed at 0.6, 1.1 and 1.4 THz. These are due to resonances occurring in the rf choke filter: when the filter is not present in the calculations, the resonances disappear.

To assess the influence of the groundplane conductivity σ_{Au}, we decrease σ_{Au} from ∞ to a practical value of $1 \cdot 10^7\ \Omega^{-1}m^{-1}$ (dashed line). This causes the maximum of η_{int} to be broader (B = 1.9 THz) and 5% lower. The filter resonances are less sharp, too. These effects are expected when one thinks of the system as a resonant circuit with its Q-factor being decreased. Upon lowering σ_{Au} even more, the broadening gets less and less pronounced.

The geometry of the CPW transformer is of influence to the center frequency as well. It is found that a characteristic impedance $Z_{0,CPW}$ close to

40 Ω yields an f_c closest to the design frequency (2.5 THz).

Comparing the MoM-results to those obtained from the distributed-element approach, good agreement is observed. The peak frequency and bandwidth in both are similar. The MoM-approach gives some more details (e.g. the filter resonances). This is because the MoM-approach takes into account the interdependence of the different features in the device, whereas the distributed-element approach only takes into account the impedance of each element.

4.5 Microstrip line-coupled HEBMs

In this Section, the simulation of the coupling in the second type of devices, microstrip line coupled HEBMs, is described. In this simulation, we use the same equivalent circuit-approach as described above. For microstrip line calculations, adequate models are available to estimate the loss in the metals at sub-THz frequencies, e.g. see Ref. 19. We will use the same models here.

4.5.1 The influence of surface impedance at high frequency

In order to obtain the loss, it is important to have information on the surface impedance Z_s of the metals used. The characteristic impedance of microstrip lines is determined by, aside from the lines' geometry, the surface impedance of the metals. A significant part of the loss in high-sensitivity detectors is due to the surface resistance $R_s = \mathrm{Re}\,(Z_s)$, since this determines the Ohmic loss in the transmission line.

In general, Z_s is given by

$$Z_s(\omega) = \frac{E_x(0,\omega)}{\int_0^\infty J_x(z,\omega)dz} = R_s + iX_s \tag{4.2}$$

where $J_x(z,\omega)$ is the current density at a depth z in the conductor and $E_x(0,\omega)$ is the electric field at the conductors' surface, parallel to the current. Z_s consists of the surface resistance R_s and the surface reactance X_s.

With respect to Z_s, we differentiate between three frequency regimes:

1. In the low-frequency limit, when the electron mean free path l_e is the smallest dimension in the system at hand, the system is in the local

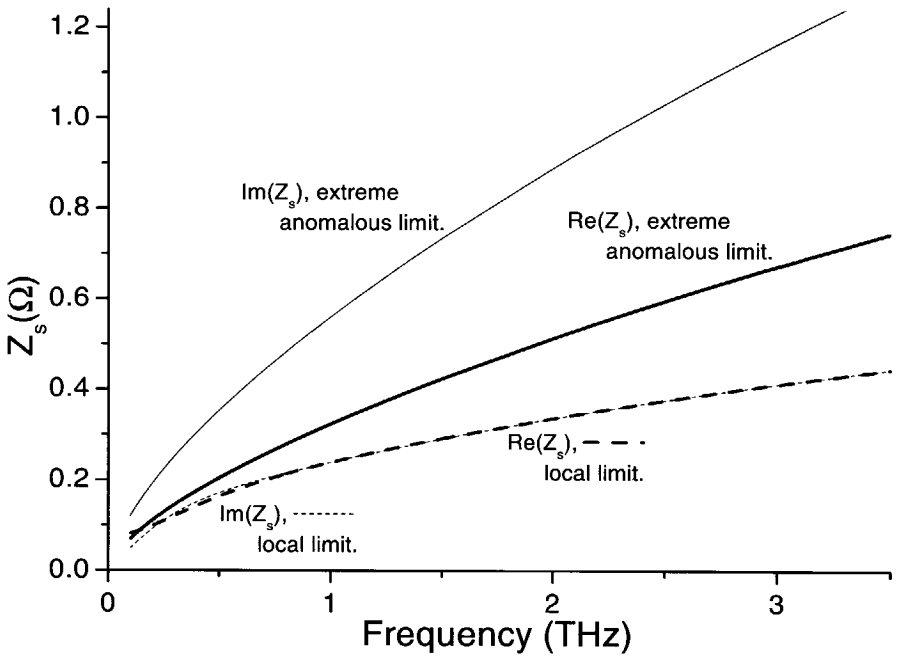

FIGURE 4.6. The surface impedance Z_s of Al as a function of frequency for 190 nm thick Al. We assume that $\sigma_{dc} = 0.7 \cdot 10^8\ \Omega^{-}\mathrm{m}^{-1}$, RRR=3, $l_e = 28$ nm, $\delta_c = 38$ nm at 2.5 THz. These values are typical for the films we produce. The thin solid line represents $\mathrm{Im}(Z_s)$, the thick solid line represents $\mathrm{Re}(Z_s)$, both in the extreme anomalous limit. The thin and thick dashed line represent $\mathrm{Im}(Z_s)$ and $\mathrm{Re}(Z_s)$, respectively, in the local limit. Au shows a similar behavior. It is noteworthy that in the local limit, Au is the better choice due to its higher dc conductivity ($\sigma_{dc} = 1.6 \cdot 10^8 \Omega^{-1}\mathrm{m}^{-1}$), whereas in the extreme anomalous limit Al a lower R_s, since it has a higher Fermi-velocity: $v_{F,Al} = 2.02 \cdot 10^4\ \mathrm{ms}^{-1}$ vs $v_{F,Au} = 1.39 \cdot 10^4\ \mathrm{ms}^{-1}$ [20].

limit. In terms of rf radiation penetrating the metal, this means that within one oscillation the electrons are scattered many times.

The current density and electric field are related via $\mathbf{J} = \sigma\mathbf{E}$. Together with Maxwell's equations, this yields for for the surface impedance

$$Z_s = \sqrt{\frac{i\omega\mu_0}{\sigma_{dc}}} \coth\left(\sqrt{i\omega\mu_0\sigma_{dc}}d\right), \tag{4.3}$$

where ω is radiation frequency, σ_{dc} the dc conductivity, d the metal layer thickness and μ_0 the vacuum permittivity. For normal metals, like Au and Al, σ_{dc} is a real (i.e. not complex) constant. For superconductors, σ is complex and frequency dependent (see, e.g., Mattis and Bardeen[21]).

2. The length over which the field penetrating the metal decays is the classical skin depth $\delta_c = \sqrt{\frac{2}{\omega\mu_0\sigma}}$. When δ_c becomes of the order of l_e, the local limit no longer holds: the system is in the anomalous limit. The distance the electron travels in the metal in one oscillation is now comparable to the electron mean free path. The simple relation between **J** and **E** has to be replaced by its non-local equivalent (see Pippard[22]). In this regime, calculations of the surface impedance are complicated since no analytical expressions are available, but numerical routines to obtain solutions are available[23].

3. The extreme anomalous limit is reached at high frequency, when $l_e \ll \delta_c$. The Reuter and Sondheimer-solution[24] for this regime is given by

$$Z_s = \frac{1+\sqrt{3}i}{3^{1/2}\pi^{1/3}} \frac{\sqrt[3]{\left(\frac{3}{2}\frac{l_e^2}{\delta_c^2}\right)^2}}{\sigma_{dc} l_e} = \frac{1+\sqrt{3}i}{3^{1/2}\pi^{1/3}} \sqrt[3]{\frac{9\omega^2\mu_0^2 m_e}{16e^2 n_e}}, \qquad (4.4)$$

where μ_0 is the vacuum permittivity, e and n_e are the electron charge and density, respectively, and m_e is the free electron mass. The last step is obtained using the Drude-model. It is noteworthy that in this regime, the surface impedance is independent of σ_{dc}. Only the material parameter n_e plays a role.

For the Al we typically produce, $l_e/\delta_c = 0.7$ at 2.5 THz, for the Au we find $l_e/\delta_c = 5$. These values put us somewhere between the anomalous and extreme anomalous limit. Z_s for the extreme anomalous limit is calculated using Eq. (4.4). For the anomalous limit, we use a computer code by Bin *et al.*[23] based on the method described by Kautz[4].

Instead of the CPW transmission line, it is also possible to employ a microstrip line for the transformer and rf choke filter. Fig. 4.1 illustrates the microstrip line considered in this simulation. The microstrip line ground

plane, in which the antenna is defined, is an Al layer with a thickness of 150 nm. The top wiring is an Al layer of the same thickness. The dielectric layer is made of 400 nm SiO_2 with $\epsilon_r = 3.8$.

To simulate the direct response for this type of structures, only the method using equivalent circuits has been used. The flexibility of this method shows here: only the impedance of the rf choke filter and transformer need to be recalculated, since the antenna– and nanobridge impedance can be taken directly from the CPW-calculations. In contrast to CPW lines, for microstrip lines used at very high frequency (up to 1 THz) the losses are reasonably well modeled. We simulate the attenuation in the metals by calculating the surface impedance Z_s, which contains the surface resistance. Once the impedance of all separate elements is known, they are linked using the so-called ABCD formalism (see, e.g., Pozar[3]). Contrary to Eq. (4.1), this *does* take into account the Ohmic losses in the metal planes.

Z_s is calculated in the anomalous limit indicated above using a numerical approach[23]. A comparison of the results obtained in the local and anomalous limit shows a very similar frequency dependence. The magnitude of Z_s in the anomalous limit is a factor 1.5 higher than in the local limit. Therefore, in the calculations we use the results obtained in the local limit multiplied by 1.5. In these calculations, experimentally observed parameters are used. We believe the difference is relatively small because the length of the microstrip line between the bolometer and the antenna is relatively short and the system is low-Q. As expected, it is found that the thickness of metal layers does not matter too much as long as the layers are thicker than a few times the skin depth δ_c. Changing the bridge's normal resistance has some influence on the total coupling: both f_c and the coupling efficiency are reduced when R_N is changed from 50 Ω to 25 Ω. In practice, this requires reproducibility in mixer fabrication, especially the bridge definition. The rf filter containing narrow Al lines with a width of 1 μm is hard to control in the fabrication. However, the simulations show that the deviation of the line width does not influence the coupling noticeably. On the other hand, the filter characteristic can be affected: the ratio of Z_{high}/Z_{low} is decreased. Table 4.3 shows an overview of results obtained in simulation of systems with different parameters.

Based on models generally used for microstrip line characterization (see e.g. Refs. 3 and 19), we now calculate the impedance of the microstrip line. The characteristic impedance of the line is calculated as a function of

frequency, including an effective ϵ_r and fringing field effect. The microstrip line impedance is calculated as a function of line width and thickness of metal and dielectric layers. By varying these parameters, the impedance can be tuned from about 8 Ω to 40 Ω without introducing orthogonal modes, i.e. without making the line wider than $\sim \lambda/4$. The ratio of characteristic impedance values obtainable in the microstrip line is much larger than that reported for low loss CPW lines, offering more freedom in transformer and filter design. In the calculations, microstrip line losses are found to be on the order of 2–3 dB per wavelength.

Transformers and RF choke filter

The impedance of the transformers and separate $\lambda/4$ filter sections is calculated using microstrip line formulæ[3]. The impedance Z_{in} of a microstrip line filter with characteristic impedance Z_0, length l and terminated with a load Z_{load}, then, is given by repeated application of

$$Z_{in} = Z_0 \cdot \frac{Z_{load} + iZ_0 \tan(\gamma \cdot l)}{Z_0 + iZ_{load} \tan(\gamma \cdot l)} \tag{4.5}$$

with γ the propagation constant.

Because the filter and the IF line are made of Al, their total dc resistance is not negligible. To reduce IF losses in these parts, we add a superconducting Nb layer on the top of Al.

4.5.2 Results of the equivalent circuit approach for microstrip line devices

To design a microstrip device suitable for use at 2.5 THz, we simulate the direct response of a device with the geometry present in Table 4.4.

The total filter assumed for the simulation in Fig. 4.7 has an impedance of $0.5 - 0.02i\ \Omega$ (at f_{center}). The filter bandwidth is at least as large as the antenna bandwidth, so that the total bandwidth of the mixer is determined by the antenna. Fig. 4.7 shows a plot of the total coupling efficiency vs frequency for several geometries. It can be seen that the maximum microstrip circuit coupling is about 87% and is located at 2.6 THz. The plot shows a

TABLE 4.3. For all calculations the following values are assumed unless otherwise stated: $\sigma_{Al,dc} = 1 \cdot 10^8\,\Omega^{-1}m^{-1}$, $t_{metal} = 150\,nm$, $t_{SiO_2} = 400\,nm$, $\epsilon_{r,\,SiO_2} = 3.8$, Z_{low}, Z_{high} and Z_{tfr} are the characteristic impedance of a low, high or transformer section, respectively.

	l (μm)	w (μm)	Z_0 (Ω)	α (dB/wavel.)	Remarks
Z_{low}	14.9	10	7.4-0.3i	1.8	
Z_{high}	16.5	1	43.5-2.1i	1.8	
Z_{tfr}	6	5	13.5-0.4i	1.8	
Z_{low}	13.9	10	4.1-0.2i	3.3	200nm SiO_2
Z_{high}	15.1	1	28.3-1.6i	3.1	200nm SiO_2
Z_{tfr}	6	5	7.7-0.5i	3.2	200nm SiO_2
Z_{low}	15.0	8	8.0-0.3i	1.8	smaller line
Z_{high}	15.9	2	27.8-0.9i	1.8	wider line

3 dB bandwidth of about 1.4 THz. The peak response shifts to higher frequencies when a smaller antenna is used and the coupling is slightly reduced as well. Dramatic reduction of coupling is found when the dielectric thickness is reduced. Calculating the coupling with and without filter yields a filter loss of $\sim 5\%$. It is also found that the number of sections is of negligible

TABLE 4.4. Geometry of the CPW-device used for the simulations in this Chapter.

Antenna	l = 39.6 μm, w = 20.4 μm, 2.0 μm
Transformer	length = 2 × 6.0 μm, widthb = 0.5 μm, a = 1.0 μm
Filter: low imp.	length = 14.9 μm, widthb = 10.0 μm, a = 1.0 μm
Filter: high imp.	length = 15.1 μm, widthb = 1.0 μm, a = 5.0 μm
Nanobridge	length=200 nm, width=200 nm, $R_N = 20\,\Omega$
Substrate	Si, 300 μm, $\epsilon_r = 11.7$, metal thickness: 150 nm, SiO_2-thickness = 400 nm, $\epsilon_{SiO_2} = 3.8$.

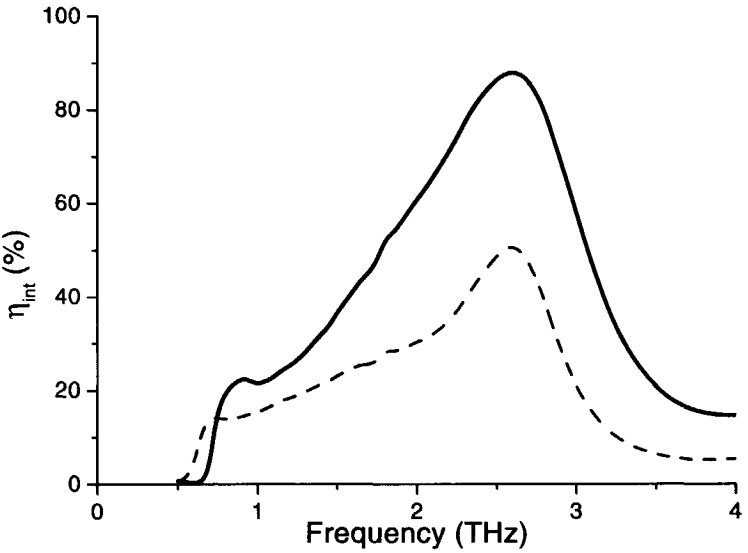

FIGURE 4.7. The simulated intrinsic coupling η_{int} to the device as a function of frequency. The thick solid line represents η_{int} in the anomalous limit. This curve overlaps that in the local limit (not shown). The dashed line shows η_{int} for a device with only 200 nm SiO_2.

influence.

4.6 Discussion

The simulations performed in this Chapter are used to design the HEBMs to be made in practice. No such detailed calculations in the THz range have been found in literature, neither for CPW–, nor for microstrip line structures. Therefore, a comparison to other simulations is not possible. We compare our results directly to the experimentally observed data. For the CPW-based devices, such a comparison will be made in Ch. 6. In Ch. 7, a similar comparison is made for the microstrip line devices.

Compared to CPW line devices, we believe the radiation loss of microstrip line devices is lower due to the fact that less 'sharp' transitions are

present in the ground plane. The antenna properties are less influenced by features in the ground plane, yielding a less disturbed beam pattern of the antenna. Since all dimensions of rf structure (not including the nanobridge) are larger than 1 μm, conventional lithography can be used. However, the structure is 3-dimensional, giving rise to several step coverages to be made (see Ch. 5).

In CPW devices, since the $\vec{E}$-field is parallel to the substrate, the metal plane can be considered effectively thick. This reduces the Ohmic loss in the transmission line. Furthermore, since CPW-technology can be considered 2-dimensional, fabrication could be simpler, although high-resolution pattern definition techniques (e.g. deep UV– or e-beam lithography) are required.

Some effects that we have neglected in the simulations may play an important role in the response of the detector. It is not clear, for example, how accurate it is to assume that $Z_{HEB} = R_N$. It has been argued[17] that the squeezing of the current from either center line of the CPW or the top wiring in the microstrip line device to the nanobridge causes an extra inductance, in turn causing a shift in f_c. This effect is modeled in both types of devices. For the CPW devices, we calculate the impedance of the nanobridge by feeding its geometry (downscaled to 2.5 GHz) in Momentum. We find an impedance of $100 + 46i\,\Omega$. This effect is much larger than the reactance of $\sim 2i\,\Omega$ obtained when the bridge is assumed to be a thin wire[16]. Another effect that is not taken into account in the CPW-simulations is the thickness of the metal layers. As will be argued in Ch. 6, this could also shift f_c to the lower.

Whereas we can model the loss in the microstrip line devices, we have found no way to do so in the CPW-based HEBMs. Clearly, it would be beneficial to have a way to estimate the loss in this type of transmission lines as well, so that rf coupling schemes can be optimized for the lowest loss.

Although the final results are very similar, there are clear differences between the equivalent circuit approximation and the MoM-method to calculate the coupling. The MoM-method is slow and not very transparant, but rigorous and takes into account the interdepence of the elements (filter sections, antenna slot, ...). It can be used to calculate the rf properties of almost all geometries that are of interest. Some care is required in applying the Momentum-program at the frequencies that are of interest to us, since

the program has been designed to work reliably up to a few hundred GHz only. However, if some precautions are taken, the program still allows one to simulate the structures at much higher frequencies.

The method using the equivalent circuit is fast, transparant and easy to work with. However, the interdependence is not taken into account, since each element is assumed ideal. The method can in principle be applied to any circuit that can be described by an equivalent circuit for which the impedance of each element is known. To calculate another structure, the program has to be changed only slightly. The difficult part is to accurately obtain the separate impedances.

For all designs, the geometry is such that no insurmountable difficulties in production are foreseen, i.e. all required line widths are larger than $\sim 1\ \mu$m, all slot widths are no less than $\sim 0.5\ \mu$m and the metal layers should be about 200 nm thick. It should be feasible to produce these features using deep UV lithography or, preferably, e-beam lithography.

4.7 Conclusions

We show a novel design for coupling of HEB microbridges to a double slot antenna that is optimized for use at 2.5 THz. We also show the simulation of the direct response of a device described in literature[1].

For the latter type of device, we employ two methods to calculate the direct response of the detector designs. In one method, a MoM-approach is used to calculate the embedding impedance Z_{embed} of the nanobridge. The other is based on an equivalent circuit representation, coupling the impedance of each separate element to find the embedding impedance of the bolometer. The transmission (or coupling) from the antenna to the bridge is found by coupling Z_{embed} to Z_{HEB}. In the frequency range of interest, both methods yield comparable results. For a typical device, the peak in direct response is found around 2.2 THz and has a 3 dB-bandwidth of 1.4 THz.

Using microstrip line technology, it is possible to design a structure consisting of antenna–transformer–filter–HEB which yields a coupling of about 90%. The filter is designed to have low impedance in order to minimize its influence on the antenna and to provide good filter capacities. Its bandwidth is shown to be wide enough to be efficient for all frequencies of interest. Due to the large possible variation in the characteristic impedance of the consti-

tuing parts, it is quite straightforward to adapt the design if required. In a typical microstrip line, the loss in the metal layers is estimated to be 2–3 dB per wavelength. The device we simulate has its response maximum f_c at 2.6 THz and a bandwidth of 1.4 THz.

References

[1] B.S. Karasik, M.C. Gaidis, W.R. McGrath, B. Bumble and H.G. LeDuc, IEEE Trans. on Appl. Supercond. **7**, 3580 (1997).

[2] Hewlett Packard Advanced Design Software, Momentum Planar Solver.

[3] D.M. Pozar, *Microwave Engineering*, Addison-Wesley (1990).

[4] R.L. Kautz, J. Res. of the Nat'l. Bureau Std. **84**, no. 3, 247 (1979).

[5] M. Bin, M.C. Gaidis, J. Zmuidzinas, T.G. Philips and H.G. LeDuc, Appl. Phys. Lett. **68**, 1714 (1996).

[6] P. Dieleman, T.M. Klapwijk, J.R. Gao, H. van de Stadt, IEEE Trans. on Appl. Supercond. **7**, 2566 (1997).

[7] A. Karpov, D. Miller, F. Rice, J. Zmuidzinas, J.A. Stern, B. Bumble, H.G. LeDuc, Proceedings of the 8th Int. Superc. Electronics Conf., Osaka, Japan, June 19–22, pp. 521–522 (2001).

[8] S.S. Gearhart and G.M. Rebeiz, IEEE Trans. on Microwave Theory Tech. **42**, 2504 (1994).

[9] J. Zmuidzinas and G. Chattopadhyay, private communication.

[10] M. Kominami, D.M. Pozar and D.H. Schaubert, IEEE Trans. on Antennas and Propagat. **33**, 600 (1985).

[11] M.J.M. van der Vorst, Ph. D. thesis, Eindhoven University of Technology (1999).

[12] J. Zmuidzinas and H.G. LeDuc, IEEE Trans. on Microwave Theory Tech. **40**, 1797 (1992).

[13] EEsof, TouchStone Series IV.

[14] B.C. Wadell, *Transmission Line Design Handbook*, Artech House, Inc., ISBN 0-89006-436-9 (1991).

[15] S. Sridhar, J. Appl. Phys. **63**, 159 (1988).

[16] L.R. Swart, M. Sc. thesis, Rijks*Universiteit* Groningen (1999).

[17] R.A. Wyss, A. Neto, W.R. McGrath, B. Bumble and H.G. LeDuc, Proc. 11th Int. Symp. Space THz Techn., Ann Arbor MI, May 1–3, pp. 379–388 (2000).

[18] W.F.M. Ganzevles, J.R. Gao, N.D. Whyborn, P.A.J. de Korte and T.M. Klapwijk, Proc. of the ESA Workshop on Millimetre Wave Techn. and Appl., Espoo, Finland, June 21–23, pp. 504–509 (1998).

[19] G. Yassin and S. Withington, J. of Phys. D, **28**, 1983 (1995), and G. Yassin and S. Withington, ESA Technical Report RDG 4, 1995 (unpublished).

[20] Values for v_F taken from C. Kittel, *Introduction to Solid State Physics*, 7^{th} ed., Wiley and Sons, NY (1996), other values are determined experimentally.

[21] D.C. Mattis and J. Bardeen, Phys. Rev. **111**, 412 (1958).

[22] A.B. Pippard, in *Advances in Electronics and Electron Physics*, **VI**, ed. L. Marton, New York, Academic Press (1954).

[23] M. Bin and J. Zmuidzinas, private communication.

[24] G.E.H. Reuter and E.H. Sondheimer, Proc. Roy. Soc. (London) **A195**, 336 (1948).

Chapter 5

Device fabrication

This Chapter describes the development of fabrication processes for both coplanar waveguide (CPW) and microstrip line coupled nanoscale Nb HEBMs. We describe the fabrication of the superconducting nanobridge, its normal metal cooling pads and the rf coupling environment. The process we have developed to produce CPW-coupled devices is compared with a process using an Al etch mask and one having an in situ Nb/Au interface as described in literature[1,2].

5.1 Introduction

The requirements that are put on the fabrication by the desired rf properties are strict. The first constraint is put by the astronomers: they want a large (several GHz) IF bandwidth, thus requiring a fast device. Since Nb HEBMs rely on diffusion cooling, the thermal relaxation time τ_{diff} of the device is proportional to $L_{\mathrm{bridge}}^2/(\pi^2 D)$ in which L_{bridge} is the device length and D the diffusion constant[3]. Since the IF bandwidth is defined as $f_{3\mathrm{dB}} = (2\pi\tau_{\mathrm{diff}})^{-1}$, for a typical device ($L_{\mathrm{bridge}} = 200\,\mathrm{nm}$ and $D = 1.6 \cdot 10^{-4}\,\mathrm{m^2 s^{-1}}$) we find a theoretical bandwidth of slightly over 6 GHz. To reach this length regime, the use of e-beam lithography (EBL) is required. Possibly, deep ultra violet (DUV) lithography can be used. However, that is a much less flexible technique since it needs expensive, sophisticated mask plates. Furthermore, it is not yet capable of producing state-of-the-art HEBMs, which are in the sub-100 nm region.

Second, normal state resistance $R_N = R_\square \cdot L_{\mathrm{bridge}}/(w)$ of the device, in

which w is the bridge width and $R_\square$ is the square resistance of the Nb. $R_\square$ has to have a value between 15 and 75 Ω. If R_N is not in this range, a considerable impedance mismatch to the rf environment will occur. The maximum value obtainable for $R_\square$ is about 15 Ω for our Nb films. This is because for use at ℓHe-temperatures, the critical temperature T_c should be somewhat above 4.2 K, say 6 K. When the films become thinner, T_c drops below this value, thus setting a lower limit for the thickness. Since the length of the bridge is set by the requirements on the IF bandwidth, the only free parameter is the bridge width w. As is clear from the discussion above, w should be of the order of 200 nm. Again, this can only be reached by EBL.

A third constraint is put by the frequency of operation. Nowadays, the rf frequencies of interest are well in the THz range ($\sim$ 2.5 THz). The lateral dimensions of the rf coupling structures are required to be well below the wavelength of the incoming signal (in free space, $\lambda = 120$ μm at 2.5 THz) and the thickness should be at least a few times the penetration depth $\delta = 50$ nm of the radiation. Good control of the lithography– and metal deposition steps is required. Again, next to EBL, DUV is a candidate, but yields problems in lift-off due to limited resist thickness.

Lastly, since these detectors are meant to be used in an instrument, it is important to have good reproducibility and yield in the process. The people building the receiver need several devices showing very similar characteristics.

Until the work of Wilms Floet[4], only one —rather successful— recipe for the production of Nb diffusion cooled HEBMs was developed (Bumble and LeDuc[2]). There are two main differences between that process and the one used by Wilms Floet. Bumble and LeDuc use

1. an in situ Nb/Au bilayer

2. a self-aligned, metal etch mask

The main advantage of this process is the clean Nb/Au interface, yielding a good transmissivity. No removal of the Nb-oxide is necessary when depositing the Au cooling pads. This probably allows for adequate removal of hot electrons and thus a large IF bandwidth. Besides, using a metal (Au) etch mask ensures a high selectivity between the Nb and Au in the definition of the bridge width. Due to the rather thin (25 nm) metal layer, hardly any

underetch of this metal will occur. This guarantees a good pattern transfer into the Nb layer. The disadvantage of this process is in the removal of the Au etch mask after etching the Nb. The Au is removed in an Ar-plasma by sputter etching the Au. The end point of this etch is hard to determine since the thickness of the mask is uncertain due to previous processes, resulting in reduced superconducting properties when etched too long, or a metallic short when the Au is not removed completely. Apart from that, it introduces an additional deposition step: the Au etch mask deposition.

5.2 Process outline of co-planar waveguide-based HEBMs

Fig. 5.1 sketches the process flow we have developed for the production of CPW-coupled HEBMs. HEBMs relying on quasi-optical coupling are usually made on a high-resistivity Si wafer. We use double-sided polished 50 mm wafers with resistivity $\rho > 1\,\mathrm{k}\,\Omega$ and (111) orientation. Si with a high resistivity is used because the incoming radiation will then much less be absorbed by free electrons in the Si. Since the device is operated at low temperature, the freeze-out of the electrons will decrease the absorption loss even further. The wafers are cleaned in a standard RCA-process[5].

To define alignment markers, shown in Fig. 5.1[a], a double layer PMMA system is used as a lift-off mask. First, a layer of $< 180\,\mathrm{kg/mole}$ PMMA, 4% dissolved in chlorobenzene is spun on, yielding a thickness of 160 nm. This layer is baked at 120°C for 5 min.. The baking temperature is kept low because the critical temperature T_c of a thin Nb film decreases rapidly when baked at higher temperatures[6]. A top layer of 350 kg/mole PMMA, 4% in ortho-xylene is spun on and baked in an identical way. The total thickness now becomes 330 nm. 20 μm × 20 μm markers are defined using a Leica PG5 HR FEG electron beam pattern generator (EBPG). It should be noted that this step can well be performed using optical lithography. Since no suitable mask set was present, the EBPG has been used. Whenever a PMMA-based resist sytem is used, an oxygen descum (30 sec., 20 W, 6 μBar, -180 V) is done after development (standard: 30 sec. IPA:MIBK 3:1, stop: 30 sec. in IPA) to remove remnants of PMMA in the opened-up areas. The markers consist of 6 nm Al as an adhesion layer and 75 nm Au and are, as are all sputtered metal layers, deposited in a Nordiko 2000 sputtering system.

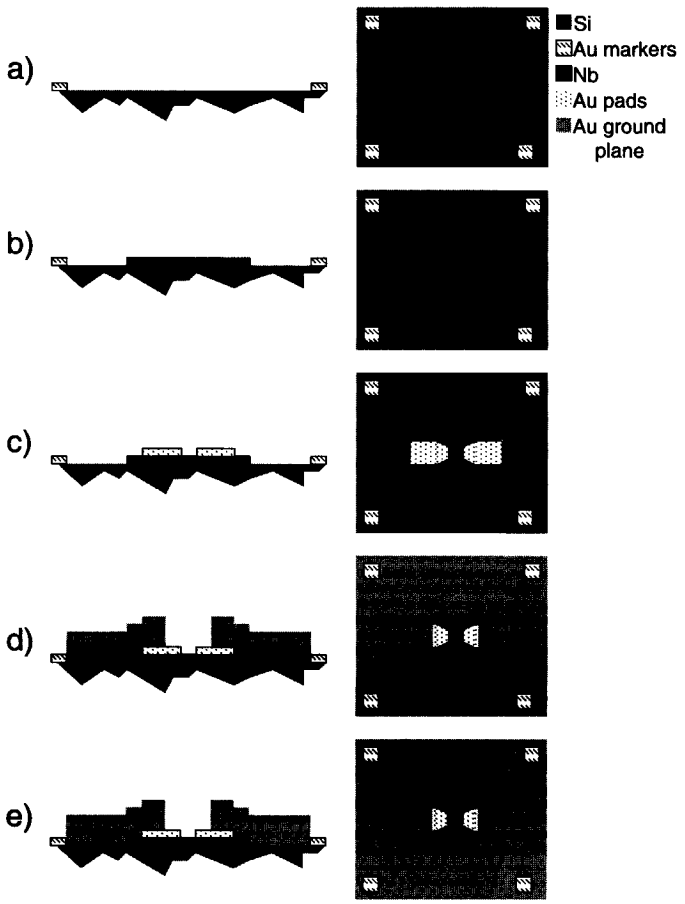

FIGURE 5.1. [a] Deposition of alignment markers. [b] Nb patch deposition. [c] Cooling pads definition. [d] Deposition of rf groundplane, including CPW lines and contacts. [e] RIE etch of the nanobridge.

We only use dc sputtering. This system has a base pressure of $2 \cdot 10^{-7}$ mBar. Since oxygen is well known to decrease the critical temperature of Nb (see, e.g. Ref. 7), it is important to keep H_2O– and O_2-partial pressures below — in our case — $5 \cdot 10^{-8}$ mBar. To effectively pump out the remaining water and oxygen from the vacuum chamber, care is taken to provide enough

gettering material by pre-sputtering Nb. Substrates are mounted onto a 9 mm thick, 100 mm diameter Cu chuck. To improve thermal contact, vacuum oil is applied between the wafer and chuck. The distance between the 75 mm diameter target and the chuck is 100 mm.

From here onwards, we have tried three routes to produce the HEBMs. These routes will be described below.

Ex situ processing of the Nb/Au interface

With the above markers defining a frame of reference for the EBPG, we deposit Nb patches with typical dimensions of 5 μm $\times$ 5 μm as depicted in Fig. 5.1[b]. We use the PMMA resist system described above. The use of these patches — instead of a blanket film — drastically reduces the time needed in the EBPG for the last step and avoids Nb being present under the rf ground plane. Since Nb is rather lossy at frequencies above the gap frequency, this could be a contribution to the reduction of the sensitivity of the device. The thickness of these patches is used to tune the square resistance $R_\square$ of the Nb. To get $R_{\square,10K} \approx 15\,\Omega$, we need a thickness of about 12 nm. To accurately control the layer thickness by time, we sputter at a rate lower than about 0.4 nm/s (power 130 W, pressure p = 11 μBar). We obtain an error margin of about 5% in sputtering time. Thickness measurements using an atomic force microscope (AFM) confirm the film thickness to be within 1 nm of the desired value.

At this point, the process we have developed fundamentally differs from those reported in literature[1,2,8]. Bumble and LeDuc[2] deposit an Au protection layer *in situ*. We, however, pattern Au cooling pads (5 μm $\times$ 2 μm, separation downto 80 nm), again using the double layer PMMA in the EBPG (Fig. 5.1[c]). Prior to depositing the Au, we remove the native Nb oxide using a 2 min. Ar standard plasma (conditions: rf power 200 W, 300 V, pressure 6 μBar, performed in two steps of 1 min. to avoid excessive heating). In situ, 15 nm Au is sputter deposited. The sample is taken out and put into an e-beam evaporator ($p_{base} \approx 2 \cdot 10^{-7}$ mbar). 100 nm Au is then evaporated at $p_{evap} \approx 2 \cdot 10^{-6}$ mbar, 0.5 nm/s. In this step, also the markers for all following steps are defined in order to keep all further alignments relative to the cooling pads. We do not use a per-die alignment, but rather a set of 4 markers at the edge of the wafer. The accuracy of the stage and its laser interferometer give us an alignment accuracy of better than 50 nm over the

wafer.

Fig. 5.1[d] shows the definition of the rf ground plane and contact wiring, which are defined in a double layer resist system. Because of the critical alignment (better than 250 nm) and small slot widths (down to 400 nm) we use the EBPG. Commercially available photoresist (Microposit S1813[9]) is used as a spacer layer (1420 nm thick). A negative-tone e-beam resist (SNR M2 : xylene = 3 : 1[10]) is used as the top layer. During development, only the top layer is removed. The Microposit 1813 is etched through in an O_2-plasma (p = 6 μBar, 30 W rf, $V_{bias} = -120$ V). During etching, the SNR forms an etch stop layer containing SiO_2. The end point of this process is detected using a laser interferometer. To obtain an undercut resist profile suitable for lift-off, we over-etch 15% of the time needed to etch through the spacer layer at p = 200 μBar, 10 W rf, −20V. This process allows us to deposit — and lift-off — up to 400 nm thick Au with slots 400 nm wide and several tens of microns long. Fig. 5.2 shows a scanning electron micrograph of a resist line defined in such a system.

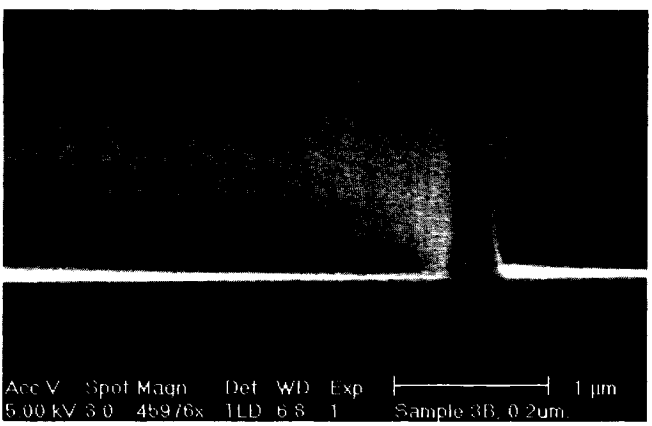

FIGURE 5.2. SEM micrograph of the profile of a narrow line defined in the bilayer resist system used in the deposition of the rf ground plane. Due to less optimized etching conditions for the resist line shown here, the profile is believed to be even better in the recipe used in device production. The nominal width of the line at its top is 200 nm.

After a standard 2 min. Ar sputter etch, a 6 nm Al adhesion layer is deposited in the sputtering machine. In situ, 15 nm Au is sputtered to prevent oxidation of the Al. The wafer is transfered to an e-beam evaporation machine, in which about 225 nm Au is deposited. This gold has a dc conductivity of $\sigma_{4.2K} = 4.7 \cdot 10^8\,\Omega^{-1}\mathrm{m}^{-1}$. In one batch (ES 4_3), however, sputtered Al is used as the material for the rf ground plane in order to have a better step coverage. The Au layer is lift-off in boiling acetone. Ultrasonic agitation is applied to remove the Au rims, left over from the resist edges. This does not affect the structures in the Au.

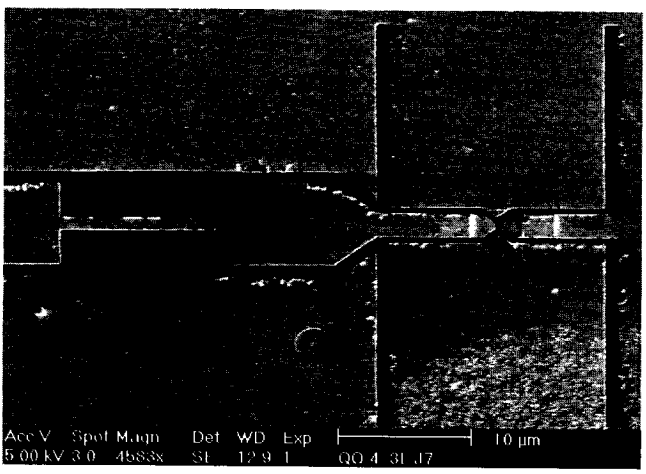

FIGURE 5.3. SEM micrograph of a 2.5 THz twin slot antenna after lift-off.

The last EBPG-step serves to define the etch mask of the Nb bridge. In a double layer PMMA system (both layers 350 kg/mole in ortho-xylene to reduce undercut or underetch), we only have to open up the Nb patches, except the bridge. The Au is not opened up in this step. This both reduces writing time and avoids too large patches of metal being exposed in the etch step. The latter is suspected to cause fluctuations in etch rate between large and small Nb areas in the last step.

As a last step, the Nb patch is etched away in CF_4 + 3% O_2. The end point of the etch can be accurately determined by the laser interferometer,

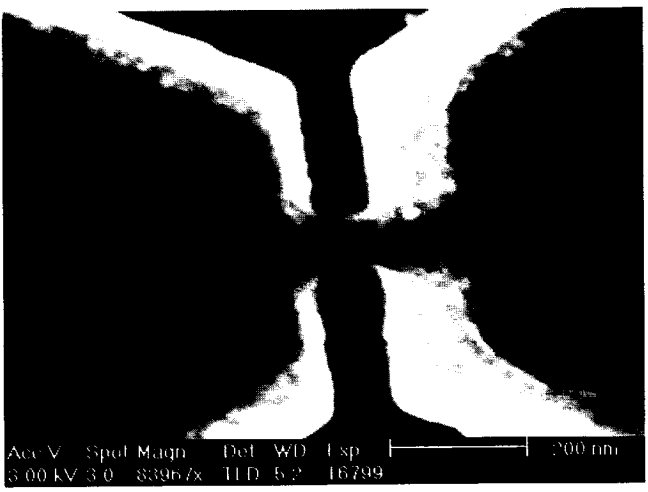

FIGURE 5.4. SEM micrograph of the PMMA etch mask used to define the nanobridge. This device has dimensions 60 nm × 80 nm.

as can be seen in Fig. 5.5. To be sure to have removed all Nb, we over-etch for 60 sec. This allows the Nb in the narrow slots to be removed completely. The PMMA is thick enough to withstand some 10 min. of etching, whereas a total etching time of about 5 min. is needed.

After etching, the wafer is rinsed in water and the PMMA is stripped in acetone. We dice the wafers in a standard semiconductor dicing machine. To avoid devices to be damaged by electrostatic discharge (ESD), all devices are

TABLE 5.1. DC properties of the metal layers in batch ES 4_6.

	$R_{\square,10K}(\Omega)$	RRR	$\sigma_{10K}(\Omega^{-1}m^{-1})$	thickness (nm)	$T_c(K)$
Au_{pads}	0.063	3.6	$1.6 \cdot 10^8$	100	–
Al_{rf}	0.076	2.9	$0.7 \cdot 10^8$	190	–
Nb	6.7	2.0	$0.1 \cdot 10^8$	14	7.2

interconnected such that all nanobridges are shorted to the ground plane. It

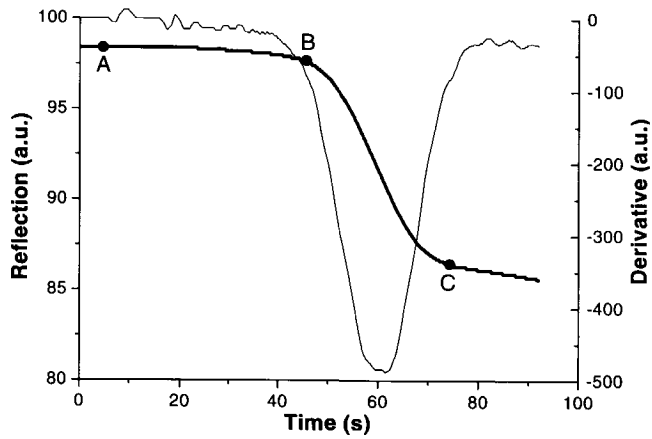

FIGURE 5.5. End point detection signal vs time in the bridge etch. Shown are the signal (thick line) and derivative (thin line). In point A, the plasma is started. B indicates the point when the Nb-oxide is removed. In C, the Nb is removed. Since the signal is obtained from a large window, 60 sec. over-etch is applied to allow the small slots to be completely cleaned from Nb.

has proven necessary to use cooling water that has a lower resistivity than usual DI water while dicing to avoid charge build up on the dicing blade. We hypothesize that upon cutting the shorts, this charge flows through the device, which is then damaged. Either tap water or carbonated water will serve for this purpose. Once the devices are diced, no ESD-security measures are left. Therefore, extreme care is taken in all further handling. The devices are then measured in a DC setup to select those promising for rf use.

The Al etch mask

A second recipe to produce HEBMs we have developed uses an Al etch mask instead of the PMMA mask described in Section 5.2. Instead of the PMMA etch mask as shown in Fig. 5.1[e], we also produce devices along the route proposed in literature[1,8]. Instead of defining a PMMA bridge, we sputter deposit a 30 nm thick Al bridge (typical dimensions 200 nm × 200 nm) by a

lift-off in a double layer PMMA system. To avoid interference between Nb and Al[11], we do not remove the native oxide on the Nb. The Al is lift off, after which the etch is performed as described above. To avoid shorting the bridge, the Al is removed afterwards in a 2 min. wet etch in a photoresist developer (Shipley MF 351 developer[9]). This process is fully compatible with the process we have developed before. Its main advantages are the larger control of the bridge width due to the absence of under-etch and the very large selectivity between Nb and Al in CF_4/O_2. The easy removal of the Al in a selective wet etch is again a large advantage of this process over that using an Au bridge mask[2].

In situ processing of the Nb/Au interface

To also obtain the advantages of the in situ interface between the Nb and the cooling pads, in our third fabrication approach we deposit patches of a Nb-Au bilayer (10/15 nm thick). After defining the cooling pads and rf ground plane (identical to the first process), we remove the Au of the bilayer. We do this by Ar sputter etching the wafer (no resist applied) in the Nordiko at an etch rate of 9 nm/s, very similar to the standard sputter cleaning performed before any deposition step. To avoid any unwanted masking in the following reactive ion etch by Au that has not been removed, we apply a 100% (time) over etch. To minimize heating effects, we split the total of 3 min. into 3 equal steps with a cooling pause in between. At this point of the process, we are at exactly the same point as shown in Fig. 5.1[d]. We then use either a PMMA or Al etch mask to define the nanobridge.

5.3 Process outline of microstrip-line based HEBMs

To produce the microstrip line devices described in Ch. 4, a fabrication process for this type of HEBMs is developed.

Again, high-ρ (> 1 kΩcm), double-sided polished Si is used as a substrate after being cleaned in an identical process as described above. In the first fabrication step, shown in Fig. 5.6[a], a thick Au layer of 250 nm is evaporated onto the substrate in a similar evaporator as is described in Section 5.2. To define the lift-off mask for the rf groundplane and dc contact pads,

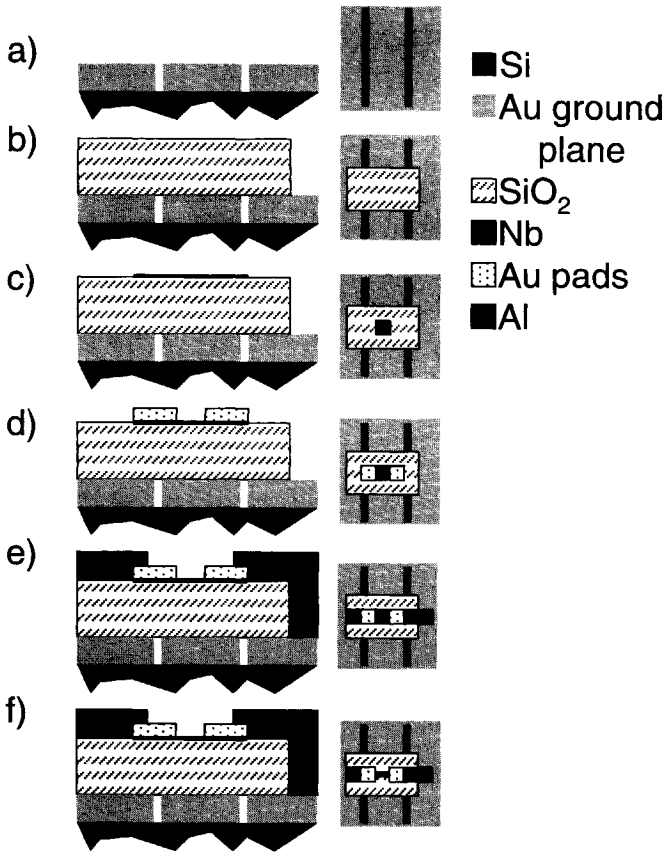

FIGURE 5.6. Process flow for the microstrip line coupled HEBMs. The cross section is taken along the line A-A' (Fig. 5.7). The picture is not to scale. [a] RF ground plane deposition. [b] Dielectric deposition. [c] Deposition of the Nb patches. [d] Definition of the Au cooling pads. [e] Deposition of the top wiring layer. [f] Nanobridge definition.

Microposit 1813 is used as a near ultra-violet (NUV) photoresist in a Karl Süss contact printer. In this layer, 1 alignment marker is defined per die for use in consecutive steps in the EBPG.

Using Microposit 1813 as a NUV-resist, 250 nm SiO_2 is deposited in a Leybold Z400 sputtering machine and patterned by lift-off in the areas where

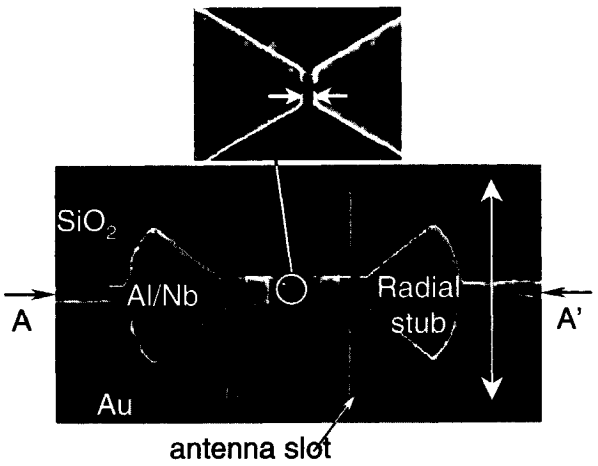

FIGURE 5.7. SEM micrograph of a microstrip line coupled HEBM. The vertical arrow indicates 31 μm. The smaller picture shows the Nb nanobridge itself. The distance indicated by the arrows is 200 nm.

the microstrip line will be located as can be seen in Fig. 5.6[b]. Because SiO_2 does not stick to the Au very well, we first deposit about 2 nm Ti by evaporation and subsequently oxidize it. The oxidization serves to prevent rf currents to run in the lossy Ti[12].

We then deposit 16 nm Nb and pattern patches of $12\,\mu\text{m} \times 12\,\mu\text{m}$ on top of the SiO_2 using lift-off in NUV resist as shown in Fig. 5.6[c]. The EBPG is used to define the bridge length by writing the cooling pads in the standard double layer PMMA system. The cooling pads are formed by depositing 80 nm Au with electron beam evaporation in the same way as was described in Section 5.2 (Fig. 5.6[d]).

The top wiring layer of the microstrip line consists of a bilayer of 550 nm Al and 75 nm Nb (see Fig. 5.6[e]). To obtain a good step coverage, the layers are sputter deposited. Since the smallest lines in this layer are over 1 μm, we use lift-off in optical resist instead of an EBPG-process as is necessary in the ground plane of CPW-based devices. Al is used instead of Au because its adhesion to the SiO_2 is better. The Nb layer here is used to reduce dc- and IF series resistance. For the same reason, we add 90 nm thick Nb on

the IF CPW-transmission line.

In the last fabrication step, we define the bridge width by reactive-ion etching in a mixture of CF_4 + 3% O_2, as is shown in Fig. 5.6[f]. The etch mask is again a double layer PMMA resist (both layers 350 kg/mole in ortho-xylene) patterned by the EBPG.

In contrast to typical SIS mixers, the superconducting bridge acts as part of (i.e. it is in series with) the top wiring layer. This means an electrical contact between the top wiring layer and the ground plane is needed. In our case this is established via a step coverage on the vertical wall of the SiO_2 (Fig. 5.6[e]). This coverage turns out to be rather difficult, since SiO_2 tends to form high and sharp edges after lift off. We overcome this problem by sputter depositing a *thick* (625 nm Al/Nb) wiring layer.

5.4 Discussion

All fabrication processes described in this Chapter yield devices showing proper dc characteristics. Details on the device characterization will be given in Ch. 8. In the devices we have fabricated we have observed dc characteristics comparable to those reported in literature[1,8,13,14,15].

We observe rather large variations in the T_c of the Nb, whereas the value of $R_\square$ does not seem to vary much. Although no research was done on the chemical composition of the Nb thin film, based on literature[7] we state that the presence of O_2 and H_2O in the sputtering system strongly reduces the superconducting properties of the Nb. A solution to reduce this effect can be found in a long (30 min.) pre-sputtering of Nb, assuming that the Nb deposited in this process acts as a strong getter pump for O_2 and H_2O. Besides, it guarantees that the target surface is as fresh as possible. We make sure that the oil used to improve thermal contact between the chuck and the wafer is not exposed to the plasma and we use a dedicated (Nb-only), clean chuck for the thin film deposition. Comparing T_c of the film before and after the whole process, we find a reduction of $\Delta T_c = 0.5$ K. This reduction is attributed to the baking steps used in the process. The R(T)-curves of the devices can in general be modeled well by the model given in Ref. 16. Sometimes, however, a tail develops at temperatures lower than $T_{c,pads}$. In NbN, this tail has been observed by other groups[17] and is attributed to damage to the film in the Ar sputter etch prior to deposition

of the cooling pads.

Due to the superconducting proximity effect, T_c of the Nb under the cooling pads is reduced. This reduction is caused by electrons from the normal metal leaking into the superconductor and Cooper pairs leaking into the normal metal. The more transparant the interface, the stronger this effect. The difference ΔT_c between $T_{c,\,bridge}$ of the bridge and $T_{c,\,pads}$ of the Nb under the cooling pads is an indication for the transparency. In the batches produced with the ex situ Nb/Au interface, ΔT_c does not exceed 0.8 K. In the batches having an in situ interface, $\Delta T_c = 1.2\,K$. When T_c under the pads is too high, a heat trap exists between the superconducting parts of the pads and the normal region within the bridge. This slows down the device and decreases its IF bandwidth.

Using a computer program by Golubov[18], we have simulated the proximity effect in this type of bilayers. Table 5.2 shows the expected and observed reduction from a bare Nb film of indicated thickness when 110 nm Au is put on top. The expected reduction is not quite observed in the experiments:

TABLE 5.2. Proximity effect in Nb/Au bilayers

Nb (nm)	$T_{c,\,Nb}$ (K)	Red. (%)	$\Delta T_{c,theor.}$ (K)	$\Delta T_{c,exp.}$ (K)
14 (IS)	7.0	32	2.2	1.2
10 (ES)	7.0	40	2.8	0.8

the experimentally observed reduction for the thinner (ex situ) Nb film is smaller than that of the thicker film. We think that this is caused by a less clean (due to exposure to ambient conditions prior to Au deposition) and more damaged interface due to Ar sputter etching before cooling pad deposition. Also for the thicker in situ interface, the suppression of T_c is smaller than expected. For this sample, a bilayer (14 nm/15 nm) has been sputtered, immediately after which 95 nm Au has been evaporated in another vacuum chamber. When the transmission between both Au layers is not optimal, the effective Au thickness is smaller, resulting in a smaller suppression of T_c.

ΔT_c observed by Wilms Floet[4] using the ex situ process is similar to the

ΔT_c observed in the ex situ process described in this work. Baselmans[19] has studied similar bi-layers produced in the same equipment. For reasons unclear to us, he observed a transmission that is larger than predicted by the model.

The I(V)-curves obtained from devices made in an ex situ process generally differ from those made with the in situ interface. The former show less upward curvature, i.e. $\frac{d^2V}{dI^2}$, at low bias voltage. Also, the excess current (the current that seems left when the high-V curve is extrapolated to zero bias) is low or not present at all. Both these effects are attributed to heat trapping in the device. To sustain the hot spot (see Ch. 2), less additional dc heating is necessary, since some heat is present in the bridge. The trapping mechanism could be the one mentioned above. Related to this heat trapping is the fact that the dynamic range of the hot spot is small: since heat is trapped, the hot spot is already rather large, leaving no room to 'breath' with the beatings in rf power. A comparison of the rf properties obtained from devices having an in situ and and ex situ defined Nb/Au interface can be found in Ch. 8.

The yield (we define yield as dc yield: how many devices show the expected dc I(V)-curve) of the process is mainly influenced by four factors: the quality of the resist system used for the rf ground plane, the quality of the etch defining the nanobridge and the post-process handling of the devices. The fourth is present only in IS batches: the accuracy of the end point in removing the Au passivation layer by Ar sputter etching. For the last IS batches, the overall yield is around 5-10%. The ES batches have shown yields up to 70%.

The first problem causes bad lift-off and yields shorted devices. This problem can be overcome by using a thick resist system having an undercut profile. The system described above fulfills these requirements and also allows for the small ($\sim$ 400 nm) slot width required for high-frequency devices. Using this resist system has overcome most of the problems in defining the rf ground plane.

The second is responsible for ill-defined bridge geometries, resulting in too high or too low normal resistance of the bridge. This, in turn, causes less good rf matching. Solving this problem is done by etching in $CF_4 + O_2$ instead of in the SF_6 used previously, carefully controlling the etching parameters (i.e. conditioning the etching chamber and using the same etch

parameters) and using an Al etch mask, reducing the undercut and resist burning compared to etching using a PMMA mask. Since the hot spot will be formed at the weakest point of the nanobridge, in a bridge that does not have parallel sides —a problem often seen in a non-homogeneous etch—, the hot spot will grow from the narrowest point in the bridge. Since this is not necessarily the middle of the bridge and because the bridge width is not equal over the bridge, the hot spot behavior is not well defined.

The third problem usually yields open devices. Safely handling ESD-sensitive devices mainly requires discipline in following exactly the same procedure each time. Although developing the right procedure is not an easy task, it is of prime importance for doing systematic measurements on HEBMs. As the main problem areas in handling HEBMs, we identified dicing wafers, mounting the wire-bonded device into the dewar and switching the bias settings as the most dangerous operations. As discussed, dicing is done using conducting water. When measuring, the bias settings shall only be changed after connecting a resistor parallel to the device and disconnecting the device.

The last problem only applies to the in situ batches. When the passivating Au layer is removed from the Nb patch, it is hard to determine the end point of this process, since no end point detection system is available. Careful calibration of the etch time still results in a low yield with most of the devices resistive, but not superconducting. This problem may be overcome by a detailed study of the parameters involved in this etching step.

Although SF_6 can be used to etch the Nb, its major advantage for semiconductor industry (etch rates of about 1 μm/min, both in depth and laterally) is its greatest drawback in producing Nb HEBMs. Control of the end point is difficult and the isotropy of the etch process makes that the bridge is completely freestanding after about 15 sec. When this happens, it effectively thins the Nb bridge by both etching and oxidization of the bottom. We suppose that this causes many devices to show infinite resistance. It is not possible to increase anisotropy by lowering the substrate temperature. When the etch process is run below $-10°$ C, irreproducible etch rates and homogeneity are found. We have not succeeded in fabricating Nb nanobridges using pure SF_6. However, the addition of 3% O_2 passivates the Si sidewalls enough to prevent underetch and leave the Nb superconducting. The fast etch rates still cause deep trenches parallel to the bridge. Although no dis-

advantage due to these was observed, the slow etch rate of CF_4 in Si is to be preferred over the use of SF_6.

Due to the complexity of the above processes it would be a great advantage if these could be run in a dedicated tool set. Interference with other users, mainly in the critical deposition of Nb, is to be avoided. The need for a number of apparatus to be used in series (*one* typical deposition step involves a spinner/oven/EBPG/O_2–RIE/Nordiko/evaporator) requires large uptime and availability of all these machines. It is therefore recommendable to make sure that this equipment is immediately available at all times during a production run.

When comparing the CPW– and microstrip line process it becomes obvious that neither of them is a trivial process to run. The CPW-devices require the use of e-beam lithography, but can be considered 2-dimensional, i.e. no difficult step coverages are needed, whereas the microstrip line coupled devices require good step coverage on the edge of the SiO_2, but can be fabricated using conventional NUV lithography. Not enough data are available to make solid statements on which device is to be preferred from a performance point of view. Initial tests however show similar mixer sensitivity. Data on the rf performance of CPW- and microstrip line coupled devices can be found in Ch. 6 and 7, respectively.

DC measurements on CPW devices made along the both the ex situ and in situ-route show R(T)-curves very similar to those modeled by Wilms Floet *et al.* who used an ex situ-process. RF measurements at frequencies below 1 THz —such as those presented in Ch. 8 and 9 — show that the in situ-produced devices have a lower noise temperature than those produced with the ex situ process combined with the Al etch mask. No data are available at higher frequencies. However, there is no reason to assume that the situation would be different at 1.9 or 2.5 THz, for example. One should note that the noise temperature of the twin-slot (TS) antenna-based devices measured at 2.5 THz is consistently about a factor of 2 lower than that measured using the spiral antenna (SP) when comparing devices from the same batch. The IF bandwidth of the in situ process clearly is larger than that obtained in the ex situ process. (The low bandwidth in IS 1_4 is accounted for in Ch. 9.) We attribute this to the combined effect of a high interface transparency due to the in situ deposition process of Nb and Au and the absence of the physical sputter etch to remove the Nb oxide prior to the deposition of the

TABLE 5.3. A comparison between T_{rec} (K) and IF bandwidth of the IS and ES-batches.

freq (THz)	ES 2_2	ES 4_6	IS 1_2	IS 1_4
0.35		1400 (SP)		
0.45		1700 (SP)		
0.5		4900 (SP)		
0.65			1200	2400 (LP)
1.9		10000 (SP)		6800 (LP)
2.5	4100 (TS)	10000 (SP)		8900 (LP)
IF (GHz)	2.0	1.6	5.0	0.8

cooling pads. We speculate that this leaves us with better defined cooling pads and thus a higher IF bandwidth. Furthermore, due to the Al etch mask, the pattern transfer of the etch mask into the Nb is better than when PMMA is used. This yields a straighter bridge, which is in turn closer to the system assumed in the hot spot model. We note, however, that the ex situ fabrication of the device could in principle give a highly transparent interface. To do so, it is required that the Nb oxides at the surface are properly removed without introducing damage to the film. Good results obtained using such a process are found by Wilms Floet[4].

5.5 Conclusion

We have developed three different processes to fabricate Nb nanobridges: devices with an ex situ Nb/Au interface and a PMMA etch mask, devices based on an in situ interface having and devices with an Al etch mask. The details of these processes have been described in this Chapter.

For the CPW-coupled devices, two all-EBPG processes are developed. For these, we employ 2 different resist systems. One is capable of producing 200 nm wide slots in a 400 nm thick Au layer, while the other yields a

separation downto 80 nm between cooling pads of 125 nm thick Au.

The recipe to fabricate microstrip line coupled HEBMs is based on NUV lithography while the steps defining the bridge employ e-beam lithography. In this recipe, control over the step coverage from the top wiring to the ground plane is essential; this has proven the bottleneck in these devices.

Using CF_4 as an etch gas is to be preferred over SF_6 since it has a much lower etch rate to Si, thus better control over the end point.

Our recipe for the bridge definition, using PMMA as an etch mask, is simplest, although the Al etch mask gives better control over the etch.

All three processes yield devices that show dc I(V)- and R(T)-curves quite comparable to data found in literature, although there is indication that the devices suffer from heat trapping.

Best rf properties, i.e. noise temperature and IF bandwidth, are found in the devices made using the in situ recipe combined with an Al etch mask.

References

[1] M. Frommberger, F. Mattiocco, P. Sabon, M. Schicke and K.F. Schuster, Proc. 11th Int. Symp. Space THz Techn., Ann Arbor MI, May 1–3, pp. 489–500 (2000).

[2] B. Bumble and H.G. LeDuc, IEEE Trans. Appl. Superc. **7**, 3560–3563 (1997).

[3] H.S. Carslaw and J.C. Jaeger, *Conduction of heat in solids*, Oxford University Press, 1959.

[4] D. Wilms Floet, *Hotspot Mixing in THz Niobium Superconducting Hot Electron Bolometer Mixers*, Ph. D. thesis, Delft University of Technology (2001).

[5] S. Bakker, Rijks*Universiteit* Groningen, private communication.

[6] E. Miedema, Internal report, Rijks*Universiteit* Groningen (1997).

[7] J. Halbritter, Journal of the Less-Common Metals, **139**, 133–148 (1988).

[8] J. Stodolka and K. Jacobs, Proc. 12th Int. Symp. Space THz Techn., San Diego, CA, Feb. 14–16 (2001).

[9] Microposit S1813 photoresist and Shipley MF 351 photoresist developer, Shipley Company, L.L.C., Marlborough, MA.

[10] J. Romijn and E. van der Drift, Physica B **152**, 14–21 (1988).

[11] R.M. Heeres, M. Sc. thesis, nr. 423/96/Afst/FDL, Rijks*Universiteit* Groningen (1996).

[12] P. Echternach, private communication.

[13] B.S. Karasik, M.C. Gaidis, W.R. McGrath, B. Bumble and H.G. LeDuc, IEEE Trans. on Appl. Supercond. **7**, 3580 (1997).

[14] A. Skalare, W.R. McGrath, B. Bumble and H.G.Leduc, IEEE Trans. on Appl. Supercond. **7**, 3568 (1997).

[15] D. Wilms Floet, J.R. Gao, W. Hulshoff, H. van de Stadt, T.M. Klapwijk and A.K. Suurling, Proc. EUCAS, Veldhoven, The Netherlands (1997).

[16] D. Wilms Floet, J.J.A. Baselmans, T.M. Klapwijk and J.R. Gao, Appl. Phys. Lett. **73**, 2826 (1998).

[17] S. Miki, Y. Uzawa, A. Kawamaki and Z. Wang, IEEE Trans. on Appl. Superc. **11**, 175 (2001).

[18] A.A. Golubov, *Superconducting Superlattices and Multilayers*, ed. I. Bozovic, SPIE proceedings 215 (SPIE, Bellingham, WA, p.353 (1994).

[19] J.J.A. Baselmans, M. Sc. thesis, nr. 430/98/Afst/FDL, Rijks-*Universiteit* Groningen (1998).

Chapter 6

Direct response of co-planar waveguide coupled hot-electron bolometer mixers designed for 2.5 THz radiation detection[1]

We measure the direct response of a Nb diffusion-cooled hot electron bolometer mixer in a frequency range between 0.5 THz and 3.5 THz. The mixer consists essentially of a twin slot antenna, a co-planar waveguide transmission line and a Nb superconducting bridge. It is designed for use in receivers with astronomical and atmospherical applications around 2.5 THz. We calculate the impedance of the antenna, the transmission line and the bridge separately using models which are developed for frequencies below 1 THz and predict the direct response of the mixer. We demonstrate that these models can be applied to much higher frequencies. However, the measured central frequency is 10-15% lower than predicted.

6.1 Introduction

Highly sensitive superconducting hot-electron bolometer mixers (HEBMs) for radiation detection at THz frequencies are required for application in atmospheric and astronomic research. In particular, detection of 2.5 THz radiation is interesting since an important spectral line of the hydroxyl rad-

[1] This Chapter has been published in Appl. Phys. Lett. **76**, 3304 (2000).

ical OH appears around this frequency. Several HEBMs aiming for this frequency have been developed, showing very promising performance with regard to sensitivity[1–3].

A sensitive mixer requires low intrinsic noise, high conversion gain and high coupling efficiency of the radiation signal from free space to the Nb bridge. Thus, a high coupling efficiency is one of the key parameters for low receiver noise. In order to develop a receiver, which is directly applicable for observations in a telescope, and has a high coupling efficiency, we choose a coupling structure that consists of a twin slot antenna and a co-planar waveguide (CPW) transmission line. Such a coupling structure has been applied for a Schottky-mixer at 250 GHz[4]. A twin slot antenna combined with a microstrip line has been used for a superconductor-insulator-superconductor (SIS) mixer around 1 THz[5,6]. This study shows that twin slot antennas can be used and modeled up to 1 THz. A twin slot antenna/CPW combination has recently been introduced for HEBMs and evaluated experimentally[1]. This work demonstrates that such a coupling structure can work even at 2.5 THz. However, the measured peak response frequency is found to be considerably lower than expected theoretically. A question arises whether models developed and partially tested at low frequencies are also applicable for predicting peak frequency and bandwidth at much higher frequencies, such as 2.5 THz.

To address this issue we characterize the direct response of a diffusion-cooled Nb HEBM using a twin slot antenna and CPW transmission line designed for 2.5 THz with a Fourier Transform Spectrometer (FTS) and compare the results with several models.

Fig. 6.1 shows a scanning electron microscopy (SEM) micrograph of a mixer designed for 2.5 THz. It consists of a twin slot antenna, a CPW transmission line and a Nb microbridge. The CPW transmission line is used to match the impedance between the antenna and the bridge. On one end, the CPW line is terminated by the low (practically zero) impedance of the antenna ground plane. On the other end, the CPW transmission line is connected to the intermediate frequency (IF)- and direct current (DC) bias contact via a quarter wavelength ($\frac{1}{4}\lambda$) radio frequency (RF) reflection filter. A similar structure was used by Karasik *et al.*[1].

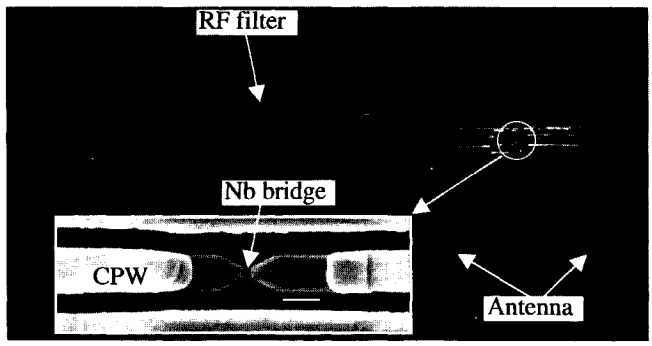

FIGURE 6.1. SEM micrograph of a twin slot antenna coupled Nb HEBM. The nominal slot length L, width w and separation s are 36.0 μm, 1.8 μm and 19.2 μm, respectively. The Nb microbridge and part of the CPW transmission line are shown in the inset, where the bar represents 2 μm.

6.2 Simulation of the direct response

We start by describing the model to calculate the intrinsic coupling efficiency η_{int} of the mixer, namely the power transmitted from the antenna to the bridge. To calculate η_{int}, we consider each antenna slot as a voltage generator in series with the antenna impedance. The RF choke filter is assumed in series with one voltage generator/antenna impedance. On one side, the microbridge sees an impedance Z_1 equal to the added filter- and slot impedance transformed by the CPW transmission line. On the other side, only the transformed slot impedance Z_2 is present. A similar approach is used for a Schottky-mixer by Gearhart *et al.*[4]. The intrinsic frequency-dependent coupling between the embedding impedance, $Z_{\text{embed}} = Z_1 + Z_2$, seen at the bridge terminals and the bolometer impedance Z_{HEB} can now be calculated using

$$\eta_{\text{int}} = 1 - \left| \frac{Z_{\text{HEB}} - Z_{\text{embed}}}{Z_{\text{HEB}} + Z_{\text{embed}}} \right|^2 . \tag{6.1}$$

The impedance of the antenna as a function of frequency is calculated using a moment method in the Fourier transform domain, developed by Kominami *et al.*[7]. In the simulation of η_{int} we take into account the decrease of

the antenna beam efficiency when the frequency is much higher than the design frequency. This effect suppresses the appearance of the second antenna resonance[8]. The characteristic impedance Z_0 of the CPW transmission line is calculated for several widths of the center conductor and the gap using a commercial software package (Momentum[9]). It is important to note that the impedances of both the antenna and the CPW are calculated for *printed slots* at the interface between two semi-infinite regions, air and substrate. Basically, the thickness of the metal layer is fully neglected. Because of this, the effective relative dielectric constant ϵ_{eff} is $\frac{\epsilon_r+\epsilon_{\text{air}}}{2}$, where ϵ_r and ϵ_{air} are the relative dielectric constant of substrate and air, respectively.

The bolometer impedance Z_{HEB} can be expressed as[10]

$$Z_{\text{HEB}} = Z_S \frac{l}{d} + Z_L, \tag{6.2}$$

where Z_S is the surface impedance of the superconducting bridge, l and d are its length and width and Z_L the impedance due to the geometrical inductance of the bridge. Z_S reduces to the square resistance $R_\square$ when the frequency is higher than the gap frequency of the bridge and the film thickness is much smaller than the skin depth[16]. Furthermore, Z_L is small, on the order of 1$\imath$ Ω for our device. Therefore, Z_{HEB} in practice equals the normal state resistance R_N. The effective impedance of the 4-section RF filter is calculated by loading each $\frac{1}{4}\lambda$-CPW section with the effective impedance of its predecessor.

Based on this model we find the maximum coupling efficiency at 2.5 THz for the following mixer geometry: for the antenna we choose length L, separation s and slot width w equal to 0.30 λ_0, 0.16 λ_0 and 0.05 L, respectively. Here λ_0 is the free-space wavelength (120 μm at 2.5 THz). For the CPW transmission line we choose the center conductor width to be 2 μm and the width of both gaps 0.5 μm, giving Z_0 equal to 39 Ω. R_N of the bridge is assumed to be 75 Ω. Using these parameters, we predict a maximum value for $\eta_{\text{model,int}}$ of 90%.

The device is fabricated on a Si wafer with a high resistivity ($\sim$ 5 kΩ·cm). The fabrication process is briefly described as follows: Nb (12 nm thick) is DC sputter deposited and patterned as squares with an area of 12 μm $\times$ 12 μm by lift-off. We restrict the presence of the Nb to the region near the bridge since Nb is rather lossy at THz frequencies. Au cooling pads are defined using electron beam lithography (EBL) and lift-off, giving

a bridge length of about 200 nm. Using deep ultra violet (DUV) lithography, the antenna and CPW structures are defined in the Au ground plane (180 nm thick). A narrow PMMA line is defined by EBL, acting as an etch mask in the final Nb etch process, resulting in a Nb bridge width of 180 nm. The critical steps in this process are the definition of bridge size, the control of R_N, and the definition of the gap in the transformer width in the CPW, determining its characteristic impedance Z_0. The device we focus on has an R_N of 41 Ω and CPW gap width of 0.8 μm. The superconducting critical temperature of the bridge is 4.8 K.

In order to verify the predictions, we measure the frequency dependent response of the mixer using the HEB as a direct detector in a FTS. The FTS measurement setup consists of a Michelson interferometer with a chopped Hg arc lamp providing broadband THz radiation. One of the mirrors is fixed, while the other can be moved over a range of 32 mm with an accuracy of 5 μm. These parameters give a maximum spectral resolution and frequency range of 5 GHz and 16 THz, respectively. The beam splitter used is a 25 μm thick Mylar sheet. To remove effects of absorption due to water, the whole optical path is in vacuum.

The device is glued onto a synthesized elliptical Si lens[17] —having a radius of 5 mm and an extension length of 1.9 mm (including substrate thickness)— and mounted in a standard cryostat. The window is of a Mylar sheet with a thickness of 40 μm. The heat filter is a 112 μm Zitex sheet[11].

The direct response in current $\Delta I(f)$ of an HEBM measured in an FTS can be described by

$$\Delta I(f) = S\eta_{int}\eta_{opt}\eta_{FTS}P_l, \tag{6.3}$$

where S is the current responsivity of the microbridge, η_{opt} the combined transmission of the window and heat filter, η_{FTS} the power transfer function of the FTS. P_l is the power spectrum of the lamp. The current responsivity S is considered to be frequency independent as long as the frequency is higher than the superconducting gap frequency, which is justified for our devices. However, the value of S is expected to depend on the mode of operation. If the operating temperature is close to T_c, the detector is operated in the 'transition edge'-regime[12]. Otherwise, the detector is in the electronic hot-spot regime2[13]. P_l is assumed to be a slowly varying function of frequency and can be considered constant throughout the frequency range of interest.

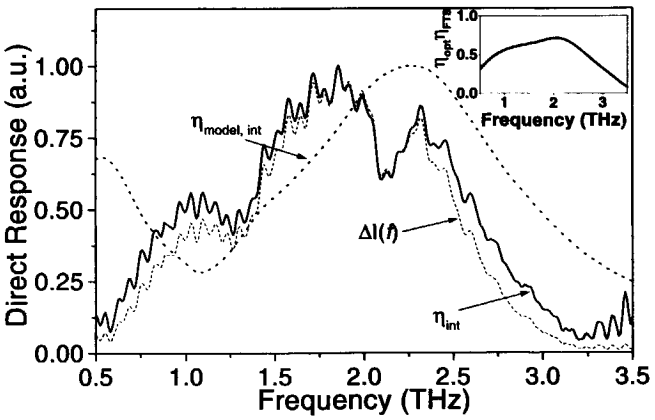

FIGURE 6.2. Direct response of the HEBM designed for 2.5 THz as a function of frequency. The dashed line gives the measured direct response ΔI(f), reflecting the product of intrinsic coupling efficiency η_{int}, the combined transmission of the window and heat filter η_{opt} and the power transfer function of the FTS η_{FTS}. The thick solid line represents the experimental η_{int}, while the dotted line represents the theoretical prediction $\eta_{\mathrm{model,int}}$. All curves are normalized to their maximum value. The inset shows a product of η_{opt} and η_{FTS}.

The transmission of the lens is not included in Eq. (6.3) since it is assumed frequency independent[14]. Thus, the measured relative response reflects the product of η_{int}, η_{opt} and η_{FTS}.

6.3 Measurements of the direct response

The direct response is measured at a constant bias voltage. The signal from the lamp is chopped with a frequency of 16 Hz and ΔI(f) is measured using a lock-in amplifier. The FTS is operated in a step-and-integrate mode with an integration time of 2 sec. The spectrum is obtained by Fourier transforming the interferogram, which is apodized using a sinusoidal apodization function. To obtain a high S, the measurements are performed at a temperature close to the superconducting critical temperature T_c.

Two similar mixers designed for 2.5 THz are measured. Fig. 6.2 shows a

typical measured relative direct response. To obtain the measured η_{int}, we divide the direct response by the product of η_{opt} and η_{FTS}. This product is shown in the inset of Fig. 6.2. η_{opt} and η_{FTS} are based on calculations including the measured index of refraction and loss of the material used (e.g. see Ref. 15). The frequency dependence of the thin lens in the FTS is not considered. The intrinsic response η_{int} is also shown in Fig. 6.2. We find a peak response frequency of 1.9 ± 0.1 THz from the intrinsic mixer response, defined as the average of the two 3 dB-points. The 3 dB bandwidth is about 1.3 THz.

To understand this result we calculate the theoretical response $\eta_{\text{int,model}}$ using the model described here. Since the actual device parameters differ from those in the initial design, the calculation of the $\eta_{\text{int,model}}$ shown in Fig. 6.2 is done using the actual values, namely $R_N = 41\ \Omega$ and $Z_0 = 46\ \Omega$ for the CPW transmission line because of a larger gap width (0.8 μm).

The model predicts a peak response frequency of 2.3 THz and a 3 dB-bandwidth of 1.3 THz. The overall response predicted coincides well with the measured curve if a frequency down shift of about 300 GHz is introduced. By doing this, we infer a peak frequency of 2.0 THz from the measured η_{int}, consistent with the value determined from the 3 dB points.

Using a standard hot/cold technique we performed heterodyne measurements on a 2.5 THz bolometer. We determine an uncorrected receiver noise temperature of 4100 K at an estimated bath temperature of 3 K and an IF-bandwidth of 1.3 GHz, about a factor of two from the best results measured with a Nb HEBM at this frequency[2].

We also calculate the relative direct response of the same mixer in an alternative way using Momentum[9]. The result is in general consistent with the simulation shown in Fig. 6.2. The peak response, however, is 2.1 THz, also higher than that measured by us.

6.4 Discussion

In both models, the quantitative difference between the measured peak frequencies and those predicted in our calculations is present only around 2.5 THz but not at low frequencies. We have measured and analyzed similar mixers designed for 1 THz, showing good agreement between measured and predicted response. Although our experimental study does not reveal

the origin of this discrepancy, we suggest that the difference is caused by neglecting the finite thickness of the metal layer. For our devices, the thickness of the metal layer has become comparable to the gap width of the CPW. For the antenna slots at 2.5 THZ, this is also the case. Reasoning qualitatively, this causes a considerable fraction of the field to run in the gap between the slot walls, giving rise to an ϵ_{eff} lower than assumed for a CPW slot in a metal film with zero thickness. This, in its turn, causes the characteristic impedance of the CPW lines to rise. Calculations show that a change in characteristic impedance has more influence at 2.5 THz than at 1 THz. Furthermore, the ratio of metal layer thickness over slot width in the antenna slots is larger in the 2.5 THz device. We suppose this changes the antenna impedance more than in the 1 THz device. Both these effects give rise to a more pronounced shift in peak frequency at 2.5 THz than at 1 THz. In order to improve the accuracy of the present models, it would be worthwhile investigating the influence of the thickness of the metal layer in the CPW transmission line.

6.5 Conclusion

In conclusion, we have measured the direct response of Nb HEBMs with a twin slot antenna/CPW transmission line combination around 2.5 THz and compared the results to the present models. We convincingly show that the measured direct response is 10-15% lower in frequency than predicted by the models, although the overall shape of the spectrum agrees with the prediction.

It becomes clear now that the mixer designed using the present models will not lead to a peak response at 2.5 THz. To achieve ultimate sensitivity at 2.5 THz one can design a mixer in an engineering way by reducing the antenna size by 15% and the CPW gap size to 0.3 μm. The impedance of the HEB device is kept at a practical value of $\sim$40 Ω. Our calculations show that this does not change the peak coupling efficiency, but the size reduction may affect other properties of the antenna. A similar experimental approach has been made by Wyss *et al.*[2].

References

[1] B.S. Karasik, M.C. Gaidis, W.R. McGrath, B. Bumble and H.G. LeDuc, IEEE Trans. on Appl. Supercond. **7**, 3580 (1997).

[2] R.A. Wyss, B.S. Karasik, W.R. McGrath, B. Bumble and H.G. LeDuc, Proc. 10^{th} Int. Symp. Space THz Techn., Charlottesville VA, March 16-18, pp. 215-228 (1999).

[3] P. Yagoubov, M. Krough, H. Merkel and E. Kollberg, Proc. 11^{th} Int. Symp. Space THz Techn., Charlottesville, VA, March 16-18, pp. 238-246 (1999).

[4] S.S. Gearhart and G.M. Rebeiz, IEEE Trans. on Microwave Theory Tech. **42**, 2504 (1994).

[5] J. Zmuidzinas and H.G. LeDuc, IEEE Trans. on Microwave Theory Tech. **40**, 1797 (1992).

[6] M. Bin, M.C. Gaidis, J. Zmuidzinas, T.G. Phillips and H.G. LeDuc, Appl. Phys. Lett. **68**, 1714 (1996), and references therein.

[7] M. Kominami, D.M. Pozar and D.H. Schaubert, IEEE Trans. on Antennas and Propagat. **33**, 600 (1985). We used a computer code of this method supplied by Zmuidzinas and Chattopadhyay.

[8] J. Zmuidzinas, private communication.

[9] Hewlett Packard Advanced Design Software, Momentum Planar Solver.

[10] J. Mees, M. Nahum and P.L Richards, Appl. Phys. Lett. **5**, 2329 (1991).

[11] Zitex G104, Norton Performance Plastics, Wayne, New Jersey, (201)696-4700.

[12] D. Wilms Floet, J.J.A. Baselmans, T.M Klapwijk and J.R. Gao, Appl. Phys. Lett. **73**, 2826 (1998).

[13] D. Wilms Floet, E. Miedema, T.M Klapwijk and J.R. Gao, Appl. Phys. Lett. **74**, 433 (1999).

[14] D.F. Filipovic, S.S. Gearhart and G.M. Rebeiz, IEEE Trans. on Microwave Theory Tech. **41**, 1738 (1993).

[15] R.J. Bell, *Introductory Fourier Transform Spectroscopy*, Academic Press, New York (1972).

[16] S. Sridhar, J. Appl. Phys. **63**, 159 (1988).

[17] T. Büttgenbach, IEEE Trans. on Microwave Theory Tech. **41**, 1750 (1993).

Chapter 7

Direct response of microstrip line coupled Nb THz hot-electron bolometer mixers[(1)]

We study the direct response of a superconducting Nb hot electron bolometer mixer (HEBM) centered at 2.5 THz incorporating an $Au/SiO_2/Al$ microstrip transmission line. The direct response is studied using a Fourier transform spectrometer (FTS). We find a peak response at a frequency of 2.1 THz, which is 20% lower than predicted based on a model neglecting the inductance effect in the microbridge.

7.1 Introduction

Superconducting HEBMs are very promising candidates to fulfill the need for low-noise, high frequency detectors using low local oscillator power in satellite-based astronomical and atmospheric observations. The practical application of these devices requires a suitable antenna like a twin slot antenna. To effectively couple radio frequency (rf) power from the antenna to the bridge, a transmission line is needed to match their impedances. Previously, the use of co-planar waveguide (CPW) transmission lines in HEBMs at 2.5 THz is reported[1,2]. An alternative is to use microstrip transmission lines, often applied to superconductor-isolator-superconductor (SIS) mixers[3].

[(1)] This Chapter has been published in Appl. Phys. Lett. **79**, 2483 (2001).

A microstrip line is chosen instead of a CPW-transmission line for several reasons. First, the characteristic impedance of a microstrip line is generally lower than for a CPW, and can be varied over a much larger range, making it easier to match a low-impedance Nb HEB. Second, in its use for SIS mixers it has proven to work very well up to about 1 THz[3]. Models to calculate properties of microstrip lines up to these frequencies are well developed. However, the lack of a rigorous closed-form expression for the characteristic impedance of CPW lines makes calculations difficult, in particular for structures containing slots with very small dimensions. Third, the presence of a microstrip line in the rf structure is expected not to disturb the antenna beam pattern. Such a disturbance occurs when a CPW is used because the ground plane is interrupted by the CPW line.

In this paper we report the first experimental realization of a quasi-optical HEBM using microstrip lines in combination with a twin slot antenna.

7.1.1 Sample Fabrication

Fig. 7.1 shows a scanning electron micrograph and a schematic cross section of the device. The twin slot antenna is formed by the two dark vertical lines in the ground plane. The three dark rectangles are the SiO_2 dielectric. On this dielectric layer, the top wiring layer is visible. Together with the SiO_2 and the ground plane, it forms the microstrip line. The radial stubs act as an rf short to the ground. From these, the microstrip line transformer feeds the signal to the Nb microbridge, which is located between the two tapered Au cooling pads. The intermediate frequency (IF) contact is made by a CPW transmission line (not shown). A fabrication process for Nb HEBMs has been developed using two-step electron beam lithography (EBL) to define both bridge length and width. Near ultra-violet lithography is used to define the rest of the device.

We use highly resistive ($> 1\ k\Omega cm$), double-sided polished Si as a substrate. In the first fabrication step, a thick Au layer of 250 nm is evaporated onto the substrate, serving as the ground plane. The ground plane contains the twin slot antenna and the IF CPW as well as alignment markers for subsequent process steps. 250 nm SiO_2 is sputtered and patterned by lift-off in the areas where the microstrip line will be located. Then we deposit 16 nm Nb using dc sputtering and pattern patches of 12 μm $\times$ 12 μm on top

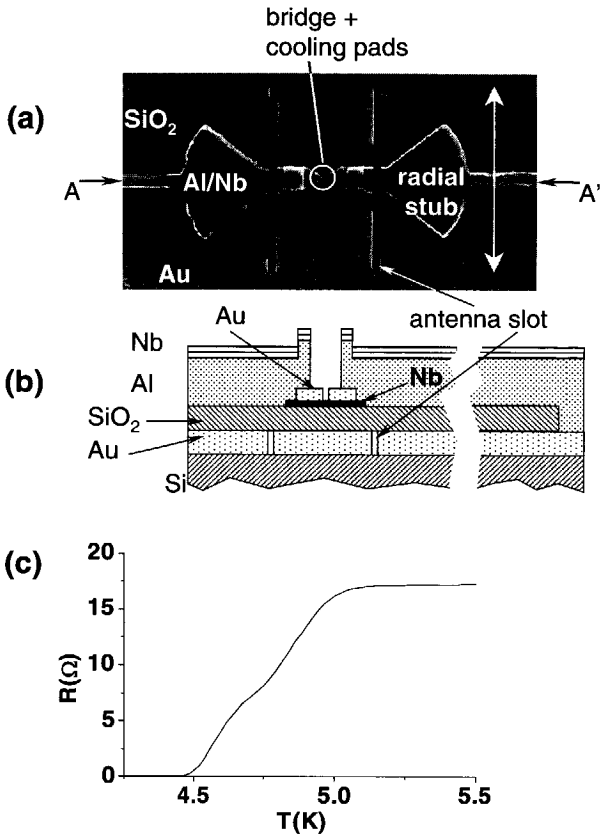

FIGURE 7.1. [a] Scanning electron micrograph of a microstrip line-coupled hot electron bolometer mixer. The arrow bar indicates 31 μm. [b] Cross-section of the sample along the line A-A'. Contact to the rf ground plane is made by extending the last section of the choke filter over the edge of the dielectric down to this plane (not shown in Fig. 7.1[a]). [c] Measured resistance vs temperature curve of a microstrip line coupled Nb hot electron bolometer mixer. The length of the microbridge is 200 nm.

of the SiO_2 using lift-off. Au cooling pads are patterned on this Nb layer to define the bridge length by EBL and lift-off using a double layer PMMA resist. The cooling pads are formed by depositing 80 nm Au with electron beam evaporation. Before deposition, the native oxide of the Nb is removed with rf Ar etching in order to achieve a high transparency between the Nb and the Au. The top wiring layer of the microstrip line consists of a bilayer of 550 nm Al and 75 nm Nb (see Fig. 7.1). The layers are sputtered and the structure is patterned by lift-off. Al is used instead of Au because its adhesion to the SiO_2 is better. The Nb layer here is used to reduce dc- and IF series resistance. For the same reason, we add 90 nm thick Nb on the IF CPW-transmission line. In the last fabrication step, we define the bridge width by reactive-ion etching in a mixture of CF_4+3% O_2. The etch mask is a double layer PMMA resist patterned by EBL.

In contrast to typical SIS mixers, the superconducting bridge acts as part of the top wiring layer. This means an electrical contact between the wiring layer and the ground plane is needed. This contact is made by extending the last section of the choke filter over the edge of the dielectric down to the ground plane (see Fig. 7.1[b]). In our case this is established via a step coverage on the vertical wall of the SiO_2. This step coverage turns out to be rather difficult, since SiO_2 tends to form high and sharp edges after lift off. We overcome this problem by sputter depositing a *thick* (625 nm Al/Nb) wiring layer.

The Nb bridge has a critical current density of 2×10^{10} Am^{-2} at 4.2 K and a relatively low critical temperature T_c of 5 K. A square resistance of 25 Ω is measured from large structures on the wafer.

Fig. 7.1[c] shows the resistance of a device vs temperature. The two critical temperatures observed, corresponding to the bridge and the Nb under the Au cooling pads, resemble the data measured from very similar microbridges by the authors[4] and by Wilms Floet *et al.*[5]. However, the shape of the curve differs from those data, in particular, from the model given in Ref.[5]. This may be attributed to the underlying sputtered SiO_2; we notice that the thin Nb films sputtered on such a layer generally show a lower T_c than those sputtered on a quartz or Si substrate.

To characterize the new coupling scheme, we measure the response of devices operated as a direct detector in an FTS. In this case, the response in current $\Delta I(f)$ can be described by

$$\Delta I(f) \propto \eta_{\rm int} \cdot \eta_{\rm opt} \cdot \eta_{\rm FTS}, \tag{7.1}$$

where $\eta_{\rm int}$ is the intrinsic coupling efficiency for the rf power transfered from the antenna to the bridge, $\eta_{\rm opt}$ the transmission of the optics which actually includes the window and heat filter, and $\eta_{\rm FTS}$ the power transfer function of the FTS[2,6].

Fig. 7.2[a] shows the measured response ΔI(f) of a device with normal state resistance $R_N = 11\,\Omega$, measured at a bath temperature of 3 K. Similar data have been obtained from several devices. The same figure shows the product $\eta_{\rm opt} \cdot \eta_{\rm FTS}$ (dashed line) as determined previously[6], but now corrected for the polyethylene lens in the FTS. To derive $\eta_{\rm int}$, we divide ΔI(f) by $\eta_{\rm opt} \cdot \eta_{\rm FTS}$. The result is given in Fig. 7.2[b]. The measured center frequency $f_{c,m}$ is found to be 2.1 THz and the full-width half maximum (FWHM) bandwidth B_m equals 1.8 THz. We also simulate the intrinsic coupling $\eta_{\rm int,sim}$ and include the theoretical curve in Fig. 7.2[b] (dashed line). We find $f_{c,\,sim} = 2.6$ THz and $B_{sim} = 1.3$ THz. In calculating $\eta_{\rm int,sim}$, we take into account both the impedance mismatch and the Ohmic losses in the microstrip lines. We do this by first determining the impedance of the antenna, microstrip line transformer and rf filter structure separately. We then calculate the coupling using the ABCD-formalism, see e.g. Pozar[7].

The impedance of the Nb microbridge Z_{HEB} is expressed as $Z_{HEB} = R_N$ [2]. The antenna we use has a length $L = 0.32\lambda_0$, a separation $s = 0.16\lambda_0$ and a slot width $w = 0.05 \cdot L$, where λ_0 is the free space wavelength at 2.5 THz. Its impedance as a function of frequency is calculated using a moment method in the Fourier transform domain, developed by Kominami, Pozar and Schaubert[8]. Details of this calculation can be found in Refs. 2 and 6. The impedance of a microstrip line is calculated based on a model[9] which was originally developed for tuning structures in SIS mixers, taking an effective dielectric constant and fringing field effect into account. The surface impedance Z_s for both top- and bottom metal layers is calculated numerically by applying Eq. (2.7) in Ref. 10 in the anomalous limit.

We simulate the characteristic impedance of a microstrip line as a function of frequency by varying the line width, thickness of top- and bottom metal layers, and thickness of the dielectric. In this way, it can be tuned from about 5 Ω to 35 Ω. The tapered cooling pads are part of the microstrip

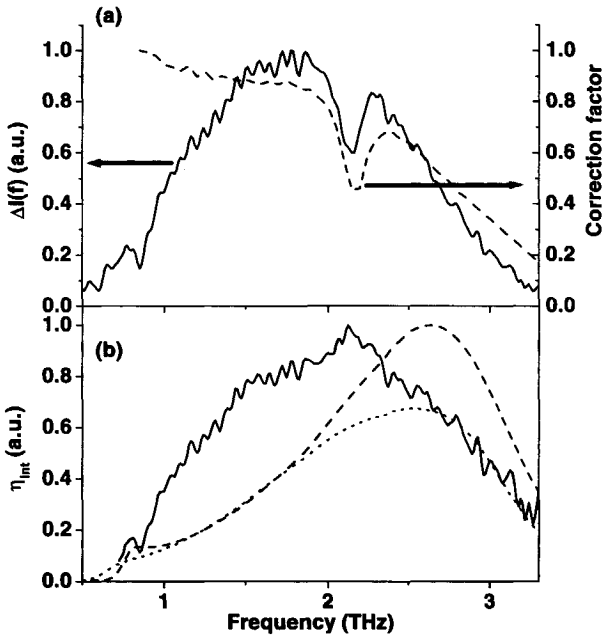

FIGURE 7.2. Relative direct response of a Nb hot-electron bolometer mixer. [a] Measured ΔI(f) (solid line) and correction factor ($\eta_{\mathrm{FTS}} \cdot \eta_{\mathrm{opt}}$) (dashed line) as a function of frequency. [b] Measured intrinsic coupling η_{int} (solid) and simulated intrinsic coupling $\eta_{\mathrm{int,sim}}$ (dashed). The dotted line shows $\eta_{\mathrm{int,sim}}$ when a very low conductivity for the top wiring layer ($\sigma_{\mathrm{top}} = 2.5 \cdot 10^6\ \Omega^{-1}\mathrm{m}^{-1}$) is assumed.

line. We model them as a series of elements with decreasing line width.

Apart from its use as a transformer connecting the antenna and bridge, microstrip lines are also applied in the rf filter (choke) structure. This is a well-known scheme to prevent the rf signal from leaking into the IF chain. The impedance of the filter structure is calculated loading each $\frac{1}{4}\lambda$ filter section by the effective impedance of its predecessor.

The calculated direct response shown in Fig. 7.2 is obtained based on the actual parameters of the device, such as the geometry, layer thickness, R_N value and dc conductivities. We use a dc conductivity of $\sigma_{\mathrm{top}} = 1 \cdot 10^8\ \Omega^{-1}\mathrm{m}^{-1}$ for the top Al layer, for the Au ground plane we use $\sigma_{\mathrm{bottom}} = 2.5 \cdot 10^8 \Omega^{-1}\mathrm{m}^{-1}$, both values measured on films similar to those in the device.

For this device, we predict a maximum intrinsic coupling efficiency of about 70%. For an optimized device of this type, we expect a maximum of over 90%[11].

We have also measured several other devices with a slightly different design regarding geometry of the top wiring layer. Devices having a rectangular coupler instead of a radial stub (Fig. 7.1[a]) do not show significant deviations in the observed direct response. On the other hand, a device having a filter with 6 $\lambda/4$ sections (instead of 2 sections as in the device discussed in this work) on either side shows a slightly lower f_c (1.8 THz) and a larger bandwidth (2.5 THz).

Using the device in heterodyne mode, an optimal, chopped Y-factor of 0.22 $\pm$ 0.05 dB has been measured. This corresponds to an uncorrected noise temperature $T_{N,\,uncorr}$ of 4200 K. It is checked that this peak is not due to oscillations in the bias circuitry nor to direct detection. This noise temperature is a few times the best noise temperature measured so far with a diffusion-cooled HEBM using CPW transmission line[12].

7.2 Discussion

Our experimental data show that the measured center frequency is 20% lower than predicted. A similar downshift in frequency has been observed in CPW-based HEBMs[1,2]. A proposal by Wyss *et al.*[13] is that the additional inductance is due to the sudden decrease in line width from the transformer to the microbridge. We explore this hypothesis by simulating microstrip line devices with such a decrease in line width. Indeed, for realistic geometries, a downshift of 10 to 15% is observed in the simulation. Assuming that the source of the downshift is understood in this way, the model for describing the peak frequency of a Nb HEBM coupled with a microstrip line works reasonably well. This suggests that the model used for the calculation of the impedance of microstrip lines works at frequencies up to a few THz. As far as we know, this is the first demonstration of using microstrip lines at such high frequencies.

The measured bandwidth is 38% higher than the prediction. This may indicate an additional loss in the RF structure. It is likely due to the presence of the thin Nb layer within the transmission lines, which extends far beyond the bridge (see Fig. 7.1[b]), and the poor quality of the Al near the SiO_2

interface. To verify this hypothesis, we calculate the surface resistance of the Al top wiring layer by using a much lower dc conductivity of the thin Nb ($\sigma_{top} = 2.5 \cdot 10^6\ \Omega^{-1}m^{-1}$) instead of its measured value. Then, we recalculate the coupling efficiency, which is also included in Fig. 7.2[b]. The new calculation gives an increased bandwidth of 1.55 THz, which is relatively close to the measured bandwidth (the difference becomes 16%), apart from a reduced coupling efficiency.

An obvious question to be raised is which coupling scheme, microstrip line or CPW line, leads to the highest sensitivity of THz HEBMs. First noise measurements on such a device show a receiver noise temperature T_N of 4600 K at 2.5 THz[14]. Because T_N also depends on conversion gain and the noise sources in the microbridge, we are not able to draw a conclusion yet. The answer has to come from a detailed experimental comparison of the sensitivity between the two types of devices.

7.3 Conclusions

In summary, we have demonstrated working Nb HEBMs designed for 2.5 THz detection using microstrip line in combination with a twin-slot antenna. The concept has been verified by measurements of the direct response. The measured peak frequency can be explained if the model takes into account the inductance of the bridge. The large bandwidth observed is mainly attributed to the presence of the thin, lossy Nb layer within the transmission line. So, to improve such devices, a crucial issue is to reduce the presence of the Nb as much as possible.

References

[1] B.S. Karasik, M.C. Gaidis, W.R. McGrath, B.Bumble and H.G. LeDuc, IEEE Trans. on Appl. Supercond. **7**, 3580 (1997).

[2] W.F.M. Ganzevles, L.R. Swart, J.R. Gao, P.A.J. de Korte and T.M. Klapwijk, Appl. Phys. Lett. **76**, 3304 (2000).

[3] M. Bin, M.C. Gaidis, J. Zmuidzinas, T.G. Phillips and H.G. LeDuc, Appl. Phys. Lett. **68**, 1714 (1996), and references therein.

[4] W.F.M. Ganzevles, J.R. Gao, D. Wilms Floet, G. de Lange, A.K. van Langen, L.R. Swart, T.M. Klapwijk and P.A.J. de Korte, Proc. 10[th] Int.

Symp. Space THz Techn., Charlottesville VA, March 16-18, pp. 247-260 (1999).

[5] D. Wilms Floet, J.J.A. Baselmans, T.M. Klapwijk and J.R. Gao, Appl. Phys. Lett. **73**, 2826 (1998).

[6] W.F.M. Ganzevles, J.R. Gao, W.M. Laauwen, G. de Lange, T.M. Klapwijk and P.A.J. de Korte, Proc. 11th Int. Symp. Space THz Techn., Ann Arbor MI, May 1-3, pp.69-81, (2000). In this paper, we ignored the transmission of the polyethylene lens in the FTS, showing a sharp dip at 2.1 THz.

[7] D.M. Pozar, *Microwave Engineering*, Addison-Wesley, Reading MA (1990).

[8] M. Kominami, D.M. Pozar and D.H. Schaubert, IEEE Trans. Ant. Propagat. **33**, 600 (1985). We used a computer code of this method by J. Zmuidzinas and G. Chattopadhyay.

[9] G. Yassin and S. Withington, J. of Phys. D, **28**, 1983 (1995), and G. Yassin and S. Withington, ESA Technical Report RDG 4, 1995 (unpublished).

[10] R.L. Kautz, J. Res. Natl. Bureau Std. **84**, 247 (1979).

[11] W.F.M. Ganzevles, J.R. Gao, N.D. Whyborn, P.A.J. de Korte and T.M. Klapwijk, Proc. of the ESA Workshop on Millimetre Wave Techn. and Appl., Espoo, Finland, June 21-23, pp. 504-509 (1998).

[12] R. A. Wyss, B.S. Karasik, W.R. McGrath, B. Bumble and H.G. LeDuc, Proc. 10th Int. Symp. Space THz Techn., Charlottesville VA, March 16-18, pp. 215-228 (1999).

[13] R.A. Wyss, A. Neto, W.R. McGrath, B. Bumble and H.G. LeDuc, Proc. 11th Int. Symp. Space THz Techn., Ann Arbor MI, May 1-3, pp. 379-388 (2000).

[14] W.F.M. Ganzevles, P. Yagoubov, J.R. Gao, T.M. Klapwijk and P.A.J. de Korte, IEEE Trans. on Appl. Supercond. **11**, pp. 570-573 (2000).

Chapter 8

The detailed characterization of a Nb hot electron bolometer mixer with a log-periodic antenna

8.1 Introduction

In this Chapter we characterize an HEB in *heterodyne* mode, i.e. acting as a mixer. Important parameters like receiver– and mixer noise temperature and gain are determined as is the IF bandwidth. A comparison between the experimentally observed characteristics and their modeled counterparts is made.

The aim of the work described in this Chapter is two-fold:

1. to completely characterize the device, including dc I(V)– and R(T)-measurements, scanning electron micrographic (SEM) data on device geometry, direct and heterodyne resonse, conversion gain and IF bandwidth and

2. to build and understand the performance of a receiver having the lowest possible noise temperature at high frequency (~ 2.5 THz).

A major hindrance in achieving these goals is the low yield in the production process: until now, only about 5% of the devices made in the in situ-runs show the required dc characteristics. Furthermore, only a fraction of those devices are found to yield good rf results. Due to the small amount of devices available, one should keep in mind that the data described here are

related to an individual device and do not necessarily represent the universal behavior of HEBMs.

This Chapter is organized as follows: first, the device geometry and its dc parameters are described, after which its direct response is described. Then, heterodyne data are reported, followed by a discussion and conclusions. The experimental set-up and the concepts used in these measurements are described in App. A.

8.2 Measured mixer characteristics

In this Section, we describe the measurements done to characterize an HEB mixer at 0.64, 1.9 and 2.5 THz. The device is called F3 and taken from an *in situ* batch designated IS 1_4. The fabrication of this type of device is described in Ch. 5. We measure the receiver noise and gain as a function of bias voltage and LO power and the IF bandwidth of the device and compare these parameters to those reported by others. These parameters are compared to those measured by other groups on similar devices.

8.2.1 Device IS 1_4 F3

The device described in this Chapter has parameters reported in table 8.1. A scanning electron micrograph (SEM) of the device is shown in Fig. 8.1. We have chosen to use a log-periodic antenna since it is very wide-band. For getting a good overview of the device's performance, this is a desirable feature: one can perform experiments in the range 0.3–3 THz, limited only by the availability of LO sources. A drawback of this large bandwidth is the increased sensitivity to direct detection, since saturation at the rf input is much more likely to occur. In this experiment, this is avoided by using the low-pass quartz/Zitex^{TM,1} filter described in App. A when measuring at frequencies below 1 THz.

The misalignment observed in this device (about 150 nm) is larger than we typically find: the alignment accuracy of the EBPG is typically better than 50 nm. This makes the device a non-ideal nanobridge. Effects of the misalignment are found in the device characterization at dc and rf frequency.

This particular device has a normal state resistance $R_N = 22\,\Omega$ (determined from its I(V) curve) and a series resistance of $R_{series} = 1\,\Omega$. Based

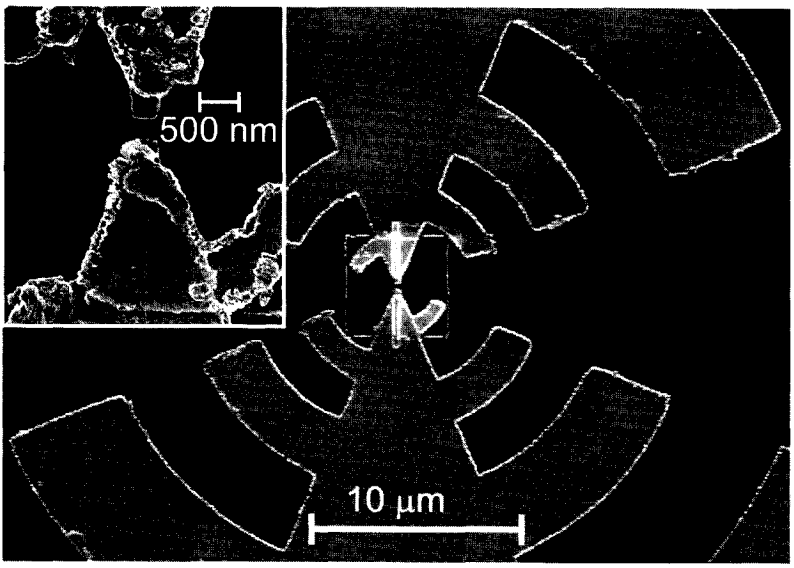

FIGURE 8.1. Scanning electron micrograph of device IS 1_4 F3. The inset shows the Nb nanobridge contacted by Au cooling pads. The length and width of the bridge are 300 nm and 400 nm, respectively. Clearly, the bridge is misaligned with respect to the cooling pads.

on the device geometry obtained from Fig. 8.1 and $R_\square = 14\,\Omega$ as measured on the same film in a large (several hundreds of μms) test structure, one expects $R_N = 10\,\Omega$. The origin of this disagreement is not clear to us. The misalignment cannot give such a large contribution to the resistance. The inset of Fig. 8.2 shows an extra transition at 5.9 K. Above the transition, the device has a resistance of $32\,\Omega$. A resistance this high is not observed in operating conditions. Apparently, the bridge is never completely driven into the normal state. In the evaluation of the rf experiments, we therefore assume a resistance of $22\,\Omega$. The residual resistance ratio (RRR) is 1.7. The critical current of the device is $I_c = 105\,\mu$A at 4.2 K, increasing to $I_c = 125\,\mu$A at 2.8 K.

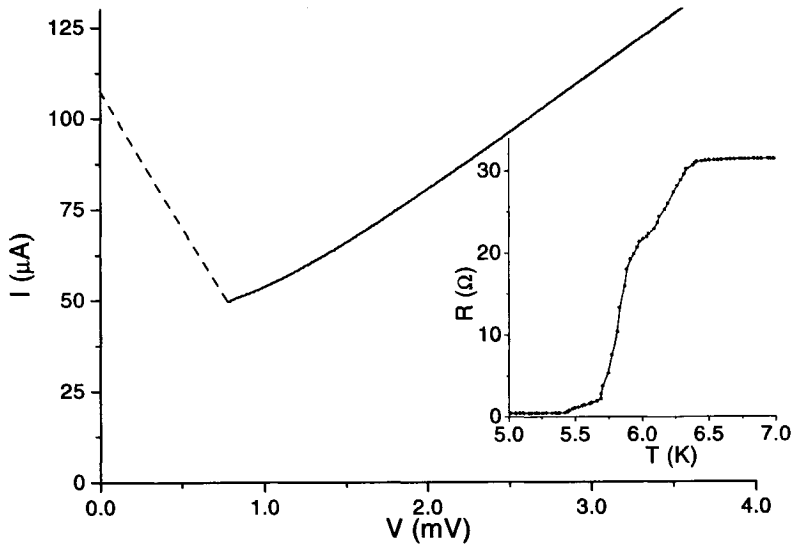

FIGURE 8.2. Unpumped I(V)-curve of device IS 1.4 F3 measured at 4.2 K. The — small — contribution of the series resistance has been corrected out. Note that no anomalies are visible in this plot, as could be expected based on the abnormal geometry observed in Fig. 8.1. The inset shows the R(T)-curve of the same device, measured at small bias. In the R(T)-curve, an extra shoulder is visible above 6 K, related to the misalignment observed in Fig. 8.1.

TABLE 8.1. Geometry of device 1.4 F3.

Antenna	log-periodic, 2×15 teeth, metal thickness: 235 nm.
Nanobridge	length = 300 nm, width = 400 nm, $R_N = 22\,\Omega$
Substrate	Si, 300 μm, $\epsilon_r = 11.7$, one-sided polished

8.2.2 FTS of the device

To get an impression of the frequency dependence of the direct response of this device, we use the device as the detector in an FTS. The device is used as a direct detector. For highest sensitivity, the detector is operated in the so-called transition edge regime, i.e. very close to its critical temperature T_c.

A 12.5 μm thick Mylar beam splitter is used in the FTS to optimally cover the expected frequency band of the device. It should be noted that no quartz/Zitex filter has been used at the 4.2 K-stage. Further details of the setup can be found in Ch. 6 and in Ref. 2.

Fig. 8.3 (dashed line) shows the spectral response of the device measured in air. The sharp dips indicated by 'H_2O' are due to absorption of the signal by water vapor in the air. The dip marked 'lens' is due to an absorption in the polyethylene (PE) lens used in the system (see Ch. 7). The sensitivity of the device is relatively flat over the region 0.6–1.8 THz. Its 3 dB-bandwidth is about 1.7 THz, not correcting for the PE lens, and its peak frequency is 1.4 THz. Note that the dip at 2.1 THz is due to the FTS itself and will not influence the sensitivity– and gain measurements described later in this Chapter.

Since no model is available to us for simulating the device response, we cannot compare the measured result to theory. However, an intuitive estimate for the theoretical upper cut-off can be made by comparing the size of the smallest tooth to the wavelength.

The highest resonance will take place between the smallest and second-but-smallest tooth. A typical dimension of the system will then be given by the second tooth, which is about 10 μm. This is equivalent to $\frac{\lambda_0}{2\sqrt{\epsilon_r}}$, so the upper frequency is on the order of 4–5 THz.

We see that this estimate is somewhat high when compared to the measured upper limit. When compared to the spiral antenna we used in earlier work[3], and one that has been used by Yagoubov *et al.*[4], the log-periodic antenna's bandwidth is about 10% larger and the cut-off is more pronounced.

One should keep in mind that the polarization of a log-periodic antenna changes with frequency. Since the signal coming from the FTS is somewhat polarized, this may influence the measurement. Furthermore, the high-frequency output of the FTS (above 4 THz) is not accurately known and may depend on frequency.

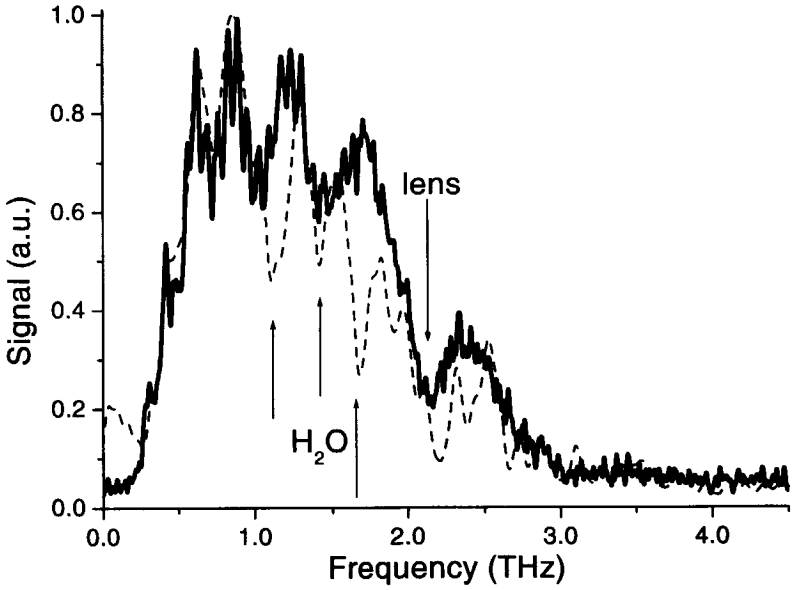

FIGURE 8.3. *Direct* response as a function of frequency. The dashed line represents a measurement with a resolution of about 20 GHz done in air. The solid line is the response in vacuum, taken with a high ($\sim$ 5 GHz) resolution. Absorption lines due to H_2O-vapor are visible in the lower resolution scan. The dip labelled 'lens' is due to the PE lens in the system. Since the polarization of the antenna oscillates with frequency, part of this dip may be due to the antenna.

From these measurements, we conclude that the log-periodic antenna indeed is a wideband antenna in the 0.5–3 THz range, although its response is decreased considerably at the higher end of the spectrum.

8.2.3 Pumped current-voltage characteristics

Fig. 8.4 shows a set of I(V)-curves of this device when pumped at 0.64 THz. The LO power needed to pump the device is obtained using an isothermal technique[5] at high bias. Although not completely accurate[6], this technique gives an estimate of the power required to operate the device. Usually, a Nb HEBM is operated with about 50–80 nW of LO power. This device seems

to require 1.5–2 times that power to obtain lowest noise operation. Similar

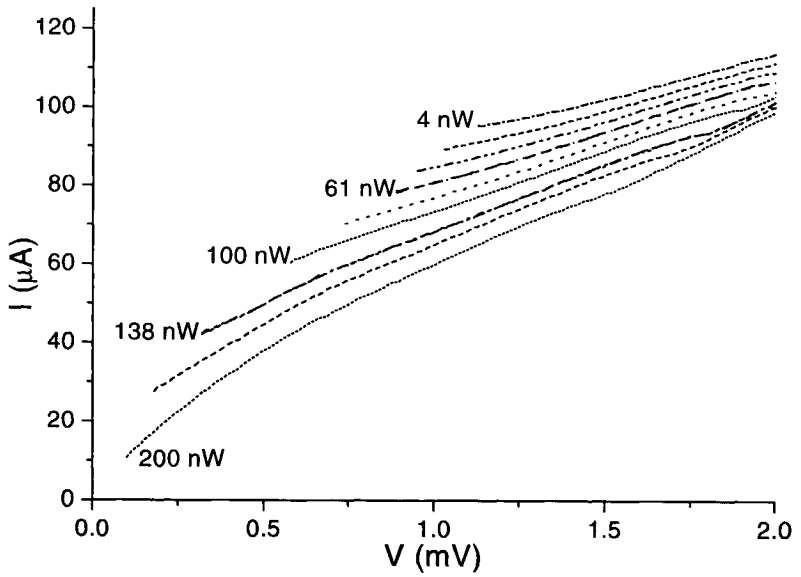

FIGURE 8.4. Several I(V)-curves for different pumping levels corrected for R_{series} (all at 0.64 THz). Indicated P_{LO}-levels are obtained using the isothermal technique[5].

plots have been obtained with pump frequencies of 1.9 and 2.5 THz. About the same amount of LO power is required to pump the device at these two frequencies.

The kink at about 1.7 mV in the I(V)-curve is not typical for HEBMs; it is attributed to the unusual geometry of the nanobridge in the device, and is related to the extra shoulder in the R(T)-curve (Fig. 8.2). We observe that the kink shifts down in bias voltage with increasing P_{LO}. Apparently, the amount of dc power needed to induce the kink decreases when more LO power is present. We speculate on the origin of this in Section 8.4.

TABLE 8.2. Noise and gain of IS 1_4 F3.

f (THz)	Y (dB)	T_{Rec} (K)	T_{Mix} (K)	$G_{Mix}(0)$ (dB)	G_{opt} (dB)	$T_{c,\,eff}$ (K)	$T_{h,\,eff}$ (K)
0.64	0.35	2400	600	-6.5	-6.8	43	88
1.9	0.13	6900	920	-11.8	-7.1	38	80
2.5	0.10	8900	900	-12	-9.0	33	60

8.2.4 Receiver– and mixer sensitivity

Receiver noise temperature measurements are performed on the device using the Y-factor technique described in Section A.2.1. When not indicated differently, the measurements have been done at 0.64 THz using an IF bandpass filter of 80 MHz at about 1.35 GHz, since this combination gives the highest Y-factor (see Fig. 8.6). T_{Rec} is defined as the noise temperature measured, without *any* correction, assuming $T_{hot} = 290$ K and $T_{cold} = 80$ K for the black-bodies at ambient and ℓN_2 temperatures, respectively (see App. A for details on the methods used). When this result is corrected for the loss in the optical path (i.e. in the beam splitter, window, Zitex IR filter, Si lens and for the offset from the maximum response measured at 0.9 THz) and the noise contributed by the IF chain (i.e. the isolator's and amplifier's contributions), we obtain T_{Mix}. It is this value that is intrinsic to the actual nanobridge. When the corrections for the optical components are taken into account, the black bodies with physical temperatures $T_{hot,\,eff} = 290$ K and $T_{cold,\,eff} = 80$ K are found to have radiation temperatures of $T_{hot,\,eff} = 88$ K and $T_{cold,\,eff} = 43$ K. Hence, the noise temperature of the mixer itself, T_{Mix}, is much lower than that of the receiver, T_{Rec}.

Fig. 8.5[b] shows a pumped (thin solid line, frequency = 0.64 THz) and unpumped (thick solid line) I(V)-curve of the device at a bath temperature T_b of 2.8 K together with $P_{IF,h/c}$, the power measured at the IF port when looking at a hot (dotted line) and cold (dashed line) load, respectively. The thick solid line shows P_{IF} with no P_{LO} applied. This data set is the basis for deriving parameters such as the gain and noise temperature of the mixer in the remainder of this Chapter.

From these data, the Y-factor as a function of bias voltage is calculated

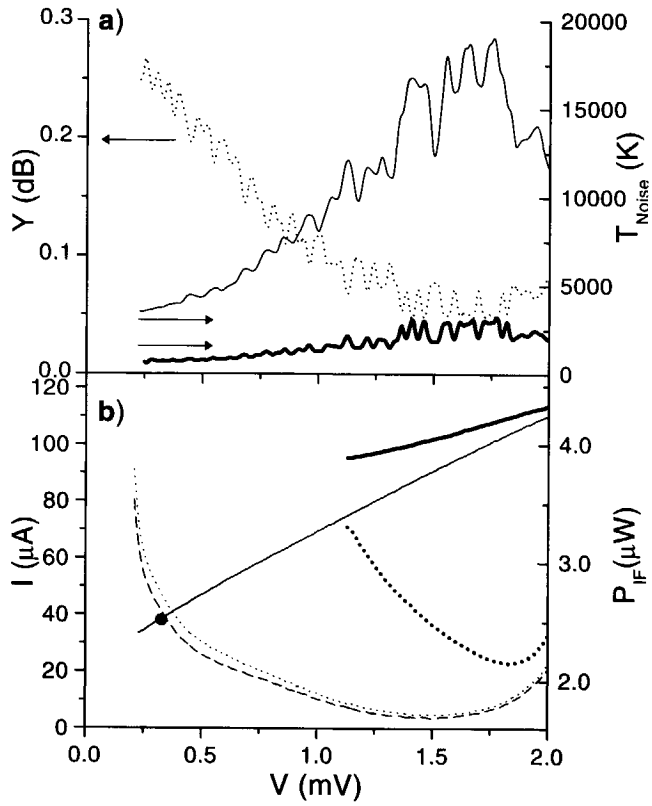

FIGURE 8.5. [a] Y-factor (dotted line) and receiver noise temperature T_{Rec} as function of bias voltage (unchopped measurement, thin solid line). The best noise temperature measured using this device is 2400 K. This datapoint is obtained by a manual hot/cold measurement and therefore not shown in this graph. T_{Mix} (thick solid line) is obtained from T_{Rec} as described in the text. $T_b = 2.8\,K$, $f_{IF} = 1.35\,GHz$. [b] I(V)- and P_{IF}(V)-curves of the device at 2.8 K. The thick solid line is the unpumped I(V)-curve, the thin solid line is the I(V)-curve when pumped at 0.64 THz. $P_{IF,h}$ is indicated by the dotted line, $P_{IF,c}$ by the dashed line. $P_{IF,unp}$ is shown by the thick dashed line. The pump power P_{LO} obtained from the isothermal technique (see Ref. 5) equals 75 nW. The dot indicates the bias condition at which Fig. 8.6 has been measured.

using Eq. (A.5). Fig. 8.5[a] shows the result (dotted) together with the corresponding receiver noise temperature T_{Rec} (thin solid). The best Y-factor measured by introducing a cold piece of Eccosorb close to the beam splitter (referred to as 'a manual hot/cold measurement') is 0.35 dB, corresponding to an uncorrected $T_{Rec} = 2400$ K. When corrected for the beam splitter (15 μm Mylar), this gives 2200 K. The graph also shows T_{Mix} (thick solid), the noise intrinsic to the device. It is obvious that the receiver noise is dominated by optics and IF loss, since the mixer noise is about 5 to 10 times lower than the receiver noise, depending upon frequency.

When operating the mixer, one should be careful to avoid *direct detection*, i.e. a change of the bias point due to a change between the hot and cold loads. In some bias conditions, especially at higher temperatures and close to the so-called drop-back point (the lowest stable voltage in which the device can be operated) direct detection can be observed. In most cases, the effect of direct detection is to change (in our experiments usually: increase) the observed noise temperature of the mixer because of a change in matching to the IF chain, which is due to a change of the bias point. At 0.64 THz, this problem is overcome by using a quartz/Zitex low-pass filter. However, such filtering is not easily available at the higher frequencies. Therefore, part of the measured noise temperature at high frequency is attributed to direct detection.

If we assume that the IF roll-off frequency, f_{3dB}, is higher than the IF chain's cut-off ($f_{3\,dB} \gtrsim 4$ GHz), the Y-factor as a function of IF *within the IF chain's band* should be flat. Therefore, the flatness of the IF chain can be checked by measuring the Y-factor throughout the band. This measurement has been done at 2.8 K in the bias point indicated by the black dot in Fig. 8.5. It turns out that this is close to, but not quite the optimal bias condition, since the maximum Y-factor (0.35 dB) is larger than that measured in Fig. 8.6.

The results of this measurement are shown in Fig. 8.6. The result is a reasonably flat Y-factor, except for three distinct features:

1. A sharp decrease at 1.15 and 1.8 GHz. This is due to the low-noise amplifier (LNA) used. This LNA is built for operation in the 1.2–1.8 GHz band. Outside this band, the amplifier noise starts to dominate the chain, and impedance matching is not guaranteed.

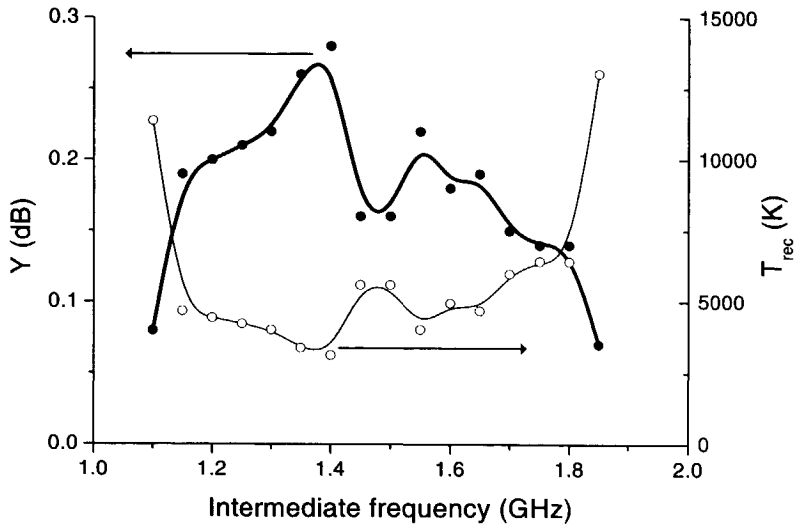

FIGURE 8.6. Y-factor (solid dots) and corresponding T_{Rec} (open dots) vs intermediate frequency (tunable bandpass filter).

2. A peak around 1.35 GHz. This peak is attributed to an improved impedance match at this frequency.

3. A dip around 1.45 GHz. This peak is attributed to a slightly worse match.

Yet another, less pronounced overall feature is visible: a decrease of Y-factor with increasing frequency. This might be due to a frequency dependence intrinsic to the nanobridge (see Section 8.2.7). Although this 300 nm long device is expected to have an IF bandwidth of 3.9 GHz, the measurements reported in Section 8.2.7 show that the actual IF bandwidth of this nanobridge is smaller than that. However, it must be noted that the value of 3.9 GHz is estimated for a fully metallic bridge, i.e. at high bias voltage, whereas this measurement has been done in a near-optimal (low) bias point. This decreases the measured IF bandwidth[6].

TABLE 8.3. Balance of DSB receiver loss at 0.64, 1.9 and 2.5 THz.

	Loss (dB) 0.64 THz	Loss (dB) 1.9 THz	Loss (dB) 2.5 THz
Splitter	0.4	0.5	0.8
Window	1.0	0.7	1.0
Zitex filter	0.1	0.3	0.4
Quartz filter	0.5	—	—
Zitex filter	0.1	0.3	0.4
Lens (reflection)	1.5	1.5	1.5
Lens (absorption)	0.3	0.3	0.3
Antenna offset	2.8	3.5	4.6
Wafer roughness	??	??	??
Total	6.7	7.1	9.0

8.2.5 Gain

The effective black body input power is obtained from its effective temperature and the losses in all elements in front of the mixer using Eq. (A.2), e.g. see Ref 7. $T_{hot,\,eff}$ is reduced from 290 to 88 K, $T_{cold,\,eff}$ from 80 to 43 K.

G_{Rec} can be calculated from the measured $P_{IF,\,h} - P_{IF,\,c}$ using Eq. (A.8). This quantity is plotted in Fig. 8.7, (dotted line). The best value observed for G_{Rec} is -20 dB. The gain drops with increasing bias voltage and flattens out after 1.5 mV. This is due to a change in dV/dI in the device at this bias voltage, improving the matching to the IF chain. This feature is also observed in Fig. 8.5 and attributed to the unusual geometry of the nanobridge.

G_{Mix} is calculated from G_{Rec} by subtracting the losses in the optics (summarized in table 8.3) and the contributions from the IF chain. G_{Mix} is shown in Fig. 8.7 (solid line). At 0.64 THz, the difference between G_{Rec} and G_{Mix} is about -6.7 dB. It should be noted that in this batch a single-sided polished Si wafer has been used. The RMS surface roughness on the non-polished

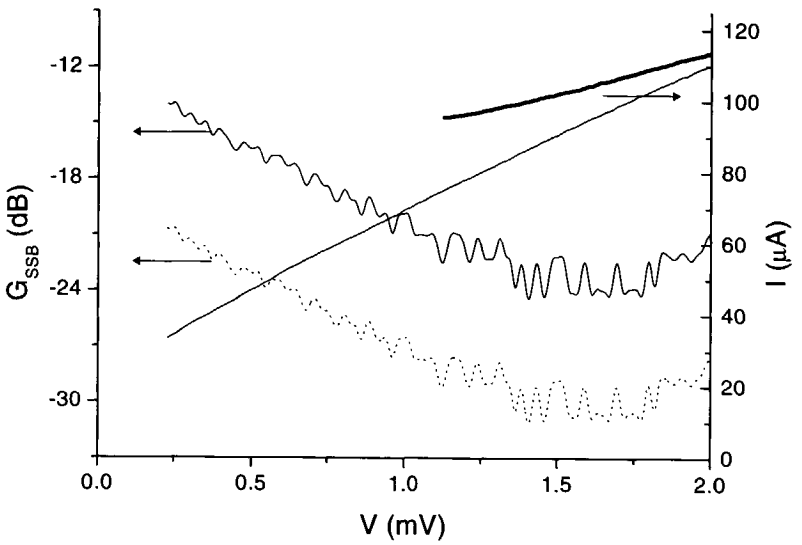

FIGURE 8.7. Receiver gain $G_{Rec,SSB}$ (dotted) and mixer gain $G_{Mix,SSB}$ of the device. The difference between both is due to the optical loss as described in Table 8.3.

side of the wafer roughness is 20 μm. The influence of this on the gain is not known, but it is expected to deteriorate the gain.

From Eq. (A.7) it can be seen that a low G_{Mix} causes T_{Rec} to increase due to the IF– and isolator contribution to the noise. Obviously, in this case it is important to decrease the noise due to the IF chain. Furthermore, it is clear that the gain of the optics is an important parameter in the expression for receiver noise. Optimizing the transmission of the signal path is of prime importance in developing THz receivers.

In table 8.4 we compare the different values for $G_{Mix,SSB}$ and $T_{Mix,DSB}$ observed by several groups. Since these values are measured within the IF band, we have corrected the value for our gain to low-frequency IF by correcting for the 6 dB loss measured in Section 8.2.7. With some exceptions, $T_{Mix,DSB}$ is generally on the order of 500 K. $G_{Mix,SSB}$ is found to be about -6 dB in the lower frequency range, decreasing to -18 dB at 2.5 THz. Some of the spread in the values is caused by the uncertainty in the corrections

TABLE 8.4. Gain and noise in Nb HEBMs

	f (THz)	$G_{Mix,SSB}$ (dB)	$T_{Mix,DSB}$ (K)
This device	0.64	-12.7 (-6.7 low IF)	600 (at low IF)
This device	1.9	-17.8	920 (at low IF)
This device	2.5	-18	900 (at low IF)
Burke[8]	0.02	-5.6	120
Skalare[8]	0.53	-13	560
Ganzevles (ch. 9)	0.65	-17.6	610
Wilms Floet[7]	0.69	-14.3	570
Frommberger[9]	0.80	–	1300
Skalare[8]	1.27	-13	450
Karasik[8]	2.5	-18.5	300

applied in calculating the *mixer* properties from the measured *receiver* parameters. From these data, it seems that the mixer noise in Nb HEBMs can be as low as a few hundred Kelvin.

8.2.6 Output noise

Using Eq. (A.12), T_{out} is derived as a function of bias voltage. This quantity is plotted in Fig. 8.8. T_{out} at the optimal bias voltage is found to be only about 17 K. Values reported in literature are around 50 K (see Ref. 8). The latter are measured within the IF band. To compare our result to that found in Ref. 8, we extrapolate T_{out} to $T_{out}(0)$ using Eq. (A.11). Using the 6 dB reduction from Fig. 8.9, we find that, in this device, the difference between T_{out} and $T_{out}(0)$ is 3.8 dB, $T_{out}(0) = 41$ K. This agrees fairly well with the results found in literature[8]. If T_{out} is dominated by the electron fluctuation noise, the mixer noise temperature is IF-independent, as can be seen from

$$T_{Mix} = \frac{T_{out}}{2G_{Mix}} \approx \frac{T_{out}(0)}{2G(0)}, \tag{8.1}$$

where we have used a result explained in Section 8.2.7.

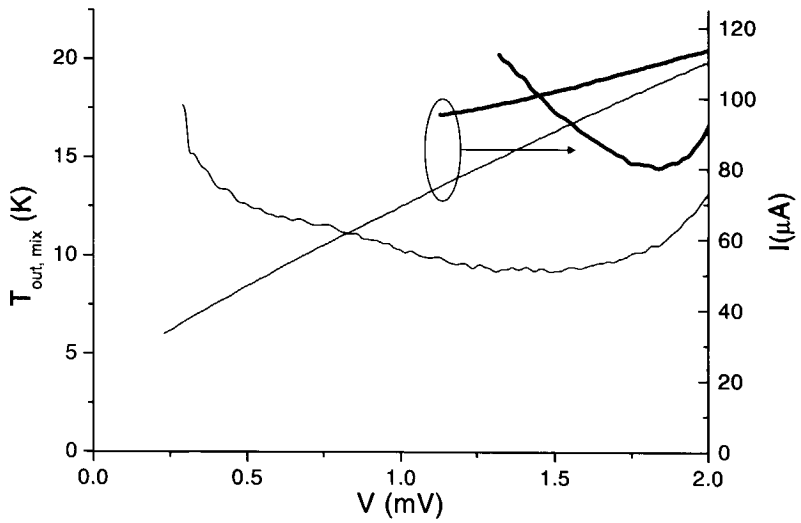

FIGURE 8.8. $T_{out, Mix}$ as a function of bias voltage. The thick solid line is the output noise in the unpumped case, the thin solid line represents $T_{out, Mix}$ in the pumped situation.

At the high IF where we measured T_{Mix}, the Johnson noise is not negligible. Therefore, we convert the observed mixer noise temperature to its dc value, finding a reduction of T_{Mix} by 2 to 3 dB. The value thus obtained is quoted in table 8.4.

8.2.7 IF bandwidth

An important property of a mixer is its IF bandwidth. Especially in bolometer mixers this is a point of concern. Therefore, we describe the measurement of the IF bandwidth in some detail.

Fig. 8.9 shows a measurement of the relative conversion gain vs IF bandwidth. The frequency of the signal is 0.69 THz. Details of the setup are described in Section A.1.3. Care is taken to avoid standing waves in the setup. Fig. A.5 shows the setup used in these experiments. A calibration of the IF chain, not including the the bond wires connecting the device to the IF board, is performed. The correction obtained from this calibration is

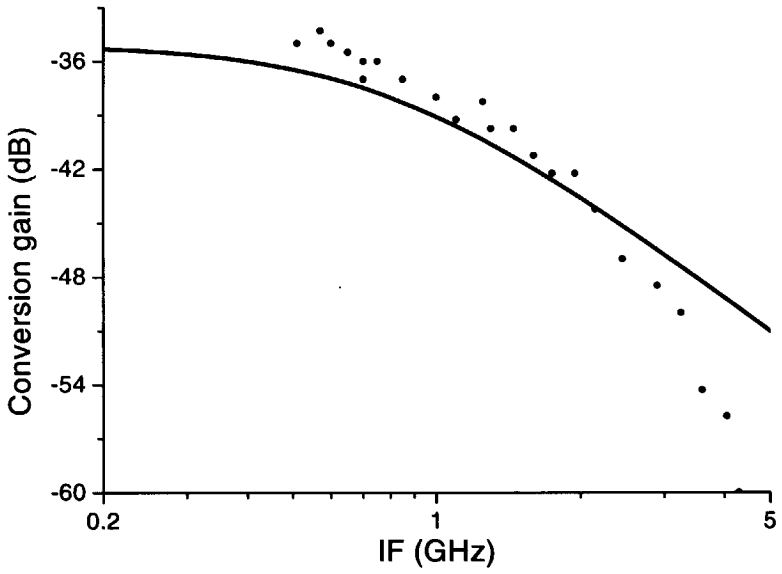

line

FIGURE 8.9. **Relative conversion gain as a function of IF bandwidth. The data are corrected for frequency dependent features in the IF chain down to (but not including) the bond wires.**

applied to the data in Fig. 8.9. Eq. (8.2) gives the expected behavior of the mixer as a function of IF frequency.

$$G_{Mix}(f) = G(0)\frac{1}{1+\left(\frac{f}{f_{3\,dB}}\right)^2}, \tag{8.2}$$

which is a so-called Lorentzian dependence. A fit of Eq. (8.2) to the data gives $f_{3dB} = 0.8 \pm 0.2$ GHz. No data points have been obtained at frequencies lower than 0.5 GHz due to frequency-limitations in the IF chain. This makes it somewhat difficult to obtain an accurate fit to the data points.

In a fully metallic strip the diffusion time τ_{diff} is given by[10,11]

$$\tau_{diff} = \frac{L_b^2}{\pi^2 D}, \tag{8.3}$$

in which L_b is the bridge length, 300 nm in this case. D, the diffusion constant, is determined experimentally for a similar Nb film: $D = 1.6\,cm^2s^{-1}$ with $R_\square = 25\,\Omega$[7]. Extrapolating these values to the film used in this nanobridge, we find $f_{3dB} = 3.9\,GHz$. This value clearly differs from the value measured here. We attribute the low IF bandwidth to the anomalous geometry of the device shown is Fig. 8.1.

Next to the large difference in value, a more striking feature in Fig. 8.9 is the drop-off, which is faster than Lorentzian. Since we have measured several devices having bandwidths larger than 4 GHz and proper Lorentzian roll-offs in this setup (see Ch. 9), the fast roll-off in this device is not due to the setup. We can only speculate for the reason of the fast roll-off: the diffusion process requires large cooling pads at a temperature T_b. In our case, the pads are rather small. This might cause a temperature rise of the pads, effecting the operation of the device. However, following Ref. 12 to find the temperature rise in the pads, we estimate that our cooling pads are well capable of removing the incoming power from the nanobridge without heating up by more than about 10% of the operating temperature. Thus, the origin of the fast IF roll-off remains unclear.

8.3 Analysis and comparison to hot-spot model

The hot-spot model[6] allows one to simulate the pumped and unpumped I(V)-curves and the gain of HEBMs. Applying that model to the data we generate the pumped I(V)– (thick solid) and gain vs voltage-curve (thick dashed) shown in Fig. 8.10. The thin solid line corresponds to the measured pumped I(V)-curve. In the fit, we assume an ideal device with length $L_b = 300\,nm$, width w=175 nm and a thickness of 16 nm. Its T_c equals 6.4 K, T_b is 3 K and $R_\square = 14\,\Omega$ (parameters measured on the Nb film used in this batch). From the fit, we find that 75 nW of LO power is needed to operate the device. This is within a factor of two of the value determined using the isothermal technique. The fit is especially good at the lower bias voltages, but it deviates somewhat at voltages above 1.2 mV. This is attributed to the geometrical anomaly in the bridge. When more power is applied to the device, a part of the bridge —presumably the farthest from the cooling pads— is able to be in a (partial) superconducting state longer than the model predicts. Thus, more current can run through the device, resulting in

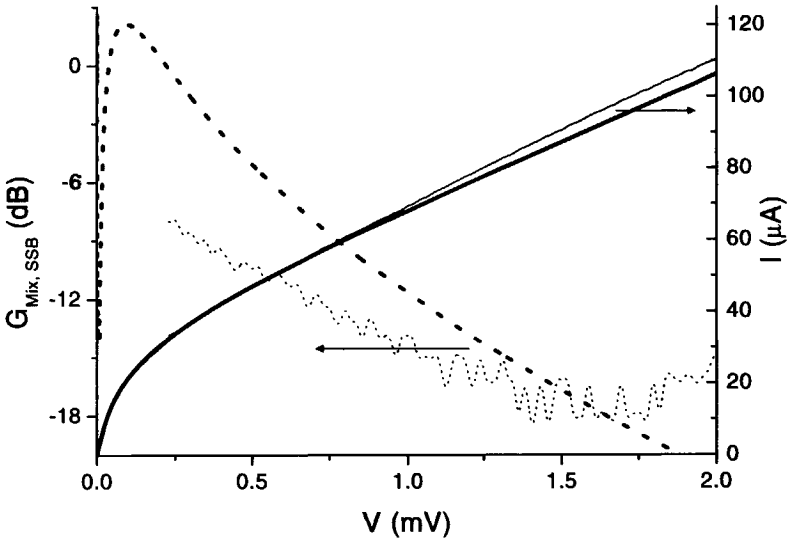

FIGURE 8.10. Measured (thin solid) and simulated (thick solid) I(V)-curve of IS 1.4 F3. $G_{Mix,SSB}$ vs bias voltage. Thick dotted line: simulated gain, thin dotted line: measured gain. The value for G_{Mix} has been obtained from G_{Rec} as described above. Note that G_{Mix} plotted here is corrected for the extra 6 dB loss due to the very small IF bandwidth (Section 8.2.7), so in effect we have plotted $G_{Mix}(0)$.

the deviation observed in the graph.

To be able to compare the measured data to the model, which predicts the dc-limit of the gain, we correct for the 6 dB loss due to the small IF bandwidth in this particular device. When the two gains are compared, it is clear that the model overestimates the gain by about 9 dB[13]. A similarly large difference in gain is also seen in the results of Wilms Floet[7]. Furthermore, in our measured data, the drop of the gain with increasing bias voltage is slower than predicted. We attribute this to the difference between the measured and simulated I(V)-curves. This, in turn, is caused by the unusual device geometry.

8.4 Discussion

The fabrication process used to produce the so-called in situ Nb HEBMs does yield working HEBMs. However, due to the complicated nature of the process its yield is only 5–10%. We also measured several other devices from this batch. However, we have not been able to characterize them as extensively as this one. Therefore, we focus on this device.

The deviations in the behavior of the device compared to a well-defined HEBM are to a large extent understood in terms of the misalignment, as discussed in the above Sections. Based on the hot-spot model, we assume that the hot-spot formed inside this nanobridge does not grow or shrink homogeneously over its width. This has an impact on the voltage dependence of the hotspot length, i.e. the differential resistance. Hints of this are visible in Fig. 8.4, where kinks are visible above 1.5 mV, somewhat dependent on the LO power applied. The change in dV/dI causes a change in impedance matching to the IF chain, resulting in a bump in P_{IF} around 2.0 mV in P_{IF} (Fig. 8.5[b]). This, in turn, results in a feature in parameters deduced from P_{IF} (like T_{out}, $T_{Rec/Mix}$ and $G_{Rec/Mix}$).

The IF bandwidth of this device is smaller than predicted. We attribute this to the geometry of the device. Its length is effectively larger than defined, causing a low IF bandwidth. We do not understand the faster-than-Lorentzian roll-off of the gain vs frequency in this device.

The receiver noise temperatures vs frequency observed in this mixer are shown in Fig. 8.11 (dots). T_{Rec} increases with 3.5 K/GHz. Obviously, these results are not as good as the state-of-the-art performance indicated in the figure (numbers, 1 K/GHz). Those results, however, are taken within the IF band. When an extrapolation of T_{Rec} towards low frequency IF is made for our device, a value around 1200–1500 K is found at 0.64 THz, indicated in Fig. 8.11 (diamonds). These values are consistent with measurements on devices from a similar batch (see Ch. 9). In that case, T_{Rec} increases with 1.8 K/GHz (see Ch. 9).

To be able to compare these results with those measured by other groups, we have applied several corrections to our data. We have done this based on the transmission data available for the components in the optical path and a careful calibration of the IF chain. We believe that these corrections yield parameters that can be directly compared to models and literature values.

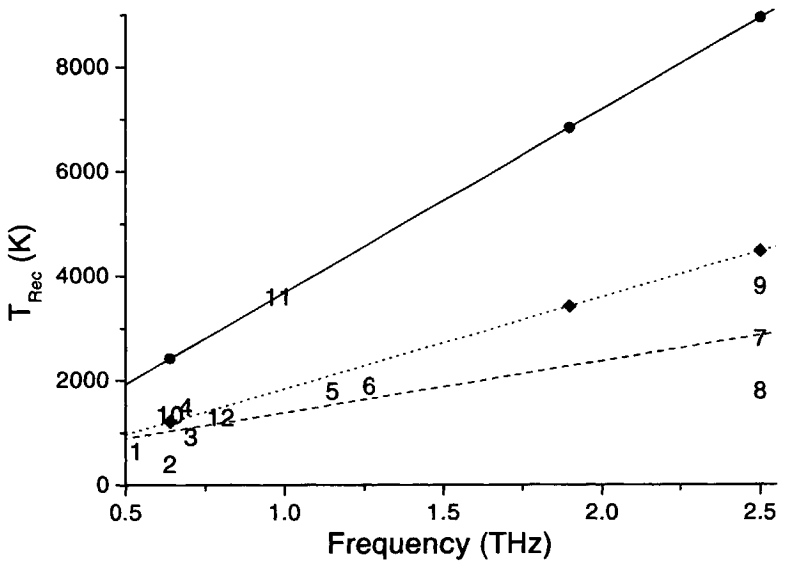

FIGURE 8.11. Overview of the receiver noise temperatures observed in Nb HEBMs. T_{Rec} vs frequency for IS 1_4 F3 (dots). The receiver noise temperature increases with 3.5 K/GHz. When these results are extrapolated to zero IF, the data represented by diamonds are obtained. These values are still somewhat above values found by other groups (numbers act as data points). 1 JPL Nb QO[14]; 2 JPL Nb QO[15]; 3 SRON/TU Delft Nb WG[7]; 4 KOSMA Nb WG[16]; 5 JPL Nb QO[18]; 6 JPL Nb QO[17]; 7 JPL Nb QO[19]; 8 JPL Nb QO[15]; 9 SRON/TU Delft Nb WG[20]; 10 SRON/TU Delft Nb WG[20]; 11 SRON/TU Delft Nb WG[2].

We do realize that the accuracy of the corrections depends largely on the accuracy of the data available.

8.5 Conclusion

We have performed a detailed characterization of a Nb diffusion-cooled HEBM at both dc and rf frequency. Our set of data includes dc measurements, R(T)-behavior, IF– and rf bandwidth, heterodyne noise– and gain measurements and SEM-data on the device geometry.

The critical temperature T_c of the device is typical for the Nb HEBMs

produced in our lab, although the behavior of the R(T)-curve is somewhat odd. An extra shoulder is seen and a normal state resistance of 32 Ω is measured. However, when operating the device in a mixer mode, the measured resistance is 22 Ω. In the lower bias range (up to about 3 mV), the dc I(V)-curve taken at 4.2 K looks normal, too. Its 2nd derivative is positive, hysteresis is observed and $I_c \sim 105\ \mu A$ at 4.2 K. Apparently, one never reaches the bias (or temperature) region where the full bridge is normal, i.e. showing its full 32 Ω. Therefore we assume that the normal state resistance under operating conditions is 22 Ω.

The direct response of the mixer as measured using an FTS shows that it detects power in the 0.3–3 THz range. This makes the log-periodic antenna, as we use it, a suitable wide-band antenna for characterizing the nanobridge.

We have been able to pump the device at frequencies between 0.6 and 2.5 THz. The LO power absorbed by the device is a factor of 2–3 higher than is expected for this type of device. This is largely due to the larger volume of our device. We observe a bump in P_{IF}, both unpumped and in operating condition. This points to a change in in the device impedance, which is caused by the unusual device geometry.

The receiver noise temperature of the system we measure is $T_{Rec} = 2400$, 6800 and 8900 K at 0.64, 1.9 and 2.5 THz, respectively. This T_{Rec} is higher than state-of-the-art. After correcting T_{Rec} for the optics and IF loss, our estimate for T_{Mix} is close to that measured by other groups.

The receiver gain G_{Rec} is -20 dB. Of this, 6.7 dB is due to loss in the optics in front of the nanobridge, thus G_{Mix} amounts to -13.3 dB. This value is similar to that reported by other groups, although it is about 15 dB lower than predicted by the hot-spot model. Even when the measured data are corrected for the low IF bandwidth observed (an additional 6 dB), the model overestimates the gain by 9 dB. The slower than predicted drop of the gain vs bias voltage is believed to be due to the non-homogeneous bridge geometry.

The IF bandwidth is much lower than expected: 0.8 GHz instead of 3.9 GHz. This is caused by a bridge that is effectively much longer than the nominal 300 nm. Also, the drop of the gain vs IF is faster-than-Lorentzian.

From the above it is clear that the exact geometry of the device is of primary importance in this type of device. Not only the length (as was shown earlier[8]), but also the shape of the bridge and the cooling pads dominates its heterodyne properties. Modeling this device is not straightforward.

For practical reasons, it is important to control all geometrical parameters (length, width and alignment) in order to produce a good mixer.

References

[1] Zitex G104, Norton Performance Plastics, Wayne, New Jersey, (201)696-4700.

[2] W.F.M. Ganzevles, J.R. Gao, G. de Lange, D. Wilms Floet, A.K. van Langen, L.R. Swart, T.M. Klapwijk and P.A.J. de Korte, Proc. 10th Int. Symp. Space THz Techn., Charlottesville, VA, March 16–18, pp. 247–260 (1999).

[3] W.F.M. Ganzevles, unpublished data.

[4] P. Yagoubov, M. Kroug, H. Merkel, E. Kollberg, G. Gol'tsman, A. Lipatov, S. Svechnikov, E. Gershenzon, Proc. 9th Int. Symp. Space THz Techn., Pasadena, CA, March 17–19, pp. 131–140 (1999).

[5] H. Ekström, B.S. Karasik, E. Kollberg and K.S. Yngvesson, IEEE Trans. Microwave Theory Techn. **43**, 938 (1995).

[6] D. Wilms Floet, E. Miedema, T.M. Klapwijk and J.R. Gao, Appl. Phys. Lett. **74**, 433 (1999).

[7] D. Wilms Floet, *Hotspot Mixing in THz Niobium Superconducting Hot Electron Bolometer Mixers*, Ph. D. thesis, Delft University of Technology (2001).

[8] P.J. Burke, R.J. Schoelkopf, D.E. Prober, A. Skalare, W.R. McGrath, B. Bumble, and H.G. LeDuc, Appl. Phys. Lett. **68**, 3344 (1996). Values for device parameters are taken from this paper.

[9] M. Frommberger, F. Mattiocco, P. Sabon, M. Schicke, K.F. Schuster, and O. Laborde, Proc. 11th Int. Symp. Space THz Techn., Ann Arbor, MI, May 1–3, pp. 489–500 (2000).

[10] H.S. Carslaw and J.C. Jaeger, *Conduction of Heat in Solids*, Clarendon Press, Oxford (1959).

[11] P.J. Burke, *High Frequency Electron Dynamics in Thin Film Superconductors and Applications to Fast Sensitive THz Detectors*, Ph. D. thesis, Yale University (1997).

[12] A.D. Semenov and G. Gol'tsman, J. Appl. Phys. **87**, 502 (2000).

[13] It is not clear to us why the modeled gain is larger than 0. For positive dV/dI, one expects a maximum gain of -6 dB.

[14] A. Skalare, W.R. McGrath, B. Bumble, H.G. LeDuc, P.J. Burke, A.A. Verheijen, R.J. Schoelkopf and D.E. Prober, Appl. Phys. Lett. **68**, 1558 (1996).

[15] R.A. Wyss, B.S. Karasik, W.R. McGrath, B. Bumble, H.G LeDuc, Proc. 10^{th} Int. Symp. Space THz Techn., Charlottesville, VA, March 16–18, pp. 215–228 (1999).

[16] K. Fiegle, D. Diehl and K. Jakobs, IEEE Trans. on Appl. Supercond. **7**, pp. 3552–3555 (1997).

[17] A. Skalare, W.R. McGrath, B. Bumble, H.G. LeDuc, IEEE Trans. on Appl. Supercond. **7**, 3568 (1997).

[18] A. Skalare, W.R. McGrath, B. Bumble, H.G. LeDuc, Proc. 9^{th} Int. Symp. Space THz Techn., Pasadena, CA, March 17–19, pp. 115–120 (1998).

[19] B.S. Karasik, M.C. Gaidis, W.R. McGrath, B. Bumble and H.G. LeDuc, IEEE Trans. on Appl. Supercond. **7**, 3580 (1997).

[20] W.F.M. Ganzevles, this work.

[21] M. Frommberger, F. Mattiocco, P. Sabon, M. Schicke and K.F. Schuster, Proc. 11^{th} Int. Symp. Space THz Techn., Ann Arbor MI, May 1-3, pp. 489-500 (2000).

Chapter 9

Heterodyne measurements on a twin-slot HEBM at 0.7 THz

In this Chapter we report the results of direct and heterodyne measurements on several devices from the IS 1_2 batch. This batch is produced using the in situ-process described in Ch. 5. We show that this way of producing HEBMs yields devices that exhibit near-state-of-the-art performance in terms of noise, gain and IF bandwidth.

The Chapter is organized as follows: first, we describe the device geometry, dc properties and its direct response as a function of frequency. Then, its heterodyne sensitivity and gain are reported. Next, the IF bandwidth is determined. Finally, a discussion and conclusions are presented.

9.1 Device geometry

Although similar results have been obtained on several devices, we focus on one device in particular. This device employs a twin-slot antenna designed for 0.7 THz. The design is made using the concepts outlined in Ch. 4. The important device parameters are summarized in Table 9.1.

The critical temperature T_c of a Nb nanobridge with thickness t=14 nm taken from the same batch is 7.4 K. T_c of the Nb under the Au cooling pads (110 nm thick) is 6.2 K, thus the difference between the two T_c's amounts to 1.2 K. This value is nearly the largest observed in our Nb HEBMs, indicating a high transmissivity of the Nb/Au interface. The critical current I_c is 160 μA at 4.2 K, increasing to 260 μA at 3.2 K. Its normal state resistance

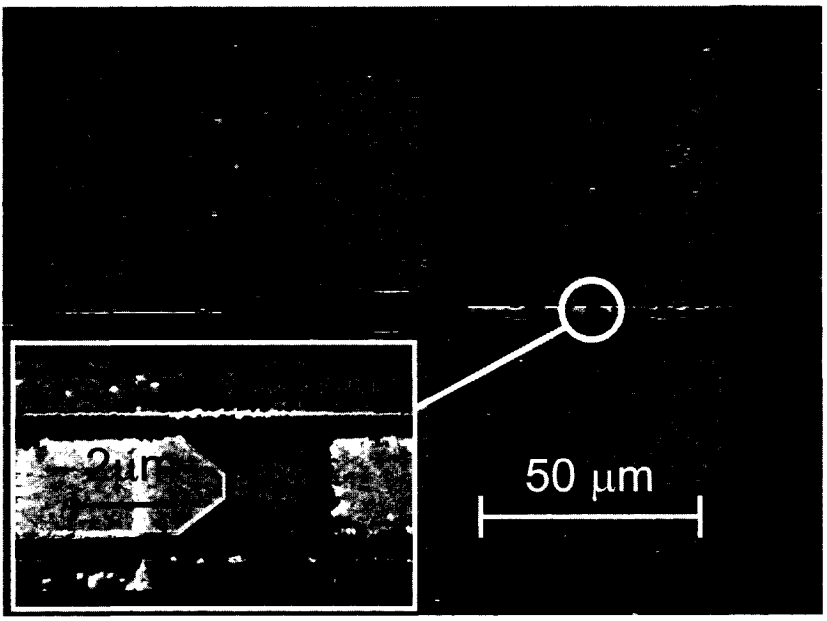

FIGURE 9.1. SEM picture of a device similar to IS 1_2 G4. Nominal dimensions are similar. The inset shows a zoom of the CPW/bridge area.

R_N is 40 Ω, its series resistance R_{series} is 7 Ω. The relatively high value of R_{series} is due to the filter: the filter sections are $\lambda/4$ in length, while the width is kept nearly the same. Therefore, the resistance of the sections increases with decreasing frequency. No SEM micrograph of this particular device is available. Fig. 9.1 shows a sister-device, of which the nominal geometry is the same. The high value measured for R_N is unexpected. Based on the nominal geometry and square resistance measured in a larger structure (hundreds of µms), around 12 Ω is expected. We suspect that the deviation from the nominal value is due to over-etching when defining the Nb nanobridge. This causes the bridge to be smaller than defined, increasing R_N.

TABLE 9.1. Geometry of device IS 1_2 G4. L, w and s are the antenna slot length, width and separation, respectively. a and b are the slot– and center line width in CPW transmission lines. $Z_{hi,\,low}$ are filter sections having high and low impedance.

f_c	0.70 THz
Antenna	twin slot, L = 137 μm, w = 6.9 μm, s = 68.5 μm
	metal thickness: 300 nm.
CPW line	a = 1.2 μm, b = 2.0 μm,
Filter	Z_{low}: a = 1.2 μm, b = 6.6 μm, Z_{hi}: a = 3.9 μm, b = 1.2 μm
Nanobridge	length = 200 nm, width = 250 nm
Resistance:	$R_{300\,K} = 104\,\Omega$, $R_{10\,K} = 40\,\Omega$, $R_{4\,K} = 7\,\Omega$
Substrate	Si, 300 μm, $\epsilon_r = 11.7$, one-sided polished

9.2 Direct response of device IS 1_2 G4

Using the model outlined in Ch. 4, we predict the FTS response for this specific device. This simulation is shown in Fig. 9.2 (thin line). This curve includes the effect of all optics. The measured curve is shown as a thick solid line. The measurement includes the effect of all optics in the signal path, so both curves can be compared directly. In general, the agreement between the two is good. Table 9.2 summarizes the main results from this experiment. The model predicts shoulders next to the main peak that could not be observed in the measurement. A low-frequency resonance is present on both simulation and measurement. The measured bandwidth B_{meas} is 30% smaller than the predicted bandwidth B_{sim}. The origin of this effect is not clear. It is worthwhile to mention that the agreement between the measured and simulated direct response has been found to be even better in other samples of this batch. A bandwidth $B_{meas} = 340$ GHz has been observed.

Resonances with a period of 63 GHz are observed in the direct response. Similar resonances are seen in both waveguide- and QO- superconductor-insulator-superconductor (SIS[1])- and HEBM devices. Therefore, they are not related to rf features within the device, but rather to the FTS setup

TABLE 9.2. Bandwidth and center frequency of IS1_2 G4.

	Simulated	Measured
f_c (GHz)	619	620
B (GHz)	382	280

itself. Contrary to what has been reported in literature[2], the resonance does not correspond to modes in the substrate. Most likely, they are due to standing waves in the quartz of the Hg-lamp, which –based on the resonance– is predicted to be about 850 μm thick. This is believed to be a realistic value for the thickness of this type of lamp bulbs.

9.3 Heterodyne sensitivity

The sensitivity of the device is measured using the Y-factor technique (see Section A.2.1). To do this, we made use of the setup shown in Fig. A.3. All measurements are taken at 1.5 GHz IF. We used a Mylar beam splitter with a thickness of 15 μm to couple the LO into the mixer.

Systematic measurements are shown in Fig. 9.3. Fig. 9.3[b] shows I(V)-curves for several values of P_{LO} taken at a bath temperature T_{bath} of 4.2 K.

It is not possible to bias the device stably in the area of the I(V)-curve with a negative dV/dI. The I(V)-datapoints in this region are averaged by the bias- and monitoring system. No heterodyne measurements are performed there.

At a bath temperature of 4.2 K, a best manual Y-factor of 0.5 dB has been observed. Fig. 9.3[a] shows the Y-factor (thin lines) and T_{Rec} (thick lines) vs bias voltage. These correspond to the I(V)-curves in the lower panel of Fig. 9.3.

Upon increasing the P_{LO}-level while keeping the bias voltage constant, one first observes an increase in Y-factor. After a certain optimal P_{LO}-level (fourth I(V)-curve from top) has been exceeded, the Y-factor curves shift downward again. This behavior clearly shows the existence of a region in

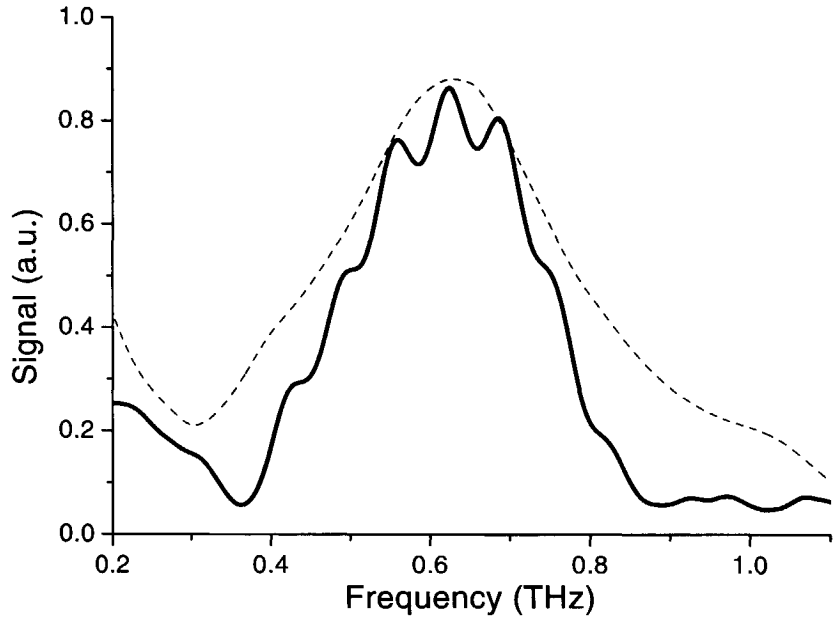

FIGURE 9.2. Measured (thick) and simulated (thin) direct response of the device. The device is designed for 0.70 THz.

pumped I(V)-curves where the mixer has the lowest noise. The P_{LO}-level needed to operate the mixer with lowest noise is estimated to be 30 nW.

Fig. 9.4[b] shows several I(V)-curves for different LO powers taken at 3.2 K. The top panel contains the corresponding curves showing Y-factor and T_{Rec}. At 3.2 K, the highest manual Y-factor is 0.65 dB. Notice that the LO source/splitter combination is not quite powerful enough to fully pump the device. However, we can reach the optimal LO power region, as is seen from the behavior of the Y-factor for several P_{LO}s.

Table 9.3 shows the Y-factor, T_{Rec} and T_{Mix} at 4.2 and 3.2 K. $T_{Rec,BS}$ and $T_{Rec,BS,wind}$ are the noise temperature corrected for the beam splitter (15 μm Mylar) and splitter plus window (40 μm Mylar), respectively, measured at 4.2 K and 3.2 K. In T_{Mix} the influence of the IF chain and the rest of the optics is removed, too.

The noise temperature decreases by about 26% upon decreasing the tem-

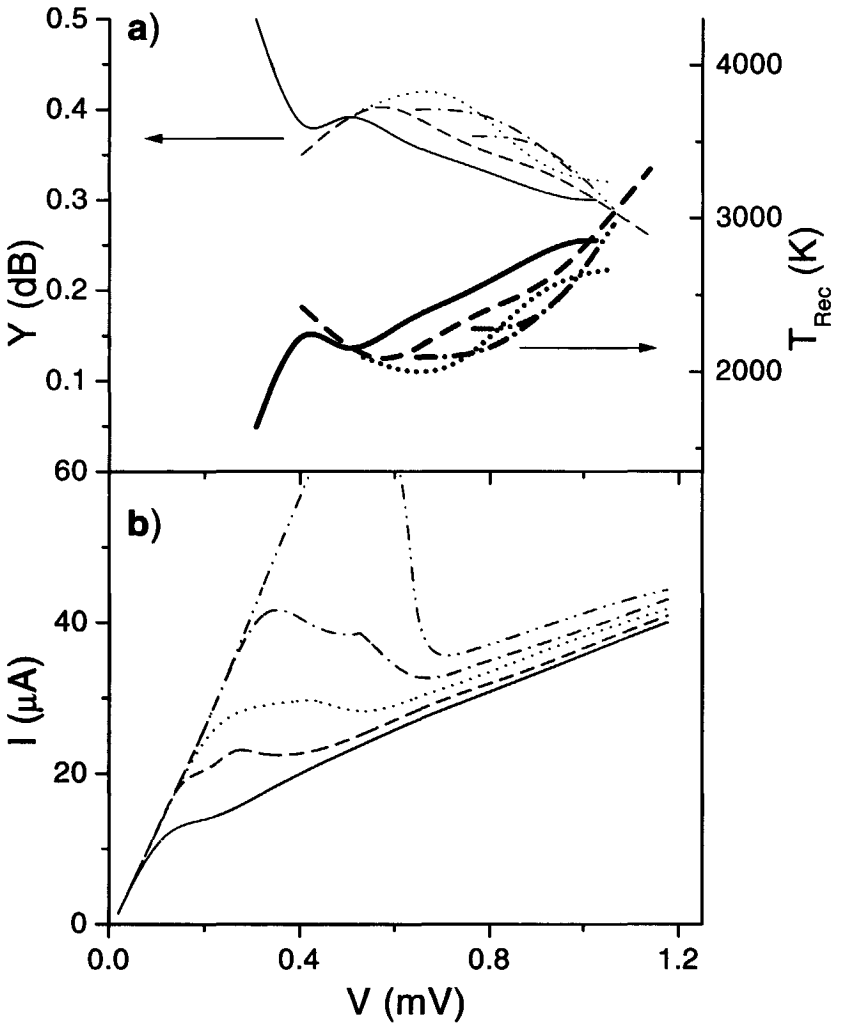

FIGURE 9.3. [a] Y-factor (thin lines) and T_{Rec} (thick lines) vs bias voltage for device IS 1_2 G4 for several P_{LO}'s at 0.64 THz. This device is designed for 0.70 THz. [b] I(V)-curve of this device for several P_{LO}. These data are taken at 4.2 K.

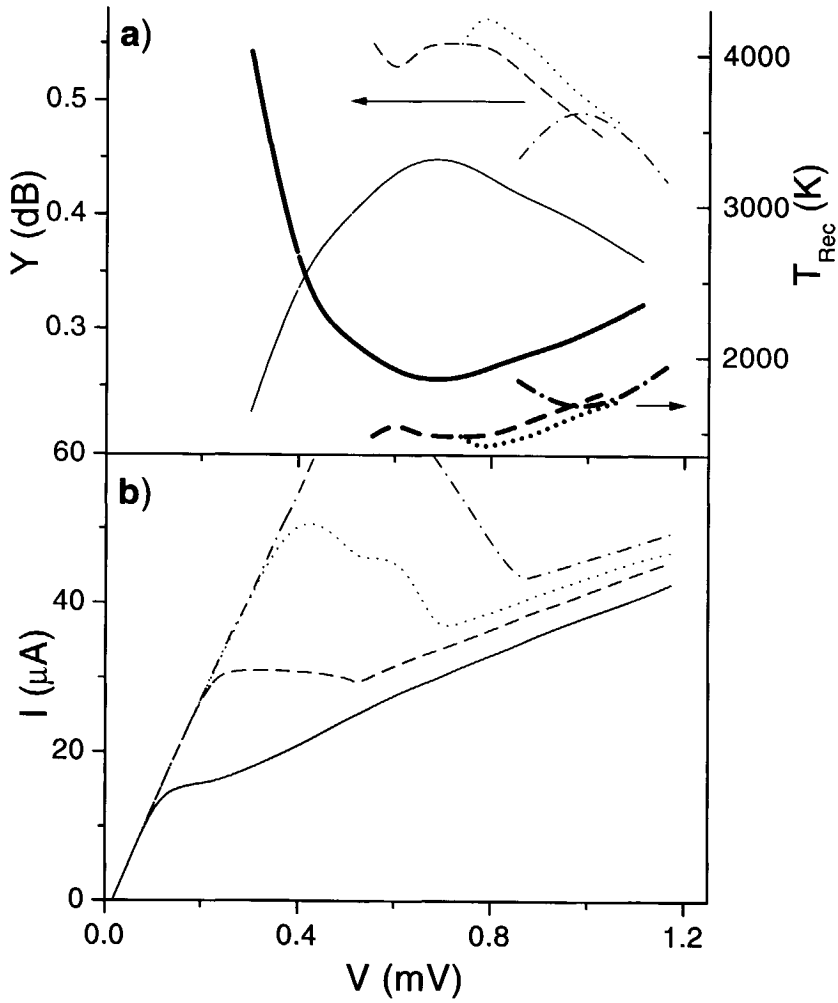

FIGURE 9.4. [a] Y-factor (thin lines) and T_{Rec} (thick lines) vs bias voltage for device IS 1_2 G4 for several P_{LO} at 0.64 THz. This device is designed for 0.70 THz. [b] I(V)-curve of this device for several P_{LO}. These data are taken at 3.2 K.

TABLE 9.3. Receiver- and mixer noise temperature of IS 1_2 G4 at 0.64 THz.

	4.2 K	3.2 K	Decrease with T (%)
Y (dB)	0.50	0.65	
T_{Rec} (K)	1600	1200	26
$T_{Rec,BS}$ (K)	1500	1100	26
$T_{Rec,BS,wind}$ (K)	1100	810	26
T_{Mix} (K)	610	470 (est.)	23

perature of the bolometer. Part of this reduction can be attributed to the lower noise coming from the background (lens, IF chain), but the main contribution to this, some 23%, is due to the decrease in mixer noise. Since the mixer noise is given by

$$T_{Mix} = \frac{T_{out}}{G_{Mix}}, \tag{9.1}$$

this decrease can be due to an increase in the mixer gain G_{Mix} or a decrease in the output noise temperature $T_{out} = T_{EFN} + T_J$. When T_{out} (which can be measured) remains constant upon lowering T_b, it is G that is increased The Johnson noise temperature T_J is given by the average temperature inside the bridge. For simplicity, this value is assumed to be T_c of the nanobridge, which is a fixed value. The electron fluctuation noise temperature T_{EFN} decreases with decreasing temperature. Therefore, one expects T_{out} to decrease when lowering T_{bath}. We do not have enough data to conclude on a change in G_{mix} upon decreasing the bath temperature.

9.4 Gain

The IF output power of the device has been measured by looking at a hot/cold load. We use these data to determine the receiver gain in different bias points and for different LO power. We determine the maximum gain of the receiver employing this device to be -20 dB. Using Table 9.4, we

TABLE 9.4. Balance of DSB receiver loss at 0.64 THz. Antenna offset is the decrease in coupling w.r.t. maximum (measured) signal.

	Loss (dB)
Splitter	0.4
Window	1.0
Zitex filter	0.1
Zitex filter	0.1
Lens (reflection)	1.5
Lens (absorption)	0.3
Antenna offset	0.2
Total	3.6

find G_{Mix} to be -16 dB. We are not able to calculate the gain at 3.2 K as we do not have the IF ouput power available.

When we calculate the mixer gain predicted by the hot spot model[3], we find a best mixer gain of -12.3 dB. This agrees reasonably well with the measured best mixer gain of -16 dB. These values compare reasonably well to those observed by other groups (see Ch. 8 of this thesis for a comparison). However, this is not always the case when G_{Mix} of a device is measured.

9.5 IF bandwidth

The IF bandwidth of an HEBM is an important practical parameter (see Section 2.4.2). In this Section, we report on measurements of the IF bandwidth of device IS 1_2 G4, fabricated using the *in situ* process.

According to the model by Wilms Floet *et al.*[4], the IF bandwidth depends on the length of the normal region within the bridge, i.e. on the bias voltage. Therefore, we have measured the gain bandwidth in a bias point where the noise is minimized (low V) and in a point where a large fraction of the bridge is normal (high V). In the operating point (low V), the value of $f_{3\,dB}$ is not

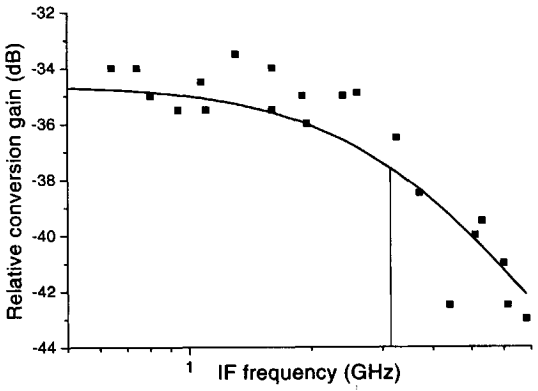

FIGURE 9.5. IF bandwidth of a a 200 nm long Nb HEBM measured in the optimal bias point. The one-pole fit gives a roll-off frequency of $f_{3dB} = 3.2$ GHz. The data have been corrected for the IF chain.

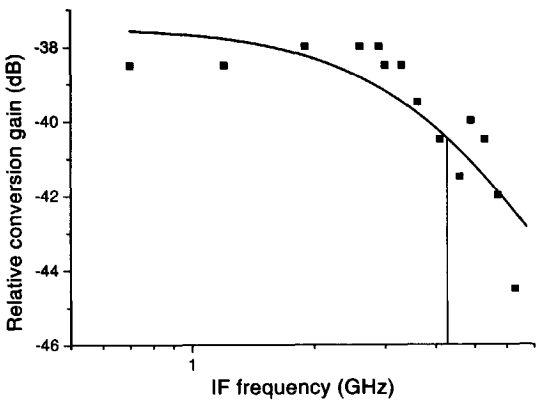

FIGURE 9.6. IF bandwidth of a 200 nm long Nb HEBM measured in a high bias point. The one-pole fit gives a roll-off frequency of $f_{3dB} = 4.3$ GHz. The data have been corrected for the IF chain.

easily determined, since it depends, among other things, on the length of the superconducting ends and their thermal conductivity. To compare with theory, we also measure the bandwidth at high bias voltage.

Fig. 9.5 shows the relative conversion gain of this mixer in the optimal bias point, i.e. the operating point in which the Y-factor is maximized: $V_{bias} = 0.65\,mV$, $I_{bias} = 30\,\mu A$. A Lorentzian fit (cf. Eq. (8.2)) shows a gain bandwidth of 3.2 GHz. In these measurements, care is taken to keep the LO power constant. This is done by keeping the current through the device constant to better than $1\,\mu A$ using a polarizer in the LO path. Several devices from IS 1_2 are measured. They show similar IF bandwidth, about 4-5 GHz at high bias voltage.

Fig. 9.6 shows the mixer conversion gain of the same device in a high-voltage bias point (about 3 mV, not visible in Fig. 9.3). This situation is most comparable to a fully metallic strip. In such a system, the diffusion time τ_{diff} is given by [5,6]

$$\tau_{diff} = \frac{L_b^2}{\pi^2 D}, \tag{9.2}$$

in which L_b is the bridge length, in this case 200 nm. D, the diffusion constant, is determined experimentally on a similar Nb film[7]. Since, according to the Einstein relation[8], D depends on the readily measured resistivity ρ, we calculate D for our film using the values for ρ and D measured by Wilms Floet and ρ obtained from in our film. We obtain $D = 2.1 \cdot 10^{-4}\,m^2 s^{-1}$ with $\rho = 2.1 \cdot 10^{-7}\,\Omega cm$. Using these values, we find $f_{3\,dB} = 8.3\,GHz$. This is fairly far from the experimentally observed value.

9.6 Discussion

The receiver noise temperature measured in these devices is the lowest we have seen in our mixers: 1200 K at 3.2 K. This is about 35% higher than the best value measured by Wilms Floet at a similar frequency, which is considered state-of-the-art performance in Nb HEBMs. A large fraction of this noise is due to the optics in front of the actual mixer. First, at lower frequency, a waveguide is generally believed to be a better coupling system than a quasi-optical system. More specific, our Si lens did not have any anti-reflection coating. This gives rise to a 1.5 dB loss due to reflections from

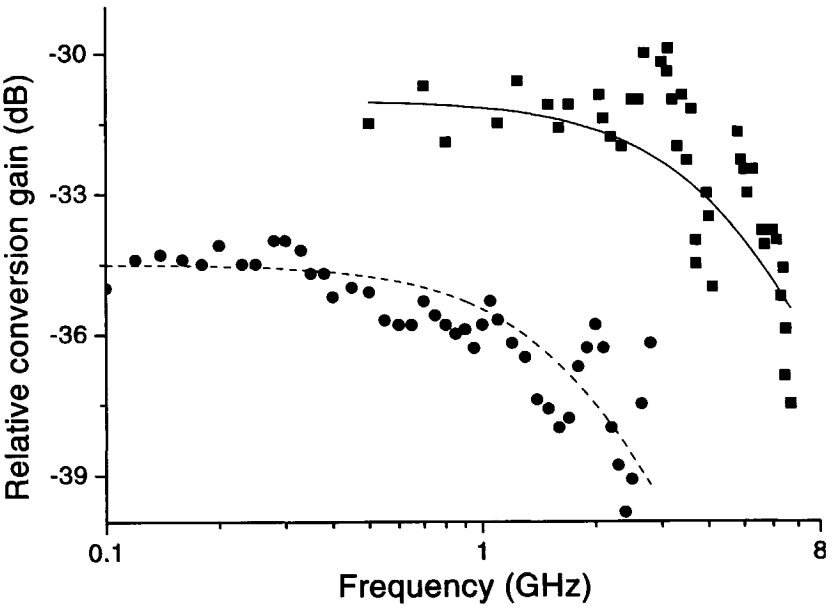

FIGURE 9.7. The relative gain bandwidth measured on an ex situ-device from batch ES 2_2 (dots) and in situ (IS 1_2 B9) (squares) device. Both devices show the highest IF bandwidth measured at high bias voltage in the two fabrication processes. The nominal device length is the same in both devices. A one-pole fit to the data yields $f_{3\,dB\,ES} = 2.0$ GHz and $f_{3\,dB\,IS} = 5.0$ GHz, respectively.

the lens surface. Secondly, our dewar window is optimized for 2.5 THz. An improvement of about 0.4 dB can be made in optimizing the dewar window for 0.7 THz. This particular batch is produced on single-sided polished Si. The backside has an RMS roughness of about 20 μm, a considerable fraction of the wavelength. This is believed to give rise to scattering and mismatch, increase T_{Rec} by an unknown amount. Polishing the back side should decrease T_{Rec}. Together, these improvements are expected to yield a receiver noise temperature below 800 K.

The IF bandwidth measured in this batch is fairly far from that predicted by the metallic bridge-approximation. We see three possible causes for this observation. One is the fact that in the simulation one assumes a

fully metallic bridge, whereas in the measurement at 3 mV, the bridge is not quite normal yet. Another reason might be that ρ and/or D measured in a large film does not necessarily correspond to that measured in a nanobridge. Due to fabrication processes or size effects, these values may differ, inhibiting a proper comparison. Thirdly, the value for D in our films has been extrapolated from that observed in another film. It is not certain to what extent this extrapolation is accurate.

Fig. 9.7 shows a measurement of the IF bandwidth measured on an ex situ device (ES, dots) and an in situ device (IS, squares) and a one-pole fit to the data. Both devices have the same length and D and both measurements have been performed at high bias voltage. $f_{3\,dB}$ measured on the ES device is 2.0 GHz, the IS device has $f_{3\,dB}$=5.0 GHz. The large difference is attributed to the difference in interface transparency and quality of the Nb under the cooling pads in these devices and, therefore, directly to the production process, see Ch. 5. Similar bandwidth (and higher for shorter devices) has been observed by Wyss *et al.*[2], using a fabrication process similar to our in situ-process.

It is worthwhile to mention that Wilms Floet[7] measured the IF bandwidth of a device with length L=300 nm fabricated using the ex situ-process. $f_{3\,dB}$ of this device equals 2.5 GHz in a bias point that does not yet drive the bridge fully metallic. This differs from the observations we have done. Possibly, D and/or ρ of a nanobridge differs from that of a large film on which D and ρ have been determined experimentally.

In NbN devices, cooling relies on a fast electron-phonon interaction rate. The hot phonons then deliver their energy to the substrate. The latter process is the bottleneck in NbN devices. The chance of phonon escape to the substrate can be increased by making the NbN film thin, on the order of 3-5 nm. This increases the number of interactions between the phonon and the substrate. In this way, experimental bandwidths up to 3-4 GHz have been measured on a Si substrate. Based on the electron-phonon coupling rate between film and substrate, an upper limit of 10 GHz is expected. In an effort to reach this upper limit, Yagoubov *et al.*[9] have used MgO substrates to improve the phonon escape to the substrate. They have measured a bandwith of 4.6 GHz in this type of device.

9.7 Conclusion

Batch IS 1_2 contains several devices with desirable dc properties. The device we focus on in this Chapter has $T_{c,\,bridge} = 7.4\,K$, $T_{c,\,pads} = 6.2\,K$. Its R_N equals $40\,\Omega$, R_{series} is $7\,\Omega$.

The FTS spectrum of several devices can be modeled well using the design model described in Ch. 4.

Heterodyne measurements on an in situ device have shown a rather high sensitivity at 0.64 THz: T_{Rec} is 1600 K at 4.2 K, decreasing to 1200 at 3.2 K. This is about 25% higher than the s.o.a.p.-performance in Nb HEBMs at this frequency. The mixer noise temperature T_{Mix} is somewhat higher than that measured by others[7,10]. It decreases with temperature. G_{Mix} of the device is some 5 dB lower than that measured by others, about -17 dB. In lowest-noise operating conditions, some 30 nW of LO power is needed to pump the device. This value is very close to that reported in literature.

The IF bandwidth of the devices in this batch is high, up to 5 GHz at high bias voltage. A comparison between the ex situ and in situ fabrication process shows that the highest bandwidth is observed in the in situ-process. We relate this to the transparency of the interface obtained using an in situ fabricated Nb/Au bilayer.

References

[1] B.D. Jackson, private communication.

[2] R.A. Wyss, B.S. Karasik, W.R. McGrath, B. Bumble and H. LeDuc, Proc. 10th Int. Symp. Space THz Techn., Charlottesville, March 16-18, pp. 215-228 (1999).

[3] D. Wilms Floet, E. Miedema, T.M. Klapwijk and J.R. Gao, Appl. Phys. Lett. **74**, 433 (1999).

[4] D. Wilms Floet, T.M. Klapwijk, J.R. Gao and P.A.J. de Korte, Appl. Phys. Lett. **77**, 1719 (2000).

[5] H.S. Carslaw and J.C. Jaeger, *Conduction of Heat in Solids*, Clarendon Press, Oxford (1959).

[6] P.J. Burke, R.J. Schoelkopf, D.E. Prober, A. Skalare, W.R. McGrath, B. Bumble and H.G. LeDuc, Appl. Phys. Lett. **68**, 3344 (1996).

[7] D. Wilms Floet, *Hotspot Mixing in THz Niobium Superconducting Hot*

Electron Bolometer Mixers, Ph. D. thesis, Delft University of Technology (2001).

[8] E.g., see N.W. Ashcroft and N.D. Mermin, *Solid State Physics*, Harcourt Brace College Publishers, Fort Worth, ISBN 0-03-083993-9.

[9] P. Yagoubov, M. Kroug, H. Merkel, E. Kollberg, J. Schubert, H.-W. Hübers, S. Svechnikov, B. Voronov, G. Gol'tsman and Z. Wang, Proc. Europ. Conf. on Appl. Superconductivity (EUCAS '99), Barcelona, September 14-17 (1999) and S. Cherednichenko, M. Kroug, P. Yagoubov, H. Merkel, E. Kollberg, K.S. Yngvesson, B. Voronov and G. Gol'tsman, Proc. 11^{th} Int. Symp. Space THz Techn., Ann Arbor, MI, May 1-3, pp. 219-227 (2000).

[10] P.J. Burke, R.J. Schoelkopf, D.E. Prober, A. Skalare, W.R. McGrath, B. Bumble, and H.G. LeDuc, Appl. Phys. Lett. **68**, 3344 (1996).

Chapter 10

Conclusions and outlook

Conclusions

In this thesis, we report the design, fabrication, measurements and analysis of several types of quasi-optically coupled hot-electron bolometer mixers.

We describe two of the designs we have focused on in this work: coplanar waveguide– and microstrip line-coupled HEBMs based on twin-slot antennas. The latter type is a novel design in the field of HEBMs, the former type of device has been described in literature, but had not been studied in detail before. We simulate the direct response of both types of rf structures to find a good design to be realized in practice. Although the log-periodic and spiral antenna are used as well in this work, we do not give any detailed analysis on their design or direct response. These have not been systematically evaluated since their properties are not favorable for use in practical receivers.

All designs are realized in practice using techniques borrowed from semiconductor industry, like nano– and microlithography. The mixers are produced following three different fabrication routes. One is intended for microstrip line coupled devices and is based on NUV lithography (except, of course, for the nanobridge). This recipe turns out to depend critically on the step coverage used to connect the top wiring to the ground plane. The two other recipes are used to produce CPW-based devices. The ex situ production of the Nb/Au interface in the bridge, using PMMA as an etch mask, is simplest. Heterodyne results obtained with this type of device are less good compared to those obtained based on an in situ-process, which is a

more difficult process. This route also shows a low yield. All three processes yield devices that show dc I(V)– and R(T)-curves which are understood qualitatively.

The direct response as a function of frequency of both types of devices is predicted based on a relatively simple model. We determine the value of the impedance of each element and then we combine them into an effective impedance seen at the position of the nanobridge. The results obtained using this method agree reasonably well with the direct response measured in an FTS. Measurements show that f_{center} is lower than predicted. The difference in peak frequency observed between the measured and simulated data is explained by an inductance in the bridge, which is believed due to the squeezing of the rf current from the relatively wide center conductor into the narrow nanobridge. It has become clear that this inductance cannot be ignored in the design as we did initially.

For the CPW-coupled HEBMs, this method is compared to a more sophisticated Method-of-Moments-approach using commercial software. Both predictions agree well. The MoM-approach is more time-consuming and less suitable for device optimization, but gives more detailed features in the spectrum. A comparison of data from these models to measured data shows a downshift in f_c. A similar downshift is observed in devices based on microstrip line transmission lines. Since the nanobridge is the only comparable feature in both types of devices, this is an indication that the squeezing could cause this reduction of f_c.

Heterodyne measurements have been performed on all types of devices. A device produced using the in situ-process has shown $T_{N,rec} = 1200\,K$ at 0.64 THz, which is within a factor of 2 of the best yet reported. At 2.5 THz, both a CPW– and a microstrip line coupled device have shown a $T_{N,rec} = 4100\,K$. Again, these values are within a factor of 2 of the best yet reported for diffusion-cooled HEBMs. A log-periodic antenna-coupled device from a similar batch shows 6800 K at 1.9 THz. In these experiments, we have shown that our mixers can be pumped with only little LO power: 30–100 nW is enough to reach highest sensitivity. A 200 nm long device from an in situ batch was measured to have an IF bandwidth of 5.0 GHz, which is to be compared to 8.3 GHz as predicted theoretically.

An in situ-device is characterized in detail. Its R(T), dc– and rf I(V), G(V), $P_{IF}(V)$, IF bandwidth, T_N and geometry are determined. Unfor-

tunately, this device suffers from a flaw in production and therefore, the measured parameters are not optimal. Another in situ-device has shown a high IF bandwidth and good noise properties, though its gain is lower than expected from the hot spot-model. This device shows that we can produce near-state-of-the-art HEBMs using an in situ-process. Further work is needed to improve the yield of this process, so that systematic measurements can be performed and the hot-spot model can be fine-tuned to describe all relevant parameters in superconducting HEBMs.

A comparison between HEBMs coupled via a twin-slot antenna or a spiral antenna shows that $T_{N,rec}$ of the former is a factor of two lower than that of the latter, while the properties of the mixing element are similar, indicating that twin-slot antennas are better suitable for use with Nb HEBMs.

Comparing the in situ devices to those made in the ex situ-process, the former show better performance in both T_N and IF bandwidth. Some caution is required in making this remark, since other processing steps have been modified slightly, too. We do not believe that this has an effect on the sensitivity measured in the device. We therefore conclude that Nb HEBMs are best made using the in situ-fabrication route.

Outlook

Although the work described in this thesis did not culminate in a ready-to-use receiver, we feel it is a step forward in the understanding and development of super-THz receivers in general and more specifically at DIMES/SRON. We identify three important areas in which progress has been made. First, diffusion-cooled Nb HEBMs have been designed and fabricated that have a sensitivity and IF bandwidth comparable to similar devices reported in literature. Second, we have obtained experience in the design of super-THz coupling structures. Third, hardware has been developed to measure both the direct and heterodyne response of Nb HEBMs up to 3 THz.

Bottlenecks foreseen in future work

In the course of this work, it has become clear that the fabrication and handling of Nb HEBMs is not straightforward. The reproducibility of this

process, particularly the deposition of the Nb thin film, is not sufficient — not even for even small series of detectors. The main problem is the reproducibility of T_c and $R_\square$. These parameters are critically dependent on the condition of the tool used to deposit the Nb thin film. In our believe, this issue is —although technological in nature— hard to overcome. Another point of concern is the procedure used to define the final etch mask and the final etching step. Finally, recently some concern has arisen with respect to the exact geometry and profile of the resist used in the deposition of the Au cooling pads. However, it is believed that these last two issues are not fundamental in nature and can be overcome relatively easily.

Once the fabrication process is finished, the devices have to be cut into die. At this point in time, they are *extremely* sensitive to ESD. This calls for very strict procedures for handling, mounting, testing and ESD-safe equipment. In our experience, even when the device is 'safely' inside the vacuum atmosphere of the dewar, shorted and all, thermal cycling or some external pulse can change the electrical properties of the device. Obviously, this is not favourable when these detectors are hooked up to a telescope, not to mention a space-born platform ...

Besides these practical bottlenecks, there is a lack in theoretical understanding of the noise mechanisms in HEBMs. No rigorous theory describing the sensitivity of superconducting hot-electron bolometer mixers is available. In this work, we have established a model to simulate a large part of the coupling from the telescope to the nanobridge. We believe that the model described in this thesis can be used for further development of THz HEBMs. However, although quite some work has been done, no model similar to the well-known Tucker-theory for SIS-mixers has been developed yet. The lack of such a model makes complete optimization along the route of simulations quite difficult. A complete model has to include a description of the rf losses as well. Certainly at high frequency, this is of prime importance to be able in order to estimate the optical losses.

Recommendations for future use

When one intends to proceed working on Nb HEBMs, it is worthwhile to consider the effort and equipment required from a fabrication-point-of-view. In our opinion, it is of major importance to control the Nb thin film quality

in the process and between the different process runs. This can only be done accurately in a dedicated tool set. The vacuum condition of the deposition tool should be optimal, and, the tool should not, if possible, be modified. Especially, the partial pressure of H_2O and O_2 should be as low as possible. Ideally, a ultra high vacuum system is used for this deposition step. Having a dedicated tool set available allows one to run the process undisturbed. No interference from other users, and thereby excessive down time of equipment, can influence the quality of the devices. In this respect, foundry services are worth considering, especially when the cost of running a dedicated tool set for diffusion cooled Nb HEBMs are taken into account.

Competing technologies

Nowadays, only two major technologies are recognised that may lead to sensitive super-THz heterodyne receivers: diffusion– and phonon-cooled HEBMs. Usually, NbN thin films are used to fabricate phonon-cooled mixers. This type of devices has been shown to have excellent sensitivity and reasonably high IF bandwidth. More importantly, they are more robust and forgiving when used in practice. Considerably more phonon-cooled HEBMs have been evaluated and reported in recent years, indicating a more mature type of receiver. A drawback of this device is that it is hard to improve its IF bandwidth since it is limited by the thickness of the NbN film and the probability the hot phonons have to leave the substrate.

Considering the above, NbN is the best candidate to become the technology of choice for super-THz heterodyne receivers, as it is technologically better evolved and in general more mature than Nb diffusion-cooled devices. The drawback of a slightly lower IF bandwidth may only be overcome by a materials-science approach, including an optimal film/substrate match, as no straightforward solution seems available. In the search for HEBMs having a high sensitivity and IF bandwidth it is worthwhile mentioning the recent NbTiN-based phonon cooled HEBMs.

In short: NbN phonon cooled HEBMs seem ready for immediate application in an observatory, while its Nb nephew is —in our opinion— not ready yet.

Space applications based on HEBMs

Space applications still rely on the availability of LOs having enough power to pump the mixer to its optimum bias point. Although NbN is a successful mixer for groundbased– and laboratory work, it seems to require a somewhat higher LO power. No powerful solutions are available yet, although much work is being done in that area. Instead of optimizing the LO, one could decide to look at another type of HEBM. This mixer would have a low T_c (reducing both LO power requirements and mixer noise) and it would have to fullfill the IF bandwidth requirements as well. Such a mixer could be based on a thin NbAu bilayer, as has recently been introduced by our group. The exact bilayer composition could be varied to tune T_c. The presence of a normal metal would increase the diffusion constant (and thereby the IF bandwidth) to a high value. Although no mixer experiments have been reported yet, first measurements show promising results.

Looking over the horizon ...

Now that we've explored Nb HEBMs, we have to conclude that they are not yet mature enough for application in practical receivers. NbN is more mature and is able to provide good enough sensitivity for astronomical applications. Next to NbN, NbTiN is being considered for use in phonon-cooled HEBMs.

Although history has shown that not each new superconducting material makes a good bolometer, the recent discovery of MgB_2 as a superconductor may open up routes to produce HEBMs with a somewhat higher operating temperatures, which may not be favorable for sensitivity, but it certainly is for operating requirements. If a suitable barrier material can be developed, MgB_2 is a candidate for high-frequency SIS-detectors.

When one speculates on a possible successor of superconducting heterodyne receivers, the recent GaAs-quantum well detector[1] may be a good candidate to introduce quantum efficiency into the field of super-THz detection.

References

[1] S. Komiyama, O. Astafiev, V. Antonov, E. Kutsuwa and H. Hirai, Nature, **403**, 405 (2000).

Chapter 11

Samenvatting

Een quasi-optische THz mixer gebaseerd op een Nb diffusie-gekoelde hete-electronen bolometer mixer

Deze dissertatie beschrijft het ontwerp, de fabricage en de metingen aan een heterodyne ontvanger voor gebruik rond 2.5 THz. In deze ontvanger gebruiken we een zeer dun, supergeleidend niobium (Nb) baantje — ook wel *nanobrug* genoemd —als het mixend element. Dit type ontvanger noemt men een hete-electronen bolometer mixer (HEBM).

Het onderzoek dat is beschreven in dit proefschrift is gericht op het ontwikkelen en begrijpen van een dergelijke ontvanger bedoeld voor atmosferisch en astronomisch onderzoek. Concrete aandachtsgebieden zijn bijvoorbeeld het dunner worden van de ozonlaag (het beruchte 'gat in de ozonlaag') en de chemie die betrokken is bij de vorming van sterren uit ijle gaswolken. De — kleine — moleculen die hierbij betrokken zijn zenden uit op zeer karakteristieke frequenties in het THz-gebied. Door deze spectra te bestuderen kan de aanwezigheid, hoeveelheid en toestand van dergelijke moleculen worden bepaald. Deze gegevens zijn van groot belang voor het begrip van de processen die zich afspelen bij de afbraak van ozon en de vorming van sterren.

Dergelijke straling is uitermate zwak en het is van het grootste belang om, nadat de straling is verzameld door een telescoop, die met zo weinig mogelijk verlies in de eigenlijke detector, de supergeleidende strip, te brengen. De koppeling van de telescoop naar de nanobrug kan op verschillende manieren. Vanwege de hoge frequentie waarop deze detector werkt hebben we gekozen voor een quasi-optische aanpak, waarin de telescoop de opgevangen straling via een silicium (Si) lens bundelt op een antenne. De antenne

is via een transmissielijn gekoppeld aan de Nb brug. In dit proefschrift zijn twee typen transmissielijn gebruikt: co-planaire golfpijpen (CPWs) en microstrip transmissielijnen. Om te voorkomen dat de straling weglekt uit de omgeving van de nanobrug is een filterstructuur ontworpen die is gebouwd in dezelfde transmissie lijn als de koppelstructuur.

Om tot een goed ontwerp te komen dat weinig verliezen vertoont hebben we het gedrag van de detector (hier: antenne, transmissielijn, filterstructuur en nanobrug) als functie van de frequentie van de opvallende straling, ofwel: de directe respons, gesimuleerd. Deze simulatie is gedaan met behulp van zelfontworpen software die de eigenschappen (vooral de 'impedantie') van elk element (antenne, transmissielijn, filterstructuur en nanobrug) apart berekent als functie van de frequentie. Deze impedanties worden wiskundig 'aan elkaar geknoopt' en geven zo het gedrag van het geheel als functie van de frequentie. Deze methode is vergeleken met commercieel verkrijgbare software die de structuur als geheel bekijkt en daarbij gebruik maakt van de Momenten-methode (MoM). De resultaten komen goed overeen: voor de frequentie waarbij de structuur het meeste signaal opvangt, de piekfrequentie, en voor het frequentiebereik waarover dit gebeurt, de rf bandbreedte, worden door beide methodes vrijwel dezelfde waarden gevonden. Laatstgenoemde methode toont het effect van de onderlinge samenhang van de geometrie van de elementen en hun effect (zg. resonanties) op de respons van de detector als functie van de frequentie. Deze effecten zouden van belang kunnen zijn voor het optimaliseren van een uiteindelijk ontwerp. In ons onderzoek echter wegen de voordelen van de zelfontworpen software — inzicht, snelheid en simpelheid — ruimschoots op tegen tegen de details die worden verkregen met de MoM-methode.

Om de geldigheid van de ontworpen modellen te testen — en natuurlijk om de uiteindelijke ontvanger echt te kunnen bouwen — hebben we de mixers gemaakt. Dit is gedaan met technieken die 'geleend' zijn uit de halfgeleidertechnologie: het zogenaamde *chips bakken*. Met deze nano– en microlithografische-technieken kunnen structuren met afmetingen van 0.000020 mm worden gerealiseerd (dat is $20 \cdot 10^{-9}$ m ofwel 20 nanometer. Een mensenhaar is van de orde 0.070000 mm, dus zo'n 3500 maal zo dik!) Zowel ontvangers gebaseerd op CPW– als op microstrip transmissielijnen zijn gebouwd. Eén van de grootste moeilijkheden in dit proces is het deponeren van een *supergeleidende* Nb nanobrug van 200 nm $\times$ 200 nm $\times$ 12 nm en om

hieraan ook nog een goed electrisch contact te bewerkstelligen. We hebben dit probleem op twee manieren opgelost. In één proces wordt, na de depositie van het dunne Nb, het vacuüm verbroken om gouden (Au) koelflappen te deponeren. Dit proces heet het ex situ proces. In het in situ proces wordt, zonder het vacuüm te verbreken, een dubbellaag Nb/Au (12/15 nm) neergelegd. Pas nu wordt het vacuüm verbroken en worden de Au koelflappen gepatroneerd. Het overtollige Au wordt in een latere stap verwijderd. Door het Au boven het Nb wordt voorkomen dat er een Nb-oxidelaagje ontstaat tussen het Nb en het Au. Dit laagje is verantwoordelijk voor een hoge electrische en thermische weerstand.

De gesimuleerde directe respons is vergeleken met de respons zoals we die hebben gemeten aan de ontvangers. Voor zowel de CPW- als de microstriplijn-gekoppelde detectoren meten we piekfrequenties en bandbreedtes die in het algemeen goed overeenkomen met de gesimuleerde waarden. In beide types echter vinden we een opvallend verschil, een verschuiving naar lagere frequenties met zo'n 10 tot 15%, tussen de praktijk en de simulatie. Een dergelijk verschil is ook door andere onderzoeksgroepen gevonden. We geloven dat de oorsprong van deze verschuiving ligt in het 'samenknijpen' van de stroom als die vanuit de — relatief brede — signaaldraad van de CPW- of microstriplijn in de veel smallere nanobrug wordt gedwongen. We concluderen dat we, als we de verschuiving in het model meenemen, de directe respons voldoende kunnen modelleren om er praktisch toepasbare koppelingsstructuren voor THz detectoren mee te ontwerpen.

We hebben de ontvangers ook als heterodyne ontvangers ('mixers', vergelijkbaar met radio- en tv-ontvangers) getest. De gevoeligheid, de bandbreedte van de middenfrequentie (IF bandbreedte) en het conversieverlies zijn gemeten bij frequenties tussen 0.35 en 2.5 THz. Verscheidene detectoren zijn getest, gebaseerd op CPW- en microstrip transmissielijnen en op in situ en ex situ geproduceerde koelflappen. De heterodyne eigenschappen van nanobruggen met in situ geproduceerde koelflappen zijn beter dan die van hun ex situ gemaakte broertjes: ze tonen een hogere gevoeligheid, een lager conversieverlies en, vooral, de hoogste IF bandbreedte. Het verschil tussen CPW- en microstrip lijn gekoppelde mixers hebben we niet zo duidelijk gezien. Een systematisch onderzoek naar hun eigenschappen zou wellicht een antwoord kunnen geven op de vraag welke koppelingsstructuur het best geschikt is voor het gebruik in een toepasbare detector.

Chapter 12

Summary

A Quasi-Optical THz Mixer Based on a Nb Diffusion-Cooled Hot Electron Bolometer

This thesis describes the design, fabrication and measurements on a heterodyne receiver designed for use around 2.5 THz, in which we employ a Nb superconducting strip as the mixing element: a *hot-electron bolometer mixer*.

Ultimately, the research described in this thesis is aimed at understanding and developing a heterodyne receiver for use in atmospherical and astronomical research, for example into the physical and chemical processes involved in the destruction of the ozone layer and the formation of stars.

The circuit used to couple rf radiation efficiently into the mixing element is of utmost importance for a high-sensitivity detector, especially at high (1–3 THz) frequency. We use a twin-slot antenna combined with a transmission line to achieve a high coupling. The antenna is connected to the nanobridge using either a co-planar waveguide (CPW) or a microstrip transmission line. For both systems, we have simulated the direct response as a function of frequency with a model that describes the impedance of the elements that form the mixer, i.e. the antenna, transmission line, filter and nanobridge. The advantages of this approach over a Method-of-Moments-approach are its simplicity, straightforwardness and speed of calculation. A comparison between our approach and the MoM-method shows that the general behavior of both is similar. The MoM-approach is capable of showing features that are due to the exact geometry of the elements and their interdependence. These might be of interest for fine tuning the coupling system.

To check the validity of the simulations, the system we describe is produced using micro– and nanolithographical techniques borrowed from semiconductor industry. Both the CPW– and a microstrip line coupled bolometer have been realized in practice. One of the main bottlenecks in the process is to fabricate a *superconducting* Nb nanobridge (typically 200 nm × 200 nm × 12 nm) and to establish good electrical contact to this bridge. We have solved this problem in two ways. In one process, the vacuum is broken directly after the deposition of the Nb to define Au cooling pads on top of the Nb nanobridge: the ex situ process. In the other, a Nb/Au bilayer is defined, and only thereafter the vacuum is broken to further define the Au cooling pads. The excess Au is removed at a later stage. This is what we call the in situ process.

The direct response of the devices thus produces is compared to the simulated response. For both the CPW– and the microstrip line coupled response we find that the values measured for the frequency at which coupling is maximal, f_{center}, and bandwidth B, in general agree well with the calculated behavior. In both types of device, however, one striking difference between theory and experiment is observed: a rather large — 10–15% — downshift of f_{center}. The origin of this shift is believed to be due to an inductance caused by the squeezing of the current from the central conductor (in the CPW-device) or top wiring (in the microstrip line case). We conclude that, taking the additional shift into account, the direct response is described accurately enough to be of practical value in the design of THz coupling structures.

The devices have also been investigated in heterodyne mode. The sensitivity, IF (gain) bandwidth and conversion gain have been measured at frequencies ranging from 0.35 to 2.5 THz. Several devices have been measured: ex situ, in situ, CPW– and microstrip line based. The heterodyne performance of in situ devices is better than that of their ex situ brothers: they show higher sensitivity, higher gain and especially highest IF bandwidth. The difference between CPW– and microstrip line devices has not been observed so clearly. A systematic study of their properties may reveal which device is to be preferred for use in a practical receiver.

Appendix A

Experimental methods and equipment used in the heterodyne measurements

In this Appendix, we describe the equipment and concepts used for the rf measurements. The cryogenic hardware is described, followed by a sketch of the setup used in the sensitivity measurements. The setup for the IF bandwidth measurements is shown, after which the method to measure T_N and G_{Mix} are explained, followed by a discussion of T_{out}.

A.1 Experimental set up

All rf measurements require the device to be in a superconducting state, i.e. at a temperature below about 6 K. The cryogenic equipment thus plays an important role in all measurements and is described first.

A.1.1 Cryogenic hardware

The direct detection measurements reported in Chs. 6 and 7 and the heterodyne experiments performed in Ch. 8 and 9 require the device to be in a superconducting state. A ℓHe-dewar is used to obtain temperatures around 4.2 K, and, if required even as low as 2 K by pumping on the bath. Fig. A.1 shows a schematic cross section of such a dewar. The mixer block is mounted on the 4.2 K cold plate. Care is taken to have all interfaces highly thermally

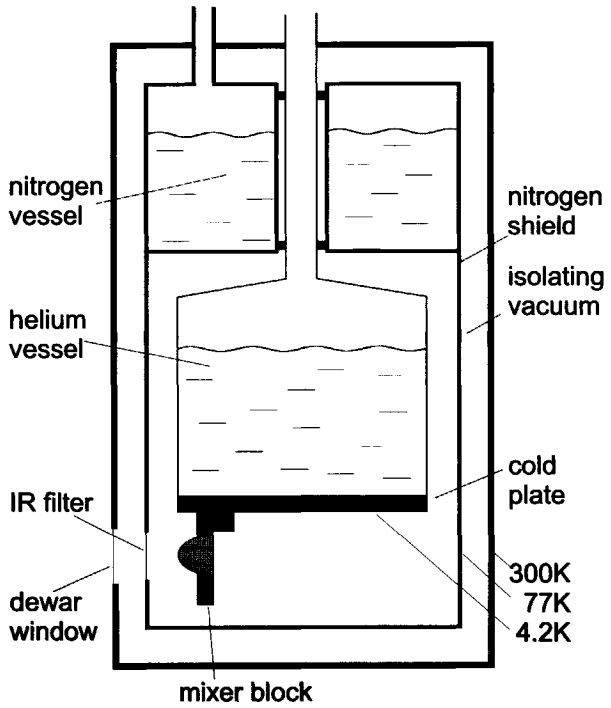

FIGURE A.1. Drawing of the dewar used in the rf experiments. By pumping the ℓHe bath, the temperature at the cold plate can be reduced to about 1.7 K. It is noteworthy that the IF amplifier and isolator are also mounted on this stage. The dewar window is a sheet of Mylar, typically 40 μm thick, the IR filter is a sheet of Zitex G104. This effectively blocks radiation with a frequency higher than 5 THz. Fig. A.2 shows the mixer block in more detail.

conducting. In operating conditions, the temperature of the device is estimated to be about 0.5 K higher than that of the cold plate. Fig. A.2 is a detailed drawing of the QO mixer block used in our set up.

The bias-T, isolator and IF amplifier are mounted on the 4.2 K-stage, so that they contribute as little to Johnson-noise as possible to the mixer's signal. In order to be able to switch amplifiers during a measurement (i.e. while cold), an rf switch is placed on the cold stage. It is possible to switch between the wide-band (for IF bandwidth measurements) and the narrow-

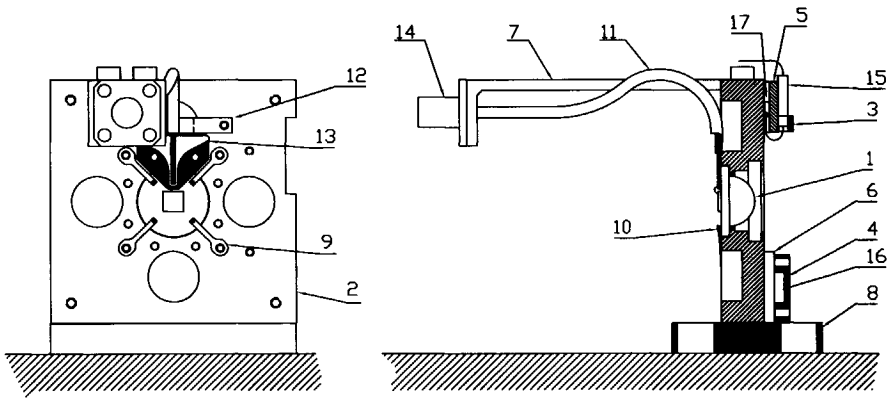

FIGURE A.2. Drawing of the mixer block used in the rf experiments. The numbering corresponds to Table A.1. Small modifications have been made to the block over the years; the most important being the replacement of the coaxial IF cable by a microstrip line launched directly to an SMA connector. Thermal coupling from the cold plate to the mixer die is optimized by applying vacuum grease and In foil at the Cu-Cu and Cu-Si interfaces.

TABLE A.1. Legenda for Fig. A.2

1	Si lens	10	lens protector
2	mixer block (Cu)	11	IF coax cable
3	electr. conn. 4 pt	12	cable clamp
4	electr. conn. 2 pt	13	IF circuit board
5	T-sensor block	14	SMA conn.
6	T-heater block	15	electr. conn. 4 pt
7	support IF cable	16	electr. conn. 2 pt
8	block support	17	T-sensor
9	spring		

band (for sensitivity measurements) IF chains by operating this switch.

A.1.2 Sensitivity measurements

Fig. A.3 schematically shows the setup used in the measurements of the sensitivity and gain of the HEBMs. The device is pumped by a local oscillator (LO). For frequencies below 1.5 THz, a backward wave oscillator (BWO) or a carcinotron is used to generate LO power. At 1.9 and 2.5 THz a far infrared (FIR) gas laser acts as an LO. Power from the LO is coupled onto the Si lens inside the dewar using a Mylar beam splitter in reflection mode. Additional polyethylene lenses can be used to focus the LO beam for optimal coupling. The power level is adjusted by rotating a polarizer in the beam. A black-body behind the beam splitter acts as the signal source (note that, in this measurement, we regard the 'noise' from the black body as the signal): one piece of Eccosorb (a nearly ideal black body in the sub-mm region) is kept at room temperature, while another is at 77 K. Using Planck's law, the power coming from the black body can be calculated. The black body thus acts as a calibrated load. The combined LO and signal power enter the dewar via a 40 μm Mylar window at 300 K. A Zitex G104 IR filter at 77 K absorbs most of the optical and infrared radiation (component (1) in Fig. A.3). Optionally, a piece of crystalline quartz and another Zitex sheet, together acting as a low-pass filter, are mounted at 4.2 K to further reduce the effects of direct detection. This is only used in measurements at a frequency lower than 1 THz.

A synthesized elliptical or elliptical Si lens (2) focuses the radiation onto the on-chip antenna. This chip is glued to the lens, with its non-processed side facing the lens. Mixing takes place in the superconducting nanobridge. The IF signal is then coupled into the IF chain, which is shown in Fig. A.4. Via short bond wires, the IF signal is fed into a microstrip line printed circuit board (PCB), launching into an SMA cable. A bias-T (3) (Radiall R441530, 0.010–1.5 GHz acc. to specs, but in practice wider) allows dc biasing of the device via the SMA cable and IF board. An isolator (4) absorbs all reflections due to the mismatch between the device's output impedance and the line's 50 Ω to ground, thus avoiding standing waves. A Berkshire cryo-amplifier (5) amplifies the signal by about 40 dB before the signal is taken out of the dewar and is once more amplified 40 dB by a Miteq 0.1–15 GHz amplifier

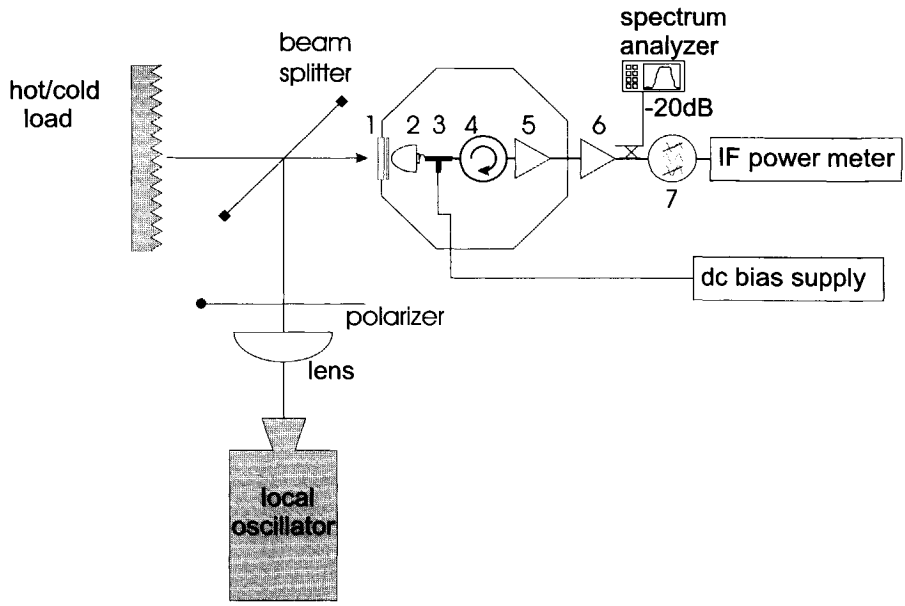

FIGURE A.3. Drawing of the setup used in the sensitivity measurements. A black body at a known temperature (~300 K or ~77 K) is used as the load. The low noise IF amplifier (5) ranges from 1.2–1.8 GHz. A tunable (1–2 GHz) 80 MHz bandpass filter (7) is placed in front of the IF power detector.

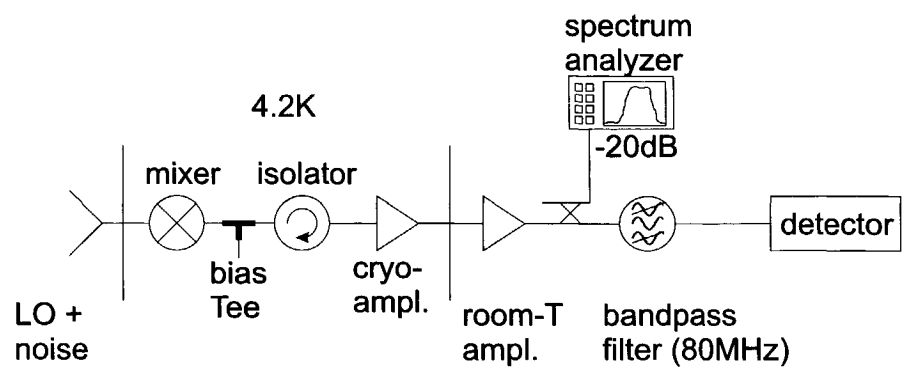

FIGURE A.4. Drawing of the IF chain used in the sensitivity measurements.

(6). A -20 dB directional coupler couples a small fraction of the signal to an HP spectrum analyzer for monitoring the IF chain's performance. The rest of the signal is input to a tunable K&L bandpass filter (7) (80 MHz between 1–2 GHz), allowing the selection of a narrow band in which the IF power is measured. The final detector is an HP power meter. Usually, the best matching through the IF chain is obtained around 1.35 GHz, which is why most measurements are performed at that frequency.

Data acquisition is done by computer. I(V)-curves can be taken, together with the output power at IF, P_{IF}. Note that this is a (quasi)-dc quantity! If the lack of LO stability requires so, the hot/cold load is chopped and P_{IF} is analyzed by a lock-in amplifier. The modulation $P_{IF,\,ac}$ is due to the power change at the input while chopping between hot and cold. $P_{IF,\,dc}$ is the steady signal from all noise sources in the system. $P_{IF,\,hot}$ and $P_{IF,\,cold}$ can be calculated from these data using

$$\begin{aligned} P_{hot} &= P_{IF,\,dc} + \alpha P_{IF,\,ac} \\ P_{cold} &= P_{IF,\,dc} - \alpha P_{IF,\,ac}, \end{aligned} \tag{A.1}$$

where α is the so-called chop factor, which corrects for the error introduced by chopping the beam. α is determined by manually introducing a hot and cold piece of Eccosorb in the beam, thus taking out the effects of the chopper and lock-in amplifier.

A.1.3 IF bandwidth measurements

At first glance, the setup for the IF bandwidth measurements is very similar to that used for measuring sensitivity (see Fig. A.5). However, there are two major differences. One is the fact that the black body load is replaced by a coherent source, the other is that the IF chain is made wide-band. Since the IF behavior of the device has to be measured accurately, it is important to have an IF chain that spans at least a few times the IF bandwidth of the device.

In principle both the LO and signal frequency can be tuned to span the entire IF bandwidth of the device. However, since it is hard to keep the output power of a small signal constant when tuning its frequency, we change the LO frequency to measure IF bandwidth. The LO power is kept constant by monitoring the current level through the device and keeping it constant to better than 1 μA by rotating a polarizer in the LO beam.

Since the IF chain has to be wide-band, we remove the narrow band isolator and change the bias-T to a Radiall R441533 (3) (1.5–6 GHz acc. to specs, but in practice down to below 0.5 GHz). The function of the isolator —to avoid standing waves— is taken over by 3 dB-attenuators. These are placed at the position of the dots in Fig. A.6. A Miteq 0.1–8 GHz cryo-amplifier (4) is now used to boost the signal. The same room temperature amplifier (5) is used, but the bandpass filter is taken out of the chain. Instead of using a power detector, power and frequency are determined from the spectrum analyzer. Using a cryo-switch inside the dewar (not shown), it is possible to switch between the narrow– and wide-band chain. This feature allows us to do sensitivity– and bandwidth measurements in one cooldown run. Since the electrical properties of the HEB can change slightly upon thermal cycling, this is a useful feature of the setup.

A.2 Experimental methods

A.2.1 Noise temperature: the Y-factor measurements

The noise added by a heterodyne receiver is usually measured using the Y-factor technique. This technique compares the output signal in a certain frequency band Δf after the receiver when it is looking at hot and cold loads of well-known temperature. Both loads are assumed to be black-bodies at a temperature T, emitting a power per unit bandwidth Δf that is described by Planck's law:

$$P(T,f) = \frac{hf\Delta f}{e^{\frac{hf}{k_B T}} - 1}, \tag{A.2}$$

in which h and k_B are Planck's and Boltzmann's constant, respectively. The output powers of the receiver with the hot and cold loads are now given by:

$$P_{out,\,hot} = G\left[P_{rec} + P_{in}(f, T_{hot})\right] \tag{A.3}$$

and

$$P_{out,\,cold} = G\left[P_{rec} + P_{in}(f, T_{cold})\right], \tag{A.4}$$

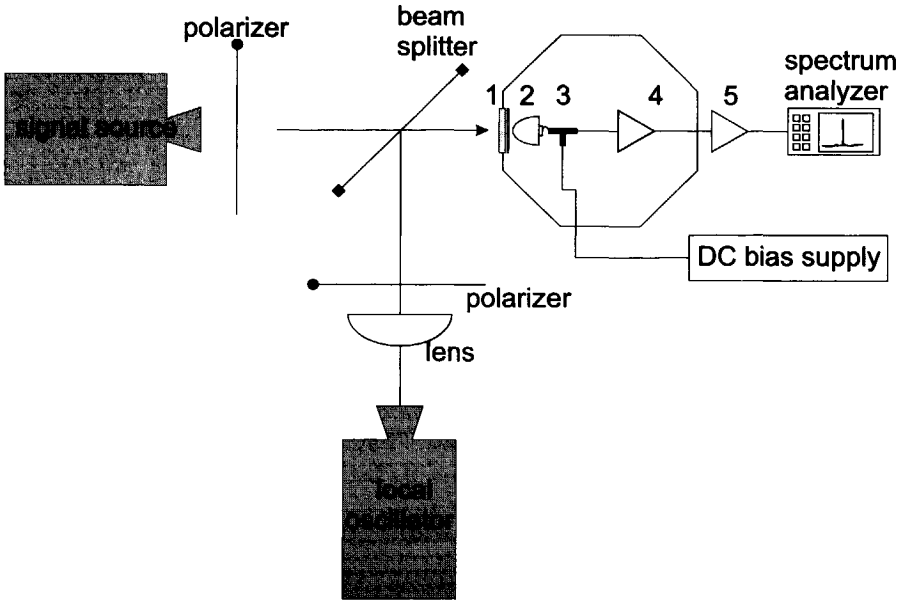

FIGURE A.5. Drawing of the setup used in the IF bandwidth experiments. Instead of a hot/cold load, we now use a second, much weaker, THz source of a well known frequency. The IF chain consists of a wideband amplifier (4) (0.1–8 GHz) at 4.2 K and a 0.01–15 GHz amplifier at room temperature (5). The IF band is monitored using an HP spectrum analyzer.

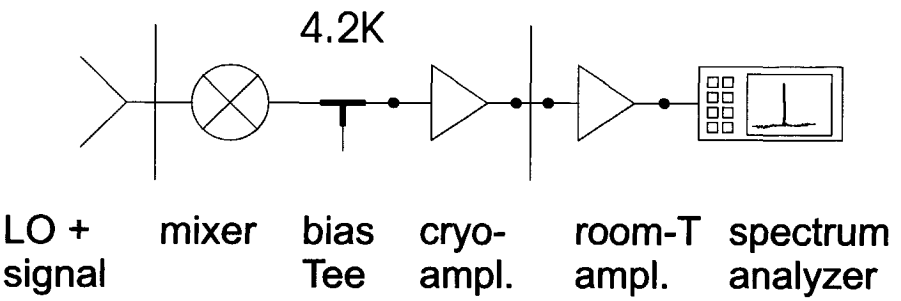

FIGURE A.6. Detailed drawing of the IF chain used in the IF bandwidth measurements.

respectively. G is the gain of the receiver and P_{rec} is the power added by the receiver ('noise'). The Y-factor is now introduced as follows:

$$Y_{dB} = 10 \cdot \log\left[\frac{P_{out,\,hot}}{P_{out,\,cold}}\right] = 10 \cdot \log\left[\frac{P_{rec} + P_{in}(f, T_{hot})}{P_{rec} + P_{in}(f, T_{cold})}\right]. \tag{A.5}$$

From this equation, one can see that the amount of noise added by the receiver to the black body power determines the Y-factor. The noise power added by the receiver can be written as

$$P_{rec} = \frac{P_{out,\,hot} - 10^{0.1 \cdot Y_{dB}} \cdot P_{out,\,cold}}{10^{0.1 \cdot Y_{dB}} - 1}. \tag{A.6}$$

In radio astronomy, it is common practice to express this output power in a noise temperature using $P = k_B TB$, in which B is a constant bandwidth of 1 Hz.

The total noise temperature has contributions from many elements in the signal path:

$$T_{Rec} = T_{opt} + \frac{T_{Mix}}{G_{opt}} + \frac{T_{iso}}{G_{opt} G_{Mix}} + \frac{T_{IF}}{G_{opt} G_{Mix} G_{iso}} \tag{A.7}$$

A.2.2 Gain

Another important feature of a heterodyne mixer is its ability to convert high-frequency signal into IF signal, or conversion gain G. It is important to note that all gains quoted in this thesis are *single sideband* (SSB) gains. For the measured gain values it is assumed that the upper sideband (USB) and lower sideband (LSB) contribute equally to the power at the IF band. Furthermore, throughout this thesis, it is assumed that the mixer is operated in double sideband (DSB) mode.

SSB mixer- and receiver gain $G_{Rec,\,Mix}$ are defined as follows:

$$G_{Rec} = 10 \cdot \log\left(\frac{1}{2}\frac{\Delta P_{IF}}{G_{IF} \Delta P_{signal}}\right) \tag{A.8}$$

$$G_{Mix} = 10 \cdot \log\left(\frac{1}{2}\frac{\Delta P_{IF}}{G_{IF} \Delta P_{signal,\,eff}}\right) = 10 \cdot \log\left(\frac{1}{2}\frac{\Delta P_{IF}}{G_{IF} k_B (T_{eff,h} - T_{eff,c})}\right) \tag{A.9}$$

G_{IF} is the gain of the IF chain. We calibrate this by using an SIS mixer as a well-known shot noise source[2]. We calibrate over the whole IF band at a bath temperature of 2.8 K. In this measurement, the noise temperature of the IF chain is also measured. We measure $G_{IF} = 80.2$ dB and $T_{IF} = 6$ K. We note, however, that the physical temperature of the isolator's load is estimated to be about 8 K, which is higher than the temperature of the cold plate. This is due to thermal loading from the amplifier. However, since this load is only weakly coupled to the IF amplifier (via $T = 1 - \gamma^2$, the power transmission coefficient), this is not strongly reflected in the noise power added by the isolator.

ΔP_{IF} is the difference in IF output power when looking at hot and cold loads, ΔP_{signal} is the difference between the rf power coming from the black body hot and cold loads. $\Delta P_{signal,eff}$ is the amount of black body power actually delivered to the superconducting bridge. Once again, the difference between G_{Mix} and G_{Rec} is that in the former the influence of the optics and IF chain is taken out, so that only the intrinsic gain of the bridge remains.

A.2.3 Mixer output noise

The mixer output noise T_{out} has two major contributions:

$$T_{out} = T_J + T_{EFN}. \tag{A.10}$$

T_J is the Johnson– (or Nyquist–) noise, which is not frequency dependent[3,4]. T_{EFN} is the contribution due to thermal fluctuations of the electrons. The rate at which electrons remove heat from the nanobridge fluctuates somewhat. This gives rise to fluctuations in the hot spot length. This is seen at the IF output port as extra noise: electron fluctuation noise (EFN). Since the frequency dependence of these fluctuations is known to be Lorentzian in the diffusion-cooled HEBM, we can write T_{out} as follows:

$$T_{out}(f) = T_J + T_{EFN}(0) \cdot \frac{1}{1 + \left(\frac{f}{f_{3\,dB}}\right)^2}. \tag{A.11}$$

T_{out} can be calculated from the mixer gain and mixer noise temperature using $T_{out} = 2 \cdot G_{Mix} \cdot T_{Mix}$ or it can be measured using

$$T_{out} = \frac{\frac{P_{hot}}{P_{SC}}(T_{iso} + T_{amp}) - (1 - \Gamma)(T_{iso} + T_{amp})}{\Gamma}, \tag{A.12}$$

where P_{SC} is the output power when the device is fully superconducting, i.e. at zero bias voltage. T_{iso} and T_{amp} are the noise temperature of the isolator and amplifier, respectively.

References

[1] Zitex G104, Norton Performance Plastics, Wayne, New Jersey, (201)696-4700.

[2] G. de Lange, *Quantum Limited Heterodyne Detection of 400–840 GHz Radiation with Superconducting Nb Tunnel Junctions*, Ph. D. thesis, University of Groningen (1994).

[3] H. Ekström, B.S. Karasik, E. Kollberg and K.S. Yngvesson, IEEE Trans. Microwave Theory Techn. **43**, 938 (1995).

[4] B.S. Karasik and A.I. Elantiev, Appl. Phys. Lett. **68**, 853 (1996).

Appendix B

Production parameters for Nb HEBMs

This appendix contains a detailed description of the fabrication process used to produce *in situ* HEBMs. This process is run at the DIMES cleanroom facility, class 10,000, June 2001. The equipment used is indicated, as are the materials (photoresist, wafers, ...) and computer files for the EBPG. Important parameters (baking temperatures, spin speeds, ...) are indicated.

B.1 Production parameters for Nb HEBMs

1. Cleaning wafers

Rinse the wafers in:

1. demi water, 5 min.
2. H_2SO_4(96%) : H_2O_2(30%), 1 : 1, 100°C, 10 min.
3. demi water until clean
4. 1% HF, room temperature, 30 sec.
5. demi water until clean
6. NH_4OH(25%) : H_2O_2(30%) : H_2O, 1 : 1 : 5, 80°C, 10 min.
7. demi water until clean
8. HCl(37%) : H_2O_2(30%) : H_2O, 1 : 1 : 6, 80°C, 10 min.
9. demi water until clean
10. spin dry.

2. Nb/Au deposition

- Oil between chuck and sample
- 100% separation
- Cooled table
- 15 min. pause after load

Condition chamber
Nordiko 2000
Dedicated chuck

Flow: 60 sccm Pressure: 8 mTorr
Pre-sputter:
Metal: Nb
Power: 130 W Time: 1800 s

Ar sputter etch
Nordiko 2000

Gas: Ar Bias: -300 V
Pressure: 8 μBar Power: 200 W
Flow: 60 sccm Time: 120 s

Nb deposition
Nordiko 2000

Flow: Ar, 60 sccm **Pressure: 8 mTorr**
Pre-sputter: **Sputter:**
Metal: Nb **Power: 130 W**
Power: 130 W **Time: 24 s**
Time: 300 s **Thickness: 14 nm**

Au deposition
Nordiko 2000

Flow: Ar, 60 sccm Pressure: 8 mTorr
Pre-sputter: **Sputter:**
Metal: Au Power: 50 W
Power: 50 W Time: 13 s
Time: 30 s Thickness: 11 nm

- rinse acetone
- rinse iso-propanol
- rinse water
- spin dry

3. EBL cooling pad definition

- PMMA, 2010 in Cl-benzene, 5 s. 500 rpm, 55 s 3500 rpm, 5 min. 120° C
- PMMA, 2041 in o-xylene, 5 s. 500 rpm, 55 s 4500 rpm, 5 min. 120° C

- Leica PG5 HR FEG, 1050 μCcm^{-2}, beam: 31NM_37NA_400UM_100KV, defocussed spot-size: 0.

Develop:
isopropanol : MIBK 3:1, 30 s.
isopropanol, 30 s.
Blow dry

Descum
New Leybold

Gas: O_2	Bias: -180 V
Pressure: 6 μBar	Power: 20 W
Flow: 20 sccm	Time: 30 s

Au deposition
Leybold evaporator

Metal 1: Ti (getter only)	Metal 2: Au
P_{back}: $3 \cdot 10^{-7}$ mBar	P_{evap}: $2 \cdot 10^{-6}$ mBar
P_{evap}: $4 \cdot 10^{-7}$ mBar	Thickness: 100 nm

Lift-off
Boiling acetone, 30'.
Spray acetone
2 × 3 min ultrasonic, spray acetone
Rinse isopropanol, spin dry

4. Nb patch definition

- Microposit 1813 12%, 5 s. 500 rpm, 55 s. 3250 rpm (HMDS condensation), 3 min. 95°C
- SNR M2 in xylene 1:3, 5 s. 500 rpm, 55 s. 3000 rpm, 30 min. 60°C
- Leica PG5 HR FEG, 120 μCcm^{-2}, beam: 29NM_22NA_400UM_100KV, defocussed spot-size: 75.

Develop:
xylene, 35 s., upside down, agitate heavily.
cyclohexane, 20 s.
blow dry

Resist burn
New Leybold

Gas: O_2	Bias: -120 V
Pressure: 6 μBar	Power: 20 W
Flow: 20 sccm	Time: 600 s

Etch until endpoint detection signal flat

Optimize profile
New Leybold

Gas: O_2	Bias: -20 V
Pressure: 200 μBar	Power: 10 W
Flow: 20 sccm	Time: 300 s

- Clean, dedicated Nb chuck
- Oil between chuck and sample
- 100% separation
- Cooled table
- 15 min. pause after load

Au removal (Ar)
Nordiko 2000

Gas: Ar	Bias: -300 V
Pressure: 8 μBar	Power: 200 W
Flow: 60 sccm	Time: 180 s

Split 3 min. in 3 equal parts. Ignition of plasma: 5 s. 25 mTorr each time.

RIE-Nb removal in the Groningen-etcher

Prepare chamber
Groningen-RIE

Gas: $CF_4 + 4\%O_2$	Bias: -120 V
Pressure: 70 μBar	Power: 50 W
Flow: 35 sccm	Time: 2700 s

RIE-etch
Groningen-RIE

Gas: $CF_4 + O_2$	Bias: -120 V
Pressure: 70 μBar	Power: 50 W
Flow: 35 sccm	Time: 124 s

Remove resist in PRS 3000 (80°C) with ultrasonic agitation. Rinse in acetone and isopropanol.

5. RF groundplane definition

- Microposit 1813 27%, 5 s. 500 rpm, 55 s. 3250 rpm (HMDS condensation), 3 min. 95°C
- (as-bought SNR M2 in xylene 1:1) : xylene 1:1, 5 s. 500 rpm, 55 s. 3000 rpm, 30 min. 60°C
- Leica PG5 HR FEG, 120 μCcm^{-2}, beams: 29NM_22NA_400UM_100KV and 60NM_179NA_400UM_100KV, defocussed spotsize: 75 and 375, resp.

Develop:
xylene, 35 s., upside down, agitate heavily.
cyclohexane, 20 s.
blow dry

Resist burn
New Leybold

Gas: O_2	Bias: -120 V
Pressure: 6 μBar	Power: 20 W
Flow: 20 sccm	Time: 3600 s

Etch until endpoint detection signal flat

Optimize profile
New Leybold

Gas: O_2	Bias: -20 V
Pressure: 200 μBar	Power: 10 W
Flow: 20 sccm	Time: 300 s

- Clean, dedicated Nb chuck
- Oil between chuck and sample
- 100% separation
- Cooled table
- 15 min. pause after load

Ar sputter etch
Nordiko 2000

Gas: Ar	Bias: -300 V
Pressure: 8 μBar	Power: 200 W
Flow: 60 sccm	Time: 120 s

Al deposition
Nordiko 2000

Flow: Ar, 60 sccm	Pressure: 8 mTorr
Pre-sputter:	**Sputter:**
Metal: Al	Power: 40 W
Power: 40 W	Time: 20 s
Time: 120 s	Thickness: 6 nm

Au deposition
Nordiko 2000

Flow: Ar, 60 sccm	Pressure: 8 mTorr
Pre-sputter:	**Sputter:**
Metal: Au	Power: 100 W
Power: 100 W	Time: 14 s
Time: 30 s	Thickness: 22 nm

Au deposition
Leybold evaporator

Metal 1: Ti (getter only)	Metal 2: Au
P_{back}: $2 \cdot 10^{-7}$ mBar	P_{evap}: $2 \cdot 10^{-6}$ mBar
P_{evap}: $1 \cdot 10^{-7}$ mBar	Thickness: 300 nm

Lift-off
Boiling acetone, 30'.
Spray acetone
2 × 3 min ultrasonic, spray acetone.
If necessary: PRS 3000 (80°C) with ultrasonic agitation. Rinse in acetone and isopropanol.
Repeat until clean.

6. Removal of Au passivation layer

- Clean, dedicated Nb chuck
- Oil between chuck and sample
- 100% separation
- Cooled table
- 15 min. pause after load

Au removal (Ar)
Nordiko 2000

Gas: Ar	Bias: -300 V
Pressure: 8 μBar	Power: 200 W
Flow: 60 sccm	Time: 180 s

Split 3 min. in 3 equal parts. Ignition of plasma: 5 s. 25 mTorr each time.

7. EBL bridge width definition

- PMMA, 2010 in Cl-benzene, 5 s. 500 rpm, 55 s 3500 rpm, 5 min. 120° C
- PMMA, 2041 in o-xylene, 5 s. 500 rpm, 55 s 4500 rpm, 5 min. 120° C
- Leica PG5 HR FEG, 1100 μCcm^{-2}, beam: 31NM_37NA_400UM_100KV, defocussed spot-size: 0.

Develop:
isopropanol : MIBK 3:1, 30 s.
isopropanol, 30 s.
Blow dry

Descum
New Leybold

Gas: O_2	Bias: -180 V
Pressure: 6 μBar	Power: 20 W
Flow: 20 sccm	Time: 30 s

- Clean, dedicated Nb chuck
- Oil between chuck and sample

- 100% separation
- Cooled table
- 15 min. pause after load

Ar sputter etch
Nordiko 2000

Gas: Ar	Bias: -300 V
Pressure: 8 μBar	Power: 200 W
Flow: 60 sccm	Time: 120 s

Al deposition
Nordiko 2000

Flow: Ar, 60 sccm	Pressure: 8 mTorr
Pre-sputter:	**Sputter:**
Metal: Al	Power: 40 W
Power: 40 W	Time: 100 s
Time: 120 s	Thickness: 30 nm

Lift-off
Boiling acetone, 30'.
Spray acetone
2 × 3 min ultrasonic, spray acetone.
Rinse in acetone and isopropanol.
Repeat until clean.

RIE-Nb removal in the Groningen-etcher

Prepare chamber
Groningen-RIE

Gas: $CF_4 + O_2$	Bias: -120 V
Pressure: 70 μBar	Power: 50 W
Flow: 35 sccm	Time: 2700 s

RIE-etch
Groningen-RIE

Gas: $CF_4 + O_2$	Bias: -120 V
Pressure: 70 μBar	Power: 50 W
Flow: 35 sccm	Time: 220 s

Rinse water
Remove Al in Shipley MF 321 photoresist developer: stir 2 min.
Rinse water
Dice using tap water (SRON old machine).

Publications

- W.F.M. Ganzevles, J.R. Gao, P. Yagoubov, W.J. Vreeling, P.A.J. de Korte and T.M. Klapwijk, *A Detailed Characterization of Quasi-Optically Coupled Nb Hot Electron Bolometer Mixers in the 0.3-3 THz range*, submitted to Proc. 13th Int. Symp. Space THz Techn. Boston, MA, March 26-28 (2002).

- W.F.M. Ganzevles, J.R. Gao, P.A.J. de Korte and T.M. Klapwijk, *Direct response of microstrip line coupled Nb THz hot-electron bolometer mixers*, Appl. Phys. Lett. **79**, 2483 (2001).

- P. Yagoubov, X. Lefoul, W.F.M. Ganzevles, J.R. Gao, P.A.J. de Korte and T.M. Klapwijk, *Development of a Nb/Au bilayer HEB mixer for space applications*, Proc. 12th Int. Symp. Space THz Techn., San Diego, CA, Feb., pp. 14-16 (2001).

- W.F.M. Ganzevles, L.R. Swart, J.R. Gao, T.M. Klapwijk and P.A.J. de Korte, *Direct and Heterodyne Response of Quasi-Optical Nb Hot-Electron Bolometer Mixers Designed for 2.5 THz Radiation Detection*, Proc. 4th European Workshop on Low Temperature Electronics, Noordwijk, The Netherlands, June 21-23 (2000).

- W.F.M. Ganzevles, P. Yagoubov, J. R. Gao, T. M. Klapwijk and P.A.J. de Korte, *Nb Superconducting Hot Electron Bolometer Mixers Coupled with Microstrip Lines*, IEEE Trans. on Appl. Supercond. **11**, p. 570-573 (2000).

- W. F. M. Ganzevles, L. R. Swart, J. R. Gao, T. M. Klapwijk and P. A. J. de Korte, *Direct response of twin slot antenna coupled hot-electron bolometer mixers designed for 2.5 THz radiation detection*, Appl. Phys. Lett. **76**, pp. 3304-3306, July 2000.

- W.F.M. Ganzevles, J.R. Gao, W.M. Laauwen, G. de Lange, T.M. Klapwijk and P.A.J. de Korte, *Direct and Heterodyne Response of Quasi-Optical Nb Hot-Electron Bolometer Mixers Designed for 2.5 THz Radiation Detection*, Proc. 11th Int. Symp. Space THz Techn., Ann Arbor, MI, May 1-3, pp. 69-81 (2000).

- W.F.M. Ganzevles J.R. Gao, P. Yagoubov, T.M. Klapwijk and P.A.J. de Korte, *Microstripline-Coupled Quasi-Optical Niobium Hot Electron Bolometer Mixers around 2.5 THz*, Proc. 11th Int. Symp. Space THz Techn., Ann Arbor, MI, May 1-3, pp. 60-68 (2000).

- W.F.M. Ganzevles, J.R. Gao, G. de Lange, D. Wilms Floet, A.K. van Langen, L.R. Swart, T.M. Klapwijk and P.A.J. de Korte, *Twin-Slot Antenna Coupled Nb Hot-Electron Bolometer Mixers at 1 THz and 2.5 THz*, Proc. 10th Int. Symp. Space THz Techn., Charlottesville, VA, March 16-18, pp. 247-260 (1999).

- D. Wilms Floet, J.R. Gao, T.M. Klapwijk, W.F.M. Ganzevles, G. de Lange and P.A.J. de Korte, *Receiver Measurements at 700 GHz with a Niobium Diffusion-Cooled Hot-Electron Bolometer Mixer*, Proc. 10th Int. Symp. Space THz Techn., Charlottesville, VA, March 16-18, pp. 229-237 (1999).

- W.F.M. Ganzevles, J.R. Gao, N.D. Whyborn, P.A.J. de Korte and T.M. Klapwijk, *Novel Design for a 2.5 THz Quasi-Optical Hot-Electron Bolometer Mixer*, Proc. of the ESA Workshop on Millimetre Wave Techn. and Appl., Espoo, Finland, June 21-23, pp. 504-509 (1998).

Curriculum Vitæ

Walter Frank Maria Ganzevles
Assen, 21 januari 1974.

Sept. '86 - juni '92: Gymnasium,
Menso Alting College, Hoogeveen.

Sept. '92 - juni '97: Technische Natuurkunde,
Rijks*Universiteit* Groningen.
Afstudeeronderzoek

'Determining the electron-hole scattering rate between 2D electron-hole gases'

in de groep *Fysica van Dunne Lagen*
o.l.v. prof. dr ir T.M. Klapwijk

Aug. '97 - dec. '01: Promotieonderzoek Technische Natuurkunde
Technische Universiteit Delft.
Proefschrift

'A Quasi-Optical THz Mixer Based on a Nb Diffusion-Cooled Hot Electron Bolometer'

in de groep *Nanofysica*
Promotor: prof. dr ir T.M. Klapwijk
Toegevoegd promotor: dr J.R. Gao

Nov. '01 – heden: Als process development engineer
werkzaam bij ThreeFive Photonics bv, Houten.

Dankwoord

Daar is het dan: het proefschrift. Feitelijk meer een product van velen dan van de promovendus alleen, vooral in dit geval omdat ik in vier laboratoria heb gewerkt. Begonnen natuurlijk bij professor Klapwijk in Groningen. Van harte, Teun, dank ik je voor de vrijheid die je je promovendi gunt en het niet aflatende vertrouwen in een goede afloop, ook als de zaken technologisch niet altijd even eenvoudig lijken. Bart – nu professor – van Wees dank ik voor de geboden gastvrijheid nadat de detector-groep naar Delft verhuisd was. In Groningen liggen ook mijn eerste schreden in de halfgeleidertechnologie: optische litho, sputteren, opdampen, bonden, 'even tussendoor koud': alles werd éven makkelijk geregeld! De hoogfrequentmetingen zijn gedaan in het lab van SRON, waar Paul Wesselius altijd wel een meetopstelling en een litertje ℓHe over had, hoe druk het ook was. Later werd dat zelfs een heuse werkplek! De technologen van DIMES hebben geholpen bij vele uurtjes e-beamschrijven, optische litho, opdampen, sputteren en etsen en onwillige lift-offs. Naarmate er meer process-werk in Delft werd verzet werden ook de faciliteiten in de Nanofysica-groep meer benut, vooral het bonden en cryogeen meten.

Vele, vele technici, office managers en anderen zijn bij dit alles van onschatbare waarde geweest, of het nu ging om een eenmalig SEM-fotootje, formuliertje in vijf-voud of het zetten van tientallen bonddraadjes: ieders bijdrage is van groot belang geweest.

Een speciale band is er natuurlijk tussen de AiO's onderling. Alberto, Jan-Peter, Pieter, Robert, Alex, Frank, Danny, Jochem, Friso, Diederik, Ruth, Andrey en Brian: ik zal de vele stoere verhalen en de vage meet– en process-acties niet gauw vergeten. Ik hoop dat de stappen–in–Groningen–avondjes, het bewijs van een bijzondere, hechte groep, nog tot in lengte van jaren zullen voortduren!

Hoewel met een veel kortere overlap wil ik hier ook de studenten noemen met wie ik nauw heb samengewerkt: Ruben en Maarten als afstudeerders,

Thea en Sander als interne stage-studenten. Dank voor jullie inzet!

Rode draad in dit alles is natuurlijk Gao. Altijd bereid tot een praatje (wat zeg ik? Die telefoon heeft niet dan roodgloeiend gestaan! ;-)), bemoedigend woord of een hoopvolle blik over de schouder bij de eerste metingen aan wéér een nieuwe batch samples. Ook voor theoretische discussies, de praktische beslommeringen rond ESA-contracten of de details van dat ene paper van –tig jaar terug kun je bij hem terecht. Nu ja, we zaten dan ook in hetzelfde keuken-schuitje. Gao, mijn dank is groot!

Hoewel uit bovenstaande het tegendeel zou kunnen blijken, ik heb de afgelopen vier jaar niet alleen maar in laboratoria rondgehangen. Mijn vrienden dank ik voor 't luisteren naar al die technologie– en *nerd*-verhalen, vele avondjes de stad in, spelletjes doen en bootje varen.

Ja, en dan het varen! Dick, Martijn, Marijke, Paul en Charlotte: dank voor onnoemelijk veel *trim!* pret, de wildste broaches, *VLAAG!!* — **TRIMMEN xxx!** —, borrels, *BIG WAVEs*, *dúmpen nu*, BHs (?!) en andere zaken.

Mijn ouders zijn er altijd als ik ze nodig heb. Ik ben jullie zeer erkentelijk voor alle steun en wijze woorden (ja, toch meestal wel!) al die tijd.

Dan nog, natuurlijk, is zij er, die bovenstaande allemáál heeft meegemaakt: Anniek. Heel veel dank voor het feit dat je er altijd voor me bent, naar me wilt luisteren en altijd wel een opbeurend woord weet te vinden!

Stellingen bij het proefschrift

A Quasi-Optical THz Mixer Based on a Nb Diffusion-Cooled Hot-Electron Bolometer

Walter Ganzevles

TR 3866-s'

1. Omdat de performance van diffusie-gekoelde hot-electron bolometer mixers sterk afhankelijk is van de precieze geometrie van de nanobrug en de koelflappen is dit type mixer minder geschikt voor gebruik als heterodyne ontvanger dan de fonon-gekoelde variant. *(dit proefschrift, hoofdstukken 8 en 9)*

2. Omdat het verwijderen van natuurlijk Nb_xO_y in een Ar-plasma zoals toegepast in dit werk een niet voldoende transparant interface oplevert verdient het voor een goede performance van diffusie-gekoelde hot-electron bolometer mixers aanbeveling een in situ geproduceerd Nb/Au interface te gebruiken. *(dit proefschrift, hoofdstuk 5)*

3. De directe respons van hot-electron bolometer mixers die hetzij via een co-planaire golfgeleider, hetzij via een microstrip transmissielijn gekoppeld zijn aan een twin-slot antenne kan in het frequentiegebied van 0.3-3 THz voldoende accuraat worden beschreven met een model dat de impedantie van de afzonderlijke elementen koppelt. *(dit proefschrift, hoofdstukken 6 en 7)*

4. Wattenstaafjes zijn een algemeen geaccepteerde vorm van schuurpapier in de nano-wetenschap van supergeleider-isolator-supergeleider-juncties.

5. Een kleine, terzake uitgeruste cleanroom-faciliteit is van grotere waarde voor een vakgroep dan een volledig uitgeruste multi-user cleanroom.

6. Voor eenieder in een nieuwe omgeving is het beheersen van de taal van het grootste belang voor een goede integratie.

7. Artikel 4 van de *Racing Rules of Sailing* biedt wedstrijdcomités voldoende basis om wedstrijden niet af te hoeven gelasten vanwege heersende of te verwachten weersomstandigheden. *(Racing Rules of Sailing 2001-2004, ISAF)*

8. Het stellen van regels schept werkgelegenheid.

9. De grootte van de 'mobiel' lijkt omgekeerd evenredig met de dikte en onduidelijkheid van de handleiding en met het aantal functies per toets.

10. Indien in de opvoeding voldoende aandacht zou worden besteed aan het omgaan met risico's zou het niet nodig zijn de normale bedrijfstemperatuur van een kopje koffie te vermelden op de verpakking.

Propositions to the thesis

A Quasi-Optical THz Mixer Based on a Nb Diffusion-Cooled Hot-Electron Bolometer

Walter Ganzevles

1. Since the performance of diffusion-cooled hot-electron bolometer mixers is strongly dependent on the exact geometry of the nanobridge and the cooling pads, this type of mixer is less suitable for application in a heterodyne receiver. *(this thesis, chapters 8 and 9)*

2. Since the removal of Nb_xO_y in an Ar plasma as applied in this work does not yield a sufficiently transparant interface, it is advisable to use an *in situ* fabricated Nb/Au interface when fabricating Nb hot-electron bolometer mixers. *(this thesis, chapter 5)*

3. The direct response of hot-electron bolometer mixers that are coupled to a twin-slot antenna using either co-planar waveguides or microstrip transmission lines can be accurately described in the 0.3-3 THz region using a model that couples the impedances of the constituent circuit elements. *(this thesis, chapters 6 and 7)*

4. Cotton swabs are a commonly accepted form of sandpaper in the nano-science of superconductor-isolator-superconductor junction fabrication.

5. A small, suitably equipped cleanroom facility is of more value to a university group than a fully outfitted, multi-user cleanroom.

6. For anyone in a new environment, mastering the local language is of the utmost importance for good integration.

7. Article 4 of the *Racing Rules of Sailing* offers racing committees a solid basis to not have to cancel races because of existing or imminent weather conditions. *(Racing Rules of Sailing, 2001-2004, ISAF)*

8. Establishing rules creates jobs.

9. The size of the cell phone seems inversely proportional to the thickness and incomprehensiveness of its manual and the number of functions per key.

10. If, in the raising of children, enough attention were paid to dealing with risks, it would not be necessary to mention the temperature of a cup of coffee on its container.